Republic of Iraq
Ministry of Higher Education
And Scientific Research
University Of Misan
College of Science

SYNTHESIS, CHARACTERIZATION OF INJECTABLE COBALT, ZINC AND SILVER IONS DOPED DICALCIUM PHOSPHATE CEMENT FOR POTENTIAL ORTHOPEDIC APPLICATIONS

A Thesis Submitted to
the College of Science / University of Misan as Partial Fulfillment
of the Requirements for the Master Degree of Science in Chemistry

By

Marwa Mohammed Abdullah

B.Sc. Chemistry / Basrah University (2012)

Supervisor

***Asst. Prof. Dr.* Ali Taha Saleh**

2025

بِسْمِ اللهِ الرَّحْمنِ الرَّحِيم

«يَرْفَعُ اللهُ الَّذِينَ آمَنُوا مِنْكُمْ وَالَّذِينَ أُوتُوا الْعِلْمَ
دَرَجَّاتٍ وَاللهُ بِمْا تَعّلَمُونَ خَبِيرِ»

صَدَقَ اللهُ الَعَلِيُ الْعَظِيمِ

"سورة المجادلة . . . . الآية (١١) "

Supervisor Certification

This is certified that this thesis entitled (**Synthesis, Characterization of Injectable Cobalt, Zinc and Silver Ions Doped Dicalcium Phosphate Cement for Potential Orthopedic Applications**) was prepared under my supervision at the Department of Chemistry. College of Science. University of Misan. As partial requirement of the degree of Master in Chemistry.

Signature
Assit. Prof. Dr. Ali Taha Saleh
Department of Chemistry
College of Science
University of Misan
Date: / /2025

Recommendation of Head of Chemistry Department

In view of the available recommendations. I forward this for debate by the examining committee.

Signature
Dr. Mohammed Abdulraheem Saeed
Head of Chemistry Department
College of Science / University of Misan
Date: / /2025

Dedication

To my pillar, my support, and my guiding light in life, my dear father. To the one who has showered us with love throughout her life, the one who gave without limits, my dear mother. To those who share my blood and soul, thank you for every word of encouragement and every smile that eased the hardship of the journey, my brothers and sister. To the light of my path and the source of my strength, my dearest husband, Raad. You were not just a husband, but a loyal friend, a patient listener, and a constant motivator. To my little darlings, the joy of my soul and the light of my eyes, and to you who were the greatest motivation to complete this journey, my children, Hussein, Muhammad, and Jana. To the beacon of knowledge who lit my path, Assistant Professor Dr. Ali Taha Saleh. With great pride and honor, I dedicate this work to you, for it would not have seen the light of day without your unlimited support and meticulous supervision.

Researcher

Acknowledgments

Praise be to God, the praise of the grateful, and peace and blessings be upon the master of creation and the noblest of messengers, our Prophet Muhammad, the trustworthy Prophet, and upon his pure and righteous family.

O God, to You be the praise for what You have given, and to You be the thanks for what You have granted.

I am pleased to extend my deepest thanks and appreciation to my distinguished supervisor, Assistant Professor Dr. Ali Taha, whose sound guidance, vast experience, and limitless patience were instrumental in the completion of this thesis. His continuous support and meticulous guidance were the best help for me to overcome challenges and bring the research to this final form. I pray that God rewards him with the best for all the follow-up and wise guidance he has provided. You have all my respect and appreciation.

To all who supported or helped me with a word or deed, my dear friends and colleagues, especially Samah and Zahraa Sabah.

I also extend my thanks and appreciation to the College of Science and the Department of Chemistry for the support they provided and for making many supplies available and facilitating the scientific research process as required, in service of our dear country, Iraq.

Researcher

Contents

Chapter One Introduction

Contents

Chapter Two Methodologies

Contents

Chapter Three Results and Discussion

Chapter Four

Contents

Contents

List of Figures

List of Figures

List of Figures

List of Tables

List of Tables

List of Abbreviations

Abbreviations	Key
HA	Hydroxyapatite
TCP	Tricalcium Phosphate
CPC	Calcium Phosphate Cement
CDHA	Calcium-deficient
CS	Compression Strength
βTCP	β- Tricalcium Phosphate
SBF	Simulated body fluid
P.	Pseudomonas aeruginosa aeruginosa
E. coli	Escherichia coli
BG	Bioactive Glasses
BCP	Biphasic Calcium Phosphate
MW	Microwave
MCPM	Monocalcium phosphate monohydrate
MCPH	Monocalcium phosphate hydrate
MCPA	Monocalcium phosphate anhydrous
MCP	Monocalcium phosphate anhydrous
DCPD	Dicalcium phosphate dihydrate (Brushite)
DCPA	Dicalcium phosphate anhydrous (Monetite)
OCP	Octacalcium Phosphate
αTCP	α-Tricalcium Phosphate

List of Abbreviations

Abbreviations	Key
TTCP	Tetracalcium Phosphate
ACP	Amorphous calcium phosphate
FWHM	Full width at half maximum
DDW	Doubled distilled water
FTIR	Fourier Transform Infrared Spectroscopy
XRD	X-Ray diffraction
EDX	Energy-dispersive X-ray spectroscopy
FESEM	Field Emission Scanning Electron Microscope
TEM	Transmission electron microscopy
UV	Ultraviolet Light
ICP-MS	Inductively coupled plasma mass spectrometry
LB	Luria-Bertani
SD	Standard deviation

List of Symbols

Symbols	Key
e.g	For Example,
etc	Et Cetera
3D	Three-Dimensional
mol%	Percentage of Number of Moles
Ca/P	Calcium to Phosphate Ratio
wt%	Weight-Weight Percentage
ppm	Part Per million
µm	Micrometer
i.e.	In other words
Å	Angstrom
°C	Temperature
Nm	Nanometers
2θ	2 Theta
mM	Millimole
M	Molarity
min	Minutes
H	Hours
eV	Electron Volt
mg/L	Milligram Per Liter
Xc	Degree of Crystallinity
m2/g	Square Meter per Gram

Abstract

Calcium phosphate cements (CPC) are often favored over the other calcium phosphate-based biomaterials in orthopedic surgeries because of its potential to be resorbed under physiological situations. Rapid setting and usually have bad injectability because of the liquid–stable phase separation, brushite cements has restricted their clinical use. The putting reaction can affect the placing reaction and subsequently the placing time and the final residences of the cement. Cement injectability could be very essential for minimally invasive surgical approaches that require injection of the cement into bone defects, but, the important thing elements for the success of surgical interventions geared toward the implantation of prosthesis or osteoconductive substances is the prevention from postoperative bacterial infections. Incorporation of antimicrobial sellers which includes antibiotics or other antimicrobial retailers in dicalcium phosphate (DCP) cements can save you put up-surgical infections. In this have a look at an array of novel DCP cements were prepared through doping Co^{2+}, Zn^{2+} and Ag^{+} ions into hydroxyapatite (HA) followed by their reaction with monocalcium phosphate monohydrate (MCPM) in presence of trisodium citrate. The effect of ion doping on the placing time, injectability, compressive power, and antimicrobial interest of the (DCP) cements had been studied. X-ray diffraction (XRD), field emission scanning electron microscopy (FESEM) attached with strength dispersive X-ray evaluation (EDX), and Fourier Transform Infrared spectroscopy (FTIR) techniques were employed to assess the section composition, floor morphology and chemical compositions of doped-HA and DCP. Gillmore needle apparatus become used to decide initial and very last setting times of cements (ASTM C266-89). Instron series ix (ASTM-model 8.33) became used to determine compressive energy. The in vitro dissolution behavior of all cements became evaluated by way of immersing the samples in the simulated frame fluid (SBF) over 7 days at 37 °C. Co, Zn and Ag substitution in HA-based totally brushite cement expanded the compressive electricity. Launch profiles of antibiotics advise that the doped cements can also serve as controlled drug launch systems.

CHAPTER ONE

INTRODUCTION

1.1 Overview

Due to its excellent osteoconduction trends, high biocompatibility, and outstanding bioactivity, HA has found extensive utility in biomedical applications. Because of this, HA is becoming more and more popular in products like dental materials and orthopedic implants. In recent past, surgery was often used to treat diseased or damaged hard tissues, which involved removal of damaged tissue by surgeons to relieve suffering. However, now researchers have focused their attention towards the development of antibacterial biomaterials having structural and biological similarities along with the natural hard tissue.

1.2 Human Bone

Nonstoichiometric calcium phosphates (CaP) together with trace amounts of other ions make up the unique composition of bone. Bone is a somewhat ordered polymer/ceramic nanocomposite that provides shape to the frame's skeleton [1]. It serves as a great reservoir for various minerals including calcium and phosphate in addition to its structural support of the body [2]. Bone is a dynamic material with the unusual capacity to self-organize or regenerate to a positive volume till the end. There are two kinds of bones: one is the cortical bone, also known as the compact bone, and the other is the trabecular bone, also known as the cancellous or spongy bone. These types are divided into groups according to their unit microstructure and porosity [3]. Long bones often include cortical bone in their shafts. With five to ten percent porosity, it's a very thick form. It is seen at the end of joints as the outer shell around the cancellous bone [4]. Based on their microstructure, certain types of cortical bones may be distinguished from one another. Compared to trabecular bone, cancellous bone is more porous, ranging from 50% to 90%. It may be found within vertebrae, at the end of long bones, and on flat bones [5].

1.3 Main inorganic components of bones.

The biomaterials contain several main inorganic compounds Table 1

Table 1: Important of calcium phosphate compounds with Ca/P ratio

Compound	**Formula**	**Ellipsis**	**Ca/P**
Hydroxyapatite	$Ca_{10}(PO_4)_6\,(OH)_2$	HA	1.67
α-Tricalcium phosphate	$\alpha\text{-}Ca_3(PO_4)_2$	α-TCP	1.50
β-Tricalcium phosphate	$\beta\text{-}Ca_3(PO_4)_2$	β-TCP	1.50
Dicalcium phosphate anhydrous	$CaHPO_4$	DCPA	1.00
Monocalcium phosphate monohydrate	$Ca\,(H_2PO_4)_2{\cdot}H_2O$	MCPM	0.50
Octa calcium phosphate	$Ca_8H_2(PO_4)_6.5H_2O$	OCP	1.33
Dicalcium phosphate Di hydrous, brushite	$CaHPO_4.2H_2O$	DCPD	1.00
Tetra calcium phosphate	$CaO.\ Ca\,(PO_4)_2$	TTPC	2.0

1.4 Biomaterials

Due to the growing ageing population and the treatment of illnesses, biomaterials have been gaining importance. Research on the creation of novel materials or the configuration and shaping of biomaterials has been heavily focused on home décor [13]. As implants, napkins, and member engross and distribution structures, the user is usually favored [6]. One effective method of extending life expectancy is by biological restoration, repair, or updating of the damaged tissue through integration with the intricate structure [14]. Depending on their biocompatibility and other characteristics, biomaterials may be used in a variety of packages due to their diverse mechanistic, physiological, alchemical, and constitutional homes. One class of materials found in biomedical devices are ceramics [15]. Because ceramics may mimic a diffusion process with high compressive strength, they are often employed as implant materials because they are physiologically hospitable and changeable [16]. The increasing similarity between the chemical composition of calcium phosphate and some ceramics [17]. These materials exhibit exceptional bioactivity, high levels of biocompatibility, and amazing [18]. Even yet, treating bone disorders resulting from long-term illness or trauma remains a challenge for medical professionals. In addition to the necessary duration, the treatment of skeletal illnesses often necessitates the use of synthetic biological materials [19]. due to the limited supply of (tissues or cells) taken from the same person. The use of artificial biomaterials, tissue grafts, organ transplants from donors of a different species than the recipient, and bone sections from certain types of brutes are crucial because to the risk of viable contamination from the use of allograpght [18, 20]. The benefit of using xenogenous bone is that it closely resembles the form and structure of the human skeleton. Bones from cattle, sheep, pigs, or fish are used to create xenografts, which contain a large number of valuable ions that can easily be obtained in bulk deliveries and need inexpensive transference [21]. Xenogenous materials may withstand a removal process that involves heating them to higher temperatures.

1.5 Calcium Phosphates

Like metals determined at loftiness, calcium phosphates are crystal ceramics with an alchemical texture and structure. One often used model of calcium phosphate is HA, which is based on the chemical formulation and has a structure similar to the main metals found in bone, apatite [22].

Because of its real biocompatibility, bioactivity, high osteoconductive and/or osteoinductive ability, nontoxicity, and residences, HA is suited for employment as a loftiness filler and as a covering on prostheses [23]. It seems that floor price scaffolding is connected to the promotion of osteogenesis and osteointegration that calcium phosphate scaffolds are said to foster [24]. Nevertheless, the resorption price of this ceramic is modest. Consequently, other calcium phosphates were developed, including β-tricalcium phosphate, which has a quick resorption rate.

1.6 Hydroxyapatite (HA)

HA molecular structure: $Ca_{10}(PO_4)_6(OH)_2$. Those bioceramics may be intentionally synthesized using special techniques, such as precipitation, hydrothermal, multiple emulsion, biomimetic deposition, and electrodeposition techniques [25]. They crystallize into the hexagonal device (figure 1.1) [27]. Moreover, appropriately produced using the sol gel method, which combines certain precursors of phosphorus and calcium to produce an excessively pure HA at the molecular level [26, 27]. Given the possibility for synthetic manufacture to be improved, HA may also be removed from the skeleton template, wherever it is naturally established in large quantities. Undoubtedly, the mineral additives that make approximately 70–80% of the noncellular skeletal template provide a tremendous amount of mechanical electricity [28]. A Ca/P ratio of less than 1.67 is opposed by normal HA, and its uneven nanostructured crystal contains carbonate companies and strains of several ions, such as $HPO^{2-}{}_4$, Na^+, $Mg^{2+,}$ Sr^{2+}, k^+, Cl^-, and F^-, inside of it [29]. Ionic substitutions can be added about by either changing the Ca^{2+}, $Po_4{}^{3-}$ or OH^- ions. Numerous ionic substitutions in HA ($Ca_{10}(PO_4)_6(OH)_2$) crystal structure have already been achieved to adjust its houses. Ca^{2+} ion can be replaced by monovalent cations (Na^+ [29] K^+ and Ag^+ [50], divalent cations (Sr^{2+} [30] Zn^{2+} [31] Cu^{2+} [32] and Mg^{2+} [33]), trivalent cations (Cr^{3+} [34], Fe^{3+} [35] and Al^{3+} [36] or tetravalent cations (Ti^{4+} [37] have been used to replace the Ca^{2+} ions. Those substituted ions have reported effect upon the crystallite size, diploma of crystallinity, lattice parameters morphology, solubility and bioactivity of HA. The $PO_4{}^{3-}$ group can be replaced by $CO_3{}^{2-}$ or $SiO_4{}^{4-}$, this type of substitution is termed as B type substitution. While OH can be replaced by either $CO_3{}^{2-}$ or F^- ions, this type of substitution is referred to as A type substitution.

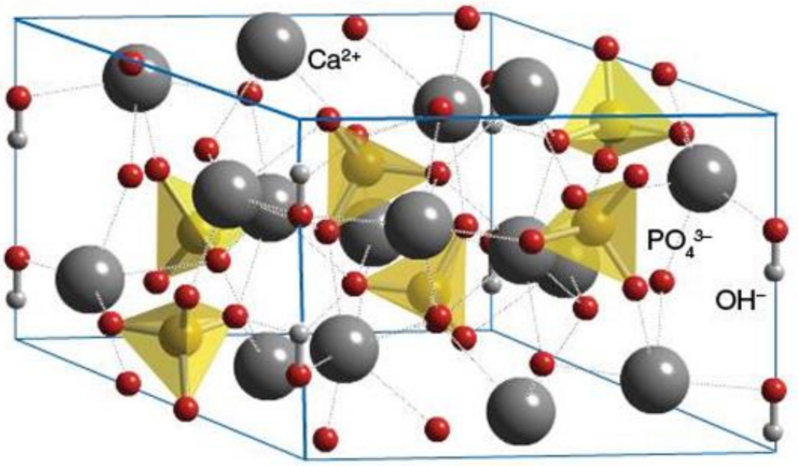

Figure 1.1: Crystal structure of hydroxyapatite

1.7 Compounds related to Hydroxyapatite

Compounded mostly of calcium phosphate (CP), these compounds have a Ca/P molar proportion within the zero range 5–2 [32] and are the most sought-after biomaterials for the reconstruction of many skeletal issues, especially in the fields of orthopedics, shock surgery, and dentistry [33, 34]. Table 1 provides a brief summary of important CP-based all-ceramic materials along with their formulae and packaging. Owing to their exceptional biocompatibility [35, 36], osteoconductivity [37], and osteointegration [38], compounds principally derived from CP have been the subject of much investigation over the last fifty years. Biomaterials that are largely CP-established are appropriately used to replace and strengthen the strong tissues of the epidermis frame that are damaged or deteriorating.

The term "apatite" is often used to describe CPs' magnificent reign trendy technique, in which A and B are regarded as calcium in many distinct residences that are special to phosphate institutions, and X denotes the subsistence of OH- organisation within form [38]. HA is an important CP-primarily initiated chemical that resembles a metal element found in enamel and herbs [41]. HA with bioactivity [39] and a Ca/P ratio of [40]. It has been used for more than 50 years as a dental grow and as a bone exchange fabric [41]. Because of its osteoconductive immovables, HA can promote rapid bone renewal and instant bonding with regenerated bone without the need for moderate conjunctive tissues. Its artificial form is primarily used to remodel strict environments, such as strict textile reconstruction [42]. due to HA growing importance as a biomaterial, attempts are constantly made to make HA's organic homes more beautiful. Although HA crystals are used extensively in the field of orthopedics, their high rate of deterioration in the physiological environment restricts their use in clinical settings. [43] Research has shown that adding biocompatible ions to HA ion-pleasant crystal structure may modify the degradation average of the compound [44].

In its crystalline state, hydroxyapatite exhibits remarkable thermodynamic properties [45]. Without resulting in any localized or systemic toxicity, infection, or foreign frame response, HA may mix with bone [46]. These factors have led to the widespread use of HA in biomedical packaging, particularly in odontology and orthopedics, as well as the covering material for metallic implants [20, 47]. Consequently, a great deal of research has been done on methods for creating HA that may be modified. Conventional chemical methods lack the necessary HA assembly signal of beneficial components such as silicon, barium, sodium, zinc, and fluorine ions, among others; the presence of those ions directly affects a number of biological processes connected to bone metabolism. The assembly description and use of ion-substituted HA were accurately depicted in recently published research publications [48]. Ions have the ability to interchange all of the OH- or PO43- ions, which is often referred to as A-type or B-kind substitution, or they may replace the Ca ions within the crystalline structure. Less costly natural organic reservoirs, including as fish and mammal bones [49], corals, eggshells, seashells, and flora, have made it possible to create ready-made ion-doped HA in an appealing and effective way [50].

1.8 Bioceramic material

Ceramics have been widely used within the area of biomedical engineering and in the medical packages for decades. An example of herbal ceramics is biological apatite whilst hydroxyapatite ($Ca_{10}(PO_4)_6(OH)_2$) and β-tricalcium phosphate (β-TCP, $Ca_3(PO_4)_2$) are the most commonly used synthetic ceramics [51, 58],[59]. HA and βTCP are the most appealing material due to its notable bioactivity, biocompatibility, osteoconductivity and chemical composition similarity within the bones and teeth [60]. It could effortlessly be implanted in the frame and show less toxic behavior in evaluation to metals or polymeric fabric. This fabric is likewise essential as it has potential to give balance to bones and show quicker bone formation and bonding.

Bioceramics are generally difficult and brittle, which make their use tough for load-bearing programs but additionally they have excessive compressive strength due to the excessive compression and put on resistance. Ceramics are traditionally used in dental restorations and orthopedic surgeries (e.g. As a part of artificial joints) [52]. Ceramics in powder form are also used with polymers to fill the bone cavities as bone cements in dental and orthopedic packages [53].

1.9 Synthesis of Hydroxyapatite

New economical and versatile methods for HA are of great interest due to the importance of these materials in the field of biomedical sciences. Different protocols are generally used for HA, β-TCP and their ion substituted analogues to prepare materials with closer similarities to the living hard tissues such as bone and teeth. Solid state routes are quite established and have been in use for last many years but due to some technical constraints, price and due to lack of appropriate equipment make this route unpopular and is often regarded as a poor choice to prepare HA. Products of co-precipitation method are usually amorphous in nature and require long heat treatments at very high temperatures to attain good degree of crystallinity, which simultaneously results in the reduction of surface area of the products. Sol-gel method has been used for the preparation of CaP based materials, however simultaneous hydrolysis, condensation, aggregation and post reaction high temperature calcination make this method less attractive. In recent years the use of hydrothermal method to prepare nanomaterial has increased tremendously but the low reaction kinetics and difficulties in conducting large scale synthesis make this method less popular with the researchers. Microwave assisted synthetic methods are fast gaining popularity as microwave heating provides rapid volumetric heating resulting in the formation of crystalline products.

1.10 future perspectives

The most recent data regarding the make use of hydroxyapatite as a clipper in fabric control pertains to investigations concerning its physical-chemical properties and organic reaction, which supports cellular proliferation in vitro, are accompanied by a reduced risk of transmitting pathogens and outstanding biocompatibility [64]. Consequently, hydroxyapatite for snapper is a potentially valuable byproduct of industrial application, textile manufacturing, and medical and dental products. Nonetheless, numerous obstacles and constraints must be surmounted in order to implement it. The evaluation of biocompatibility must be conducted through in vitro and in vivo investigations involving distinct species of fish; this is a viable approach to ascertain the fabric's ability and security. In addition, distinct documentation must be implemented and examined during the display of hydroxyapatite of Pisces. Recent studies have validated the feasibility of fabricating nano-sized hydroxyapatite pigeonhole imitators with larger dimensions. the substances added to bone tissue [65].

1.11 Thermal calcination method of HA

Recent research has focused on the utilization of hydroxyapatite in the texture facet of pouter, particularly in relation to its physical-chemical properties and natural reaction. These results support that [66], which promotes cellular proliferation in vitro while posing little risk of transport from contaminants and ensuring excellent biocompatibility [67]. Within the given framework, hydroxyapatite of gudgeon serves as a valuable resource at high altitudes, particularly for industrial applications and as a component of medical and dental products. Nevertheless, certain limitations must be surmounted. All biocompatibility assessments must be conducted using in vitro and in vivo studies, with the employment of particular fish species serving as an effective method to evaluate the fabric's safety and performance. Moreover, when exhibiting HA derived from fish, specific documentation must be synthetic and tested. Innovative research has demonstrated [68]. As a result, nano-HA fish-based fully biomaterials have the potential to provide HA, exhibiting enhanced bioactivity during degradation compared to irregular crystals due to their high floor-to-area ratio and specific chemical properties [69]. As a result, the potential purchase of nano-hydroxyapatite from Pisces may result in increased osteoblast adhesion and mobile proliferation [86]. The increased consumption of pouter in the industry has led to a significant increase in the disposal of fish waste in the form of scales and bones. The process of recovering fish scales and bones yields parent HA and recoups substantial residues generated during the fisheries industry [70]. Fish bone is an exceptionally abundant resource for the extraction of HA. The morphological dissection of the HA, which was obtained for the mammalian loftiness display, reveals that the detritus is predominantly asymmetrical in shape, with variations observed in the final complexion morphologies across different research performances. The shape version is therefore not considered to be affected by the approach or fountain. For instance, a model calcification of an identical supply of loftiness has the potential to generate various morphologies of HA, including rod-like, spherical, and needle-like [71]. In the same way that specific extraction techniques, such as alkaline hydrolysis, can produce HA in the form of rods, there may be no correlation between the morphology of HA and its supply or descent procedure [72]. The obtained HA dimensions exhibited no discernible correlation with the extraction method. Supplemental milling was employed to reduce the size of the HA particles to a nanometer scale, which is comparable in length to human HA [73]. Additional floor action and ultrafine systems that are increasing [74].

1.12 Opportunity preparation approach

Scholars have undertaken investigations into the production of calcium phosphates for standby purposes, employing techniques. Which includes alkaline hydrolysis, hydrothermal, and laser ablation. HA was utilized to collect an assemblage of blue shark (Prionace glauca) Pisces loftiness-based completely microscale detritus through the use of a laser ablation device formulated for compressed petrol plane without prior calcification [75]. The investigation validated the feasibility of extracting calcium phosphates through direct ablation without the need for calcination. The process of instruction was examined [76]. Fish bones underwent a preliminary calcination process at 950 °C to eliminate any potential organic contamination, followed by milling to obtain particles on the microscale. Hydroxyapatite microparticles were employed as precursor material in laser-induced fragmentation analyses. Particles of β-tricalcium phosphate and hydroxylapatite measuring 10 nm in diameter were received in nanometric form. Boutinguiza et al. [78] have employ CO_2 throb laser ablation in all other investigations to obtain calcium phosphate nanoparticles from swordfish bones that were previously calcined at 600 °C. approximately 25 nm in diameter at the median [79].

1.13 Dicalcium Phosphate (DCP) Cements

Monetite and Brushite Almost two decades have passed since the invention of dicalcium phosphate cements. Since then, considerable research has been conducted to enhance the properties of dicalcium phosphate cements for clinical applications and to meet the requirements. Dicalcium phosphate anhydrous (DCPA) and dicalcium phosphate dihydrate (DCPD) are the two classifications of DCP cements.

1.14 Brushite and Monetite Structure and Properties

DCP cements have demonstrated efficacy in animal models for bone regeneration at various surgical sites, including the condyle, distal femoral metaphysis, and epiphysis [80]. In 1989, brushite cement was discovered by Mirtchi and Lemaitre [81] through the combination of β-TCP, water, and MCPM. The resulting combination changed into a bendy adhesive that solidified through an exothermic response, producing a substance composed of dicalcium phosphate dihydrate, additionally known as "brushite" by mineral name. [82].

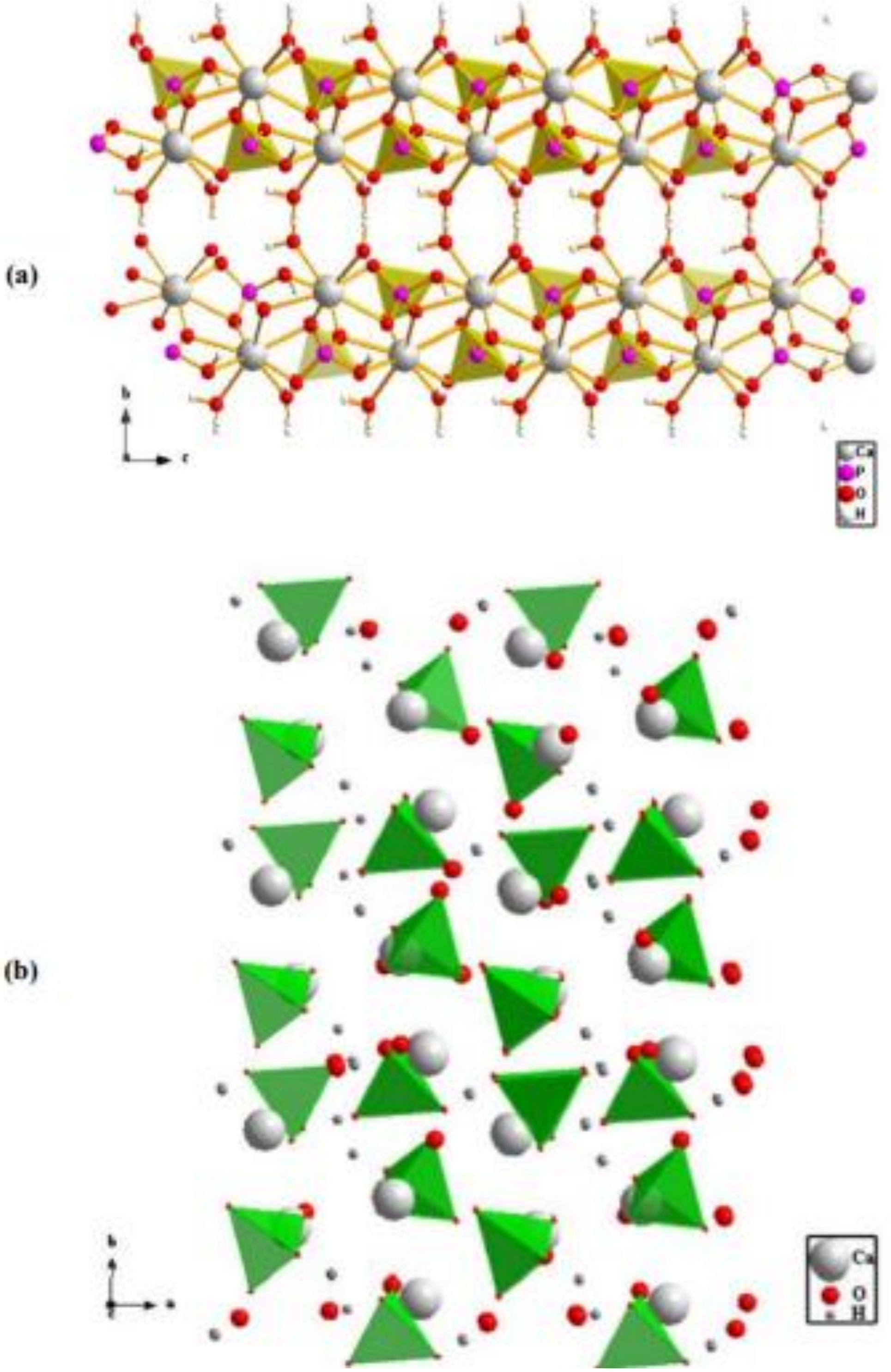

Figure 1.2 Projection view of (a) brushite and (b) monetite

Subsequent research has provided evidence that brushite cement is biocompatible and capable of undergoing reabsorption under physiological conditions. The principal components of dicalcium phosphate (DCP) cement are an acidic phosphate source, water, and an antacid calcium precursor. However, additional substances may be incorporated into the mixture to extend the setting time, improve mechanical properties, or facilitate bond treatment. Brushite (DCPD) bonds serve as precursors to monetite (DCPA), also known as anhydrous DCP. The exothermic precipitation of brushite is commonly facilitated by the setting of DCP bonds [83]. The crystal structure of brushite is monoclinic (space group Ia). As illustrated in Figure 1.2 (a), the unit cell of brushite contains four $CaHPO_4 \cdot 2H_2O$ motifs. The latter indicates that the crystals consist of brushite corrugated sheets with a CaHPO4 composition. These sheets are aligned parallel to one another, with a direction perpendicular to axis b. A double layer of water molecules connects the sheets [84]. In animal models, DCPs have been tested and found to be effective for bone regeneration at various surgical sites, including the condyle, epiphysis, and distal femoral metaphysis [85]. In 1989, Mirtchi and Lemaitre discovered brushite cements through the combination of water and a powdered compound consisting of β-tricalcium phosphate and an acidic calcium phosphate (monocalcium phosphate monohydrate). The resulting mixture was a flexible adhesive that eventually solidified in an exothermic reaction, forming a rigid substance composed of dicalcium phosphate dihydrate, also known as "brushite" by mineral name [86].

1.15 Ionic Substitutions of HA

Substitutions of ions cause changes in the lattice parameters, particle size, morphology, solubility, crystallinity, thermal stability and biological properties of

HA. The characteristics of the substituted apatite are dependent on the ion incorporated, the amount of doping and the site of substitution. The ions can substitute calcium, phosphate or the hydroxyl group. These substitutions can happen independently, just one ion or simultaneously more than one ion.

Cationic Substitutions

It is assumed that cations such as Mg^{2+}, Er^{3+}, Ba^{2+} and Ni^{2+} . Asubstitute into the lattice at one of two distinct sites, either at Ca(1) or Ca(2). Previous research has suggested that the ions with ionic radii smaller than the ionic radii of Ca^{2+} ion occupy Ca (I), while the ions with ionic radii larger than the ionic radii of Ca^{2+} ion occupy Ca (II) site.

i. Barium doped HA

Barium ions (Ba^{2+}) are present as trace ion in sedimentary rock, food, drinking water, human enamel (125 ppm) and in dentin (129 ppm). Barium compounds such as barium apatite have good mechanical properties and is used as a filling material for root canal [87] barium doped europium oxide silicates ($Ba_4Eu_6(SiO_4)_6O$) is known for its exceptional biocompability with tendency to enhance cell proliferation of osteoblast cells. Barium titanate ($BaTiO_3$), another barium based biocompatible material is often mixed with HA and is used as a bone substitute material to promote *in vivo* bone growth to enhance bone formation around implants [88] and for osteogenesis. Furthermore, barium sulphate ($BaSO_4$), has many biomedical applications due to its wound healing properties. It is also used as a contrasting agent and as an implant template during placement of dental implants [89].

Several studies have reported synthesis of barium apatite ($Ba_{10}(PO_4)_2(OH)_2$) prepared by solid state reaction and precipitation method, barium fluoro apatite ($Ba_{10}(PO_4)_6F_2$) obtained through solid state reaction barium chloro apatite doped with Eu^{+2} ($2Ba_{5-x}Eu_x(PO_4)_3Cl$) synthesized by solid state reaction [90] barium–strontium hydroxyapatites ($Ba_{10-x}Sr_x(PO_4)_2(OH)_2$) prepared by wet method and carbonated barium hydroxyapatites (($Ba_{10}(PO_4)_6(OH)_{2-2x}(CO_3)_x$) prepared by wet method Previous studies have shown that the partial incorporation of Ba^{2+} ions (0.7 mole) increased the lattice parameters along the *a* and *c* axis and formed rod-shaped agglomerates [91,92]. The above-mentioned studies have only focused on the synthesis and structural characterization of the materials.

ii. Nickel doped HA

In general bone defects due to osteomyelitis and periapical lesions become more complicated and their heeling is difficult. Moreover, removal of pathogens biome is tricky with systemic antibiotics; therefore, in these circumstances biomaterials containing antimicrobial activity can be a promising bone healing method [93,94]. Trace amount of Ni^{2+} ions are beneficial to run various biochemical processes of the body but its addition beyond certain limit [2-18(ug/g)] may be toxic for the body. Antibacterial activity of nickel (Ni^{2+}) ion is well documented therefore doping of Ni^{2+} ions in HA would part important antibacterial properties to combat post-operative bacterial infections. Several studies have indicated that the activity of Ni^{2+} ions containing urease enzymes in microorganisms of the gastrointestinal tract could be stimulated by Ni^{2+} ions supplements. Studies on rats, chicks, pigs, goats and sheep have confirmed that Ni^{2+} ions are essential for growth. In animals or humans, it acts as a structural issue in unique metalloenzymes (e.g. Urease, hydrogenase), or as a cofactor facilitating the intestinal absorption of the ferric ions, it is also required for the synthesis of an endogenous, bacterial (*Methanobacterium thermoautotrophicum*) pigment (F430)[95]. Previous studies have shown that Ni^{2+} ions doping in HA structure leads to reduction in the degree of crystallinity and crystallite size as well as a small decrease in lattice parameters along the *a* and *c* axis. Maximum possible amount of Ni^{2+} ions substitution for Ca^{2+} in the HA structure is about 3 wt% [96].

iii. Magnesium doped HA

Magnesium ions ($Mg^{2+)}$ are the fourth maximum considerable cation gift in the human and are required through extra than a hundred enzymes for his or her catalytic hobby [97]. It is directly related with the mineralization of calcified tissues and in stimulating osteoblast proliferation hundred and Mg^{2+} doped apatite is extra effective and might substantially accelerate osteoblast adhesion to the apatite and promote bone formation. Mg^{2+} deficiency may also affect skeletal metabolism, cessation of bone growth, osteoblastic and osteoclastic activities and bone fragility. Owing to this prime importance of Mg^{2+} various studies have reported doping of Mg^{2+} in HA through solid state[98].

Mg^{2+} incorporation in HA generally decreases the degree of crystallinity, particle size and reduces the lattice parameters along with *a* and *c* axis of HA. Furthermore, complete replacement of Ca^{2+} ion by Mg^{2+} in HA lattice ($Mg_{10}(PO_4)_6(OH)_2$) has toxic effect on bone cells and prevents the formation of an extracellular matrix [99].

iv. Silver doped HA

There is a myriad of studies that have identified Ag^+ ion as an eminent anti-bacterial agent against negative gram- and positive gram+ bacteria, viruses as well as fungi. Ag^+ ions are also capable of restricting the growth of numerous organisms. As a result, the different forms of Ag^+ ions are used to slow down the growth of bacteria and microorganisms [100]. HA that is enhanced with Ag^+ is widely used in orthopedic and dental surgery.

A well crystalline Ag-substituted apatite material shows good anti-bacterial activity against S. aureus and *E.* coli bacteria. Furthermore, anti-bacterial activity of Ag^+ containing HA and related materials is concerned with the rate of release of Ag^+ ions from the apatite. Greater is the rate of release of Ag^+ ions greater will be its anti-bacterial activity [101].

v. Copper doped HA

Since Copper ions (Cu^{2+}) are involved in an innumerable of metabolic processes, they are regarded as essential micronutrients almost in all living organisms. Copper's antibacterial properties have been well known for a long period of time. There are some Egyptian texts that were written approximately 2600–2200 BC which showed that copper was used to sterilize chest wounds as well as drinking water [83]. Studies have established that when HA is enhanced with Cu^{2+} ion, it becomes efficient in the inhibition of *E. coli* and *S. aureus* bacteria.

vi. Cobalt doped HA

Cobalt ions (Co^{2+}) ions can also play an important role in enabling the human body to function properly. Co^{2+} is also found in vitamin B12, which is responsible for functions such as, regulation of the generation of red blood cells, synthesis of DNA in cells, development of the myelin sheath, and protection of nerve and neurotransmitter cells [93]. There are some studies that have delved into the use of Co^{2+} as an antibacterial and antiviral agent in a variety of organic complexes The hydrothermal method was developed by Ignjatovi´c *et al.* to enable the development of HA enhanced with 5–15 wt% Co^{2+} ions but no antibacterial activity was undertaken. Using the wet method, developed a nanocrystalline HA enhanced with 0.46 wt% and 3.79 wt% Co^{2+} ions with good antibacterial activity against *Shigella flexneri, Micrococcus luteus, S. aureus,* and *P. aeruginosa* bacteria [101].

1.16 Setting Time of bone cement

The setting time is a critical factor in meeting clinical requirements; prolonged setting times can lead to clinical complications because cement is unable to retain its shape and withstand stresses during this period. [106]. Following the combination of solid and liquid phases during the formation of bone cement, a setting reaction occurs, resulting in the formation of cement. The putting reaction of brushite cement consists of the following: (i) dissolution of cement particle components in a solvent; (ii) formation of a supersaturated gel; (iii) nucleation in the gel; and (iv) formation of interlocked crystals that compose the solid. The setting reaction of the β-TCP/MCPM bonds initiates with the dissolution of MCPM, which rapidly results in a decrease in pH to 2.5 [89,110]. An overabundance of MCPM results in the cement maintaining a low pH even after the curing reaction has concluded. In contrast, when the quantity of β-TCP is substantial, the bond's pH equals 5 [106]. Vicat needles or Gilmore needles are utilized to verify that the cement has completely hardened [5,104]. A macroscopically solid cement is typically characterized by the absence of discernible penetration of the needle into the cement surface. The international standard (ASTM C266-89) specifies that the ultimate setting of the β-TCP/MCPM cement framework occurs shortly after blending [103]. For particular applications, the optimal value of the setting time is contingent on the surgical procedures involved. Surgeons recommend an initial setting time of 3 to 8 minutes, with approximately 8 minutes designated for orthopedic procedures and 3 minutes for dental procedures [104]. For both applications, an ultimate setting time of less than 15 minutes is preferable.

1.17 Injectability

Vessel injectability the injectability of the cement is critical for minimally invasive surgery concerning the injection of the cement right into a bone defect [105]. The cement's injectability is constrained as a result of the solid segment and liquid segment being separated via filter compression [18]. The limited injectability of various brushite formulations can be attributed to a phase separation issue. The mechanisms of phase separation that are observed during the excursion of cement paste. To address these challenges, one may consider increasing the extrusion speed and make use of a shortened canula syringe, both of which have been observed to enhance injectability [106]. Additionally, the injectability of cement can be enhanced through the following methods: increasing the viscosity of the mixing liquid, decreasing the PLR, conducting extensive processing of the cement powder, make use of modified cement reagents to decrease the particle–particle interface, and adding carboxylic acids as additives [107,108]. Doping β-

TCP with Mg, Sr, and Si ions has been observed to enhance the injectability of DCP cement [11, 13, 14, 18]. This effect of increased injectability cannot be generalized, as doping -TCP with Sr ions has also been reported to decrease the injectability of the cement [77]. Additional significant characteristics of DCP cement may be subject to alteration as a result of efforts to improve injectability. Likewise, a reduction in PLR results in compromised mechanical characteristics of the cement [105]. Due to the paste-like consistency that results from combining polymeric materials such as chitosan, alginate, and gelatine into CPCs, their handling properties can also be enhanced [107].

1.18 Mechanical Properties

The only criterion frequently used to evaluate the mechanical performance of CPCs is their compressive strength [3]. This criterion is frequently employed to estimate the mechanical performance of CPCs. In general, the compressive strength of apatitic CPCs is higher than that of brushite CPCs [3]. Cements and bioceramics designed for bone regeneration need to own the equal mechanical houses as bone. Pure brushite cement, however, as Lemaitre and Mirtchi have prepared it, possesses weak mechanical properties. A variety of approaches (including the incorporation of polymers and ions such as Mg^{2+}, Sr^{2+}, Zn^{2+}, among others) have been explored in order to tackle this issue [106,107]. Prior to testing, brushite cements are commonly allowed to harden for a minimum of 24 hours so that their mechanical properties can be evaluated (ISO 5833, 2002) [3,51]. Samples of CPC may be maintained under physiological conditions (37 °C and 100% humidity) or dry conditions (room temperature and humidity) throughout the setting time [83]. Clinically pertinent data is collected during the storage of CPC specimens under physiological conditions. As a means of determining whether a cement is suitable for biomedical applications, its compressive and tensile strengths are typically evaluated [5]. In contrast, the porosity of brushite cements is correlated with their compressive strength [66,108]. Reducing the porosity of the cement results in enhanced mechanical performance. By compacting the CPC during the setting reaction, its porosity is decreased, which increases the bone cement's compressive strength [45]. By optimizing the setting response conditions, Cement structures that consume water at some point of setting, along with brushite, could theoretically produce ceramics with nearly zero porosity. This was achieved through the augmentation of PLR proportion and the incorporation of setting retardants, which impede the ascent of crystals [108]. To improve the mechanical homes of DCP, sulphates, pyrophosphates, carboxylic acids, and metallic ions (Mg, Sr, Zr, and Si) may be utilized [109,110]. The introduction of free ions into a cement system typically has an effect on the setting time of the cement, but does not typically improve its mechanical properties. The introduction of metallic ions in the form of chloride compounds (e.g., SrCl2) into cement during the setting reaction does not yield favorable results in terms of influencing the mechanical properties of the cement [111]. Presumably, this occurs due to the formation of a soluble chloride sodium within the cement, which compromises its structural integrity. On the contrary, the introduction of ions as an alternative to phosphate or calcium enables the formation of phases that are less soluble, thereby contributing to the improvement of the cement's mechanical properties. For instance, the addition of Sr ions to cements can result in a 20% increase in the compressive strength of CPC based on β-TCP [11,112]. The compressive strength of pure brushite cements can be increased by as much as 40 MPa with the inclusion of magnesium. [113].

1.19 Antibiotics

Significant attention has been devoted to antibiotics due to their wide-ranging applications, including prophylactic measures to prevent surgical-associated infections and preferred treatments for bone infections [104]. In reality, a single determinant for the success of surgical procedures involving the insertion of an osteoconductive material or prosthesis is the prohibition of bacterial infections [105]. Developed complications may arise as a result of wound infection, postoperative infections following vertebral column surgical procedure, combined prosthesis insertion, or fracture restoration [106]. Due to this, prophylactic antibiotics are frequently administered orally or intravenously. Conversely, the moderate susceptibility of the site of infection to antibiotics administered systemically extends the treatment duration of bone infections by an average of one year [107].

In order to mitigate the occurrence of plant-associated infections, a multitude of external biomaterial interventions have been suggested. Previous research aimed to imbue biomaterials with antibacterial properties through roof functionalization techniques, such as coating cultivate surfaces with silver ions. [108].

1.20 Methods to synthesize CaP particles

Some of the commonly used methods for the preparation of CaP are electrochemical micro-emulsion hydrothermal sol-gel and microwave assisted have also been used for the production of metal nanoparticles. A brief detail of these methods is given below.

1.20.1 Co-Precipitation Method

This method involves the mixing of Ca^{2+} and PO_4^{3-} based precursors in a basic solution to prepare poorly crystalline HA or ion doped HA. In this method simultaneous nucleation, growth, coarsening and agglomeration of the precursors takes place in the solution to prepare the products. In this method nucleation of the reactants is the major step that occurs due to heavy precipitates followed by the growth of the crystals to furnish the agglomerated HA or ion doped HA[114].

This is one of the most traditional methods but slow mixing of the reactants and inhomogeneity of the reacting nuclei due to heterogeneous precipitation in turn may result in the formation of agglomerated products which make this method unpopular. Similarly, pH control is also an important step which requires strict monitoring to maintain at certain level to prepare stoichiometric HA. Products prepared via this method are usually amorphous in nature and require long heat treatments at very high temperatures to attain good degree of crystallinity, which not only makes this method time consuming but at the same time reduces the surface area of the products.

1.20.2 Sol-gel Method

Sol-gel is an established route for the synthesis of CaP particles but it suffers from drawbacks such as long reaction time and post reaction calcination, which results in the formation of hard agglomerated particles. Sol-gel synthesis also requires control of challenging factors like rate of hydrolysis, condensation, agglomeration of the particles and control over the size and morphology. The involvement of series of steps to furnish the final product makes this technique time consuming. The reaction begins with the preparation of 'sol' via solvated CaP species, which helps in synthesizing the gel. This gel is changed into the solid mass through long aging, drying and prolonged heating to prepare dense bulk ceramic materials[115].

Although sol-gel synthesis is a good method to synthesize different biomaterials but involvement of multi-steps makes this process time consuming and complex to prepare CaP particles. Similarly, instantaneous hydrolysis, condensation and aggregation steps make reproducibility and control over particle morphology very much complex. Moreover, the products are usually amorphous and demand long heating treatments to attain good degree of crystallinity.

1.20.3 Hydrothermal Method

Hydrothermal methods (batch and continuous) are used to synthesize CaP particles using aqueous or non-aqueous solvents at high temperature and pressure. Hydrothermal method is considered to be a better technique because of its simplicity. However, longer reaction times, use of high temperature and pressure involved in this reaction can be troublesome. To prepare crystalline products at large scale at high pressure can also be challenging. Slow kinetics and poor reaction rates also make this process time consuming. Similarly, continuous hydrothermal method is an expensive multichannel system that has its own demerits especially they are only workable at low concentrations

1.20.4 Microwave method

Microwave (Mw) technology has evolved as a fast synthetic technique to conduct our daily research activities. The classical discussion on microwave heating was first introduced by Gedy and Giguere/Majetich in 1986 to carry out organic chemical reactions and opened unending discussion on the demanding explorations of the Mw heating and its effects on the chemical reactions. Mw method has emerged as a promising source of heating and has received a considerable importance in various fields such as biomedical, polymer synthesis, materials science and in medicinal chemistry. In the beginning, experiments were performed in Teflon or glass vessels in domestic ovens without any control on temperature or pressure. However, now this problem has been solved due to the availability of pressure and temperature-controlled utensils and also due to the availability of good quality microwaves in the market.

In general, microwave electromagnetic radiations lie between infrared and radio waves, they have wavelengths between .01 and 1 meter and correspond to frequency range between 0.3 to 30 GHz. Major part of this wavelength is used in point-to-point communications. Furthermore, they have a lot of applications in the biomedical, industrial and scientific research fields. In order to evade any interference among domestic and industrial microwave reactors, domestic microwave reactors are often operated at standard allocated frequency of 2.45 GHz (corresponding to a wavelength of 12.25 cm). This frequency range is preferred for laboratory reactions because it has right penetration depth for laboratory scale reactions.

Molecules that have a permanent dipole moment can rotate in a fast-changing electric field of Mw radiation. Additionally, in substances where free ions or ionic species are present, the energy may also be transferred by the ionic motion in an oscillating Mw field. As a result of both these mechanisms the substance is heated directly and almost evenly. Heating with microwaves is therefore, fundamentally different from conventional heating by conduction. The magnitude of this effect depends on dielectric properties of the substance being heated.

1.21 Problem Statements

The majority of traditional chemical processes utilize HA synthesis without introducing any trace amounts of beneficial elements, including Na^+, Zn^{2+}, Mg^{2+}, K^+, Si^+, Ba^{2+}, F^-, CO_3^{2-}, and others. The inclusion of these ions has a direct impact on a range of biochemical reactions associated with bone metabolism. Despite the existence of numerous synthesis methods, the production of HA with specific properties continues to be a formidable task due to the potential formation of hazardous intermediate products. As a result, research into additional HA synthesis parameters remains ongoing. It is possible to chemically synthesis HA or extract it from natural sources. The synthesis of these bioactive compounds can be achieved through various straight forward methods. DCPs are frequently favored in orthopedic procedures over alternative calcium phosphate-based biomaterials. Present approaches to the development of DCPD are centered on enhancing the cements' in-situ setting characteristics while maintaining satisfactory mechanical properties under physiological conditions.

Brushite and monetite cement's rapid setting time has restricted their clinical applications. In addition, injectability is typically subpar in DCP cements that do not contain any added substances due to the liquid–solid stage separation. The presence of particular ions within the cement has the potential to influence the placing reaction, which in turn can affect the setting time and ultimate properties of the cement. Without additives, DCP cements typically have weak injectability as a result of the separation of the liquid and solid phases. The setting time and final properties of cement can be influenced by the setting reaction, which can be affected by the presence of specific ions in the cement. In minimally invasive surgical procedures, cement injectability is critical, as it permits the cement to be injected into bone defects. However, when it comes to surgical interventions involving the implantation of prostheses or osteoconductive materials, preventing bacterial infections or postoperative infections after fracture repair are critical success factors. Such infections can lead to severe complications. The advantage of employing antimicrobial agents, such as antibiotics, is that they inhibit the growth of resistant microorganisms and are rapidly eliminated by body fluids; thus, they can prevent post-operative infections for an extended period of time. By utilizing biomaterials that encapsulate antimicrobial agents, which are gradually eliminated by bodily fluids, it is possible to avert post-surgical infections gradually.

1.22 Objectives of the Study

1. To design and explore novel calcium phosphate-based biomaterials through ionic substitution into their crystal structure: Mono-doped hydroxyapatite such as Co, Ag and Zn ions.
2. To evaluate the effect of ionic substitution up to the setting time, injectability and mechanical properties of dicalcium phosphate cements.
3. To study the effect of ionic substitution on the in-vitro resorption of the dicalcium phosphate cements in simulated body fluid (SBF).

4. To evaluate the mechanical properties, injectability, and setting time of dicalcium phosphate cements.
5. To determine whether dicalcium phosphate cements have the capacity to serve as drug carriers in applications requiring sustained drug release. and study the antibacterial properties of silver doped with dicalcium phosphate cement against *Escherichia coli* (*E. coli*).

1.23 Significance / Novelty of the study

This research endeavors to produce HA synthetically. The aim of this research was to determine the composition and properties of HA that were subjected to a high-temperature (1000°C) treatment. 1.67 was determined to be the Ca/P molar ratio, which corresponds to the stoichiometries of HA. As a biomaterial, these findings possess potential for use in biomedical applications. The materials in this study represent a modest endeavor to manufacture bioactive substances in Iraq, thereby substantially decreasing their price and rendering them accessible to the general populace at an affordable cost. This investigation will yield significant insights in addition to elucidating the physicochemical characteristics of DCPD. When attempting to predict the in vivo efficacy of these materials for bone repair, these properties are crucial. DCP cement and not using a delivered materials commonly has negative infusing capacity because of the liquid–stable degree department. In this study, a means of ionic modification for obtaining high strength of DCP and cement that was injectable with clinically acceptable properties was discovered. Ions doped with HA are used to improve injectable DCP cements and to enhance physicochemical properties.

CHAPTER TWO

METHODOLOGIES

2.1 Materials and Chemicals

Every chemical utilized in the synthesis was of reagent grade and was employed exactly as it was received.

In order to assess the in vitro bioactivity, simulated body fluid (SBF) was prepared in accordance with the methodology outlined in (Kokubo 1990) (Table 2.1). The preparation of simulated body fluid (SBF) solution followed methodologies that have been previously documented. In particular, HCl was added to a solution comprising NaCl, $CaCl_2$, $NaHCO_3$, KCl, $K_2HPO_4 \cdot 3H_2O$, $MgCl_2 \cdot 6H_2O$, and Na_2SO_4 in distilled water in order to achieve a pH value of 7.4. Our specimen was submerged in 20 mL of SBF solution via a 37°C water path.

Table 2.1 ionic composition of SBF and human blood plasma

Ions	**pH**	**Na^+**	**K^+**	**Ca^{2+}**	**Mg^{2+}**	**Cl^-**	**HCO_3^{3-}**	**HPO_4^{2-}**	**SO_4^{2-}**
SBF (mM)	7.0	140.0	5.5	2.7	1.6	145.7	3.3	1.5	1.5

All chemicals that are used to prepare SBF are purchased from (QREC, Auckland, New Zealand).

2.2 Equipment and Apparatus

In this study. The following apparatus and equipment were use as in table 2.2

Table 2.2. Apparatus used during the study period with the name of the Manufacturer and the country of Origin.

NO.	Equipment and apparatus	Company \ origin
1	X-Ray Diffraction (XRD)	Philips PW1730, Iran
2	FTIR spectroscopy (spectrometer)	Nicolet iS50, BCP LAB,Iraq
3	Field Emission Scanning Electron Microscope (FESEM) (EDX)	Zeiss-LEOModel1530
5	UV-Vis Spectroscopy	UV-3101PC;
6	A. A. Spectrometer (Perkin Elmer A Analyst 400).	(Perkin Elmer A Analyst 400). BCP LAB, Iraq
7	Gilmore needle apparatus (ASTM C266)	Singapore
8	2.5 T Universal Testing machine by INSTRON	Singapore

2.3 Chemicals

All chemicals used as received

Table 2.3. All Chemicals Used in the study with the Name of the Company Manufacturer and Country of Origin.

NO.	Chemicals	Company/origin
1	Calcium nitrate tetrahydrate ($Ca(NO_3)_2.4H_2O$	Sigma Aldrich
2	diammonium hydrogen phosphate	Sigma Aldrich

	$((NH_4)_2HPO_4$	
3	Potassium chloride	QREC, Auckland, New Zealand
4	Sodium chloride	Sigma Aldrich
5	Potassium chloride	Sigma Aldrich
6	Sodium hydrogen carbonate	Sigma Aldrich
7	Potassium phosphate	QREC, Auckland, New Zealand
8	Magnesium di chloride	Sigma Aldrich
9	Hydrochloric acid	Sigma Aldrich
10	Calcium chloride	Sigma Aldrich
11	Sodium sulfate	QREC, Auckland, New Zealand
12	Trisodium citrate	Sigma Aldrich
13	Cobalt nitrate hexahydrate $Co(NO_3)_2{\cdot}6H2O$	Sigma Aldrich
14	Zinc nitrate hexahydrate. $Zn(NO_3)_2$ 6H2O	Sigma Aldrich
15	Silver nitrate $AgNO_3$	Sigma Aldrich

2.4 Samples Preparation

2.4.1 Preparation of Hydroxyapatite (HA)

Solution of calcium nitrate (1 M) became prepared in a 100 ml of distilled water to form solution A. Diammonium hydrogen phosphate (0.6 M) turned into prepared in a hundred ml of distilled water to form solution B. The PH of each answers became adjusted to 10 through including ammonium hydroxide solution (NH_4OH). The answer b becomes introduced dropwise to solution a beneath consistent stirring; the resulting combination became stirred at room temperature for 30 min in the course of which the PH changed into maintained at 10 by using adding NH_4OH solution. The reaction aggregate becomes transferred to the 800w family microwave (sharp, model R-218ls) ready with a reflux condenser and became irradiated with 800w microwaves for 30 min. Ensuing white precipitate turned into filtered, washed with distilled water till PH changed into 7, dried inside the oven at 80 ºC for 17 h and calcined in muffle furnace at different temperatres (200, and 1000 ºC) for 2 h to obtain phase pure HA.

2.4.2 Preparation of Doped Hydroxyapatite

Ion doped HA were prepared using the same protocol as for HA (Sec 2.4.1), except that the corresponding amount of cationic dopant precursor was added to the solution of calcium nitrate.

Table 2.4 Dopant concentration, suggested formula, and calcination condition of different ions doped CaP series.

Dopant	**Formula**	**Dopant concentration (M)**	**Calcination temperature (°C)**
HA	$Ca_{10}(PO_4)_{6.}\,(OH)_2$		1000 (2h)
Ag^+	$Ca_{10-x}(PO_4)_6(OH)_2$	x= [0, 0.25, 0.5, 0.75, 1.00	1000 (2h)
Co^{2+} and Zn^{2+}	$Ca_{10-x}(PO_4)_6\,(OH)_2$	x= [0, 0.25, 0.5, 0.75 1.00]	1000 (2h)

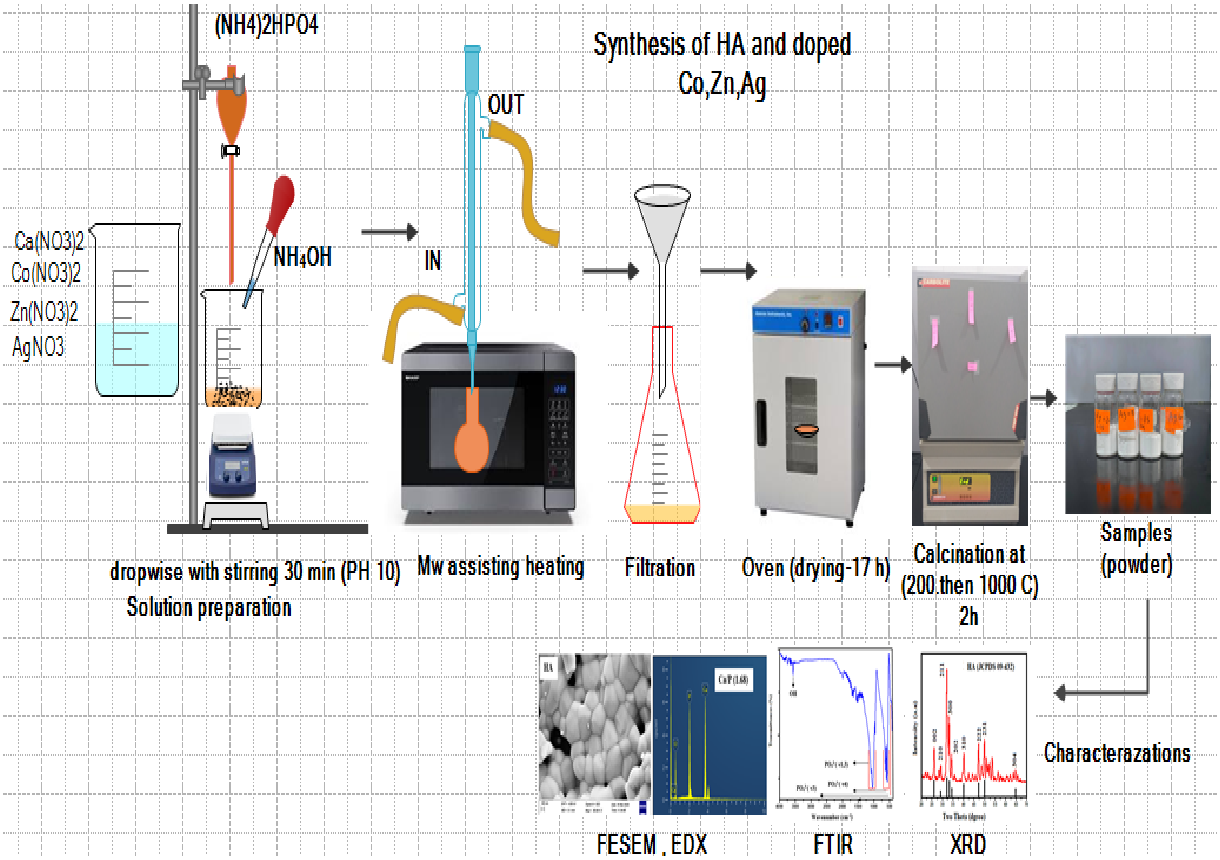

Figure 2.1 : Project outline Flowchart

2.5 Preparation of Dicalcium Phosphate Dihydrate (DCPD) Cement

In a mortar and pestle, HA and monocalcium phosphate monohydrate (MCPM) (MW 252.07, Sigma Aldrich (USA)) were combined to produce a particle known as the solid phase for cement preparation. For the preparation of DCPD cement, solid and liquid phases were combined in varying proportions of granules to liquid. The ingredients were combined through mixing until a uniform substance was formed. The material quantities utilized for the various PLRs are detailed in Table 2.2. After combining the solid and liquid phases by hand in a mortar for approximately one minute, the resulting material was transferred into cylindrical Teflon moulds with dimensions of (∅ = 6mm × ℓ = 12 mm). These moulds were subsequently making use of to determine the setting time make use of a Gilmore needle. Visual representations of the cement preparation process are presented in Figure 2.2.

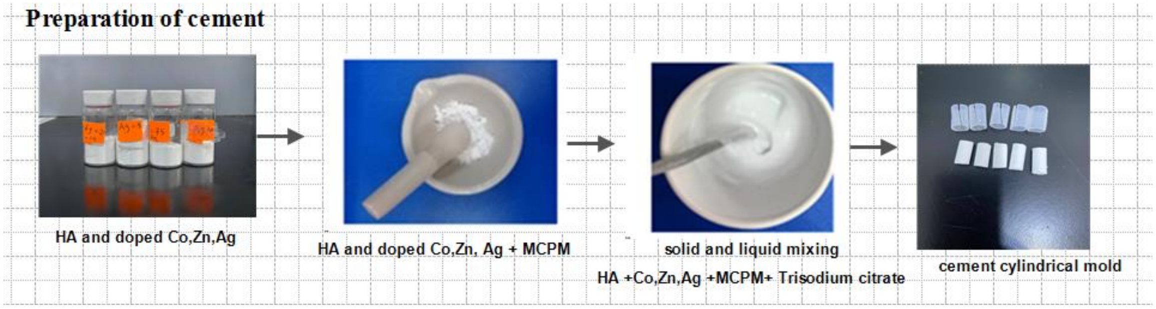

Figure 2.2: Preparation of cement

2.6 Setting Time Measurement

The Gilmore needle apparatus (ASTM C266) was utilized to determine the initial and ultimate setting durations of the prepared cement samples, as illustrated in figure 3.4. Cement material was deposited into a cylindrical Teflon mould with a dimension of 6mm × 12mm. A needle with a diameter of 2.12 mm and a mass of 113.4 g was positioned atop the specimen. Initial setting time was determined as the moment this needle etched the surface of the cement sample without leaving any indentations. Similarly, an additional needle with a diameter of 1.06 mm and a mass of 453.6 g was employed to measure the ultimate setting time [4]. In conclusion, the mean values of three measurements were utilized to record the initial and final configuration durations for each distinct PLR.

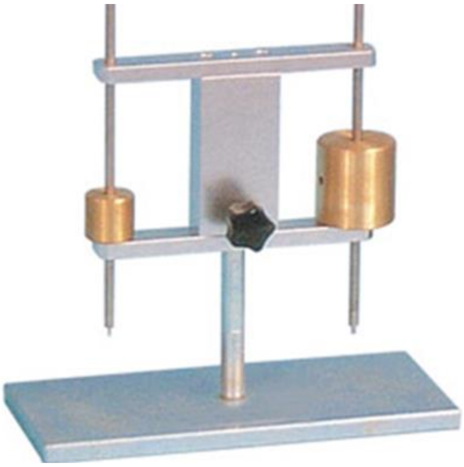

Figure 2.3: Gillmore needle for measurement of setting times

2.7 Injectability Measurement

A 2:1 DCP powder to liquid (P/L) ratio is manually combined for two minutes in order to achieve a uniform paste. The homogenized material is introduced into a commercial hypodermic featuring a 2 mm opening in the cartridge, which has a nominal capacity of 10 ml and a diameter of 13 mm. Then, for two minutes, a 5 kg compressive weight is vertically affixed on the highest point of the plunger. A series of injections are performed until the mixture becomes entirely unsuitable for injection Figure 2.4. In order to determine the percentage of injectability, one applies Equation [116].

$$\mathbf{Inj\% = W_F - W_A / W_F - W_E \times 100}$$

Where Inj% is the percentage injectability, W_E are the weight of the empty syringe, W_F is the weight of the syringe full of paste and W_A is the weight of the syringe after the injection.

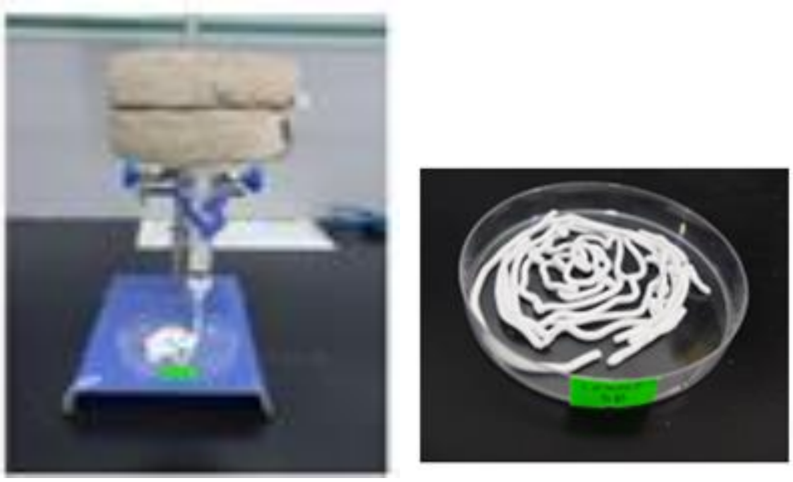

Figure 2.4: Injectability of cements

2.8 Compressive strength tests

Circular specimens of DCPD cement were fabricated using a Teflon mould with the following dimensions: 6 mm in diameter and 12 mm in height. For 1, 3, and 7 days, the specimens were submerged in 50 mL of SBF solution. In accordance with ASTM F451-99a [241 A], the cemented samples were extracted from the mould and meticulously polished with SiC sandpaper of 800 grains to reach a height of 12 mm on the extremities. The specimen's compressive strength was determined using an INSTRON Series X1S Automated Materials Tester-Version 8.33.00 with a crosshead speed of 0.5 mm/min after a 24-hour drying period at room temperature (Figure 2.5). The value of compressive strength is calculated by averaging five values.

Figure 2.5: 2.5 T Universal Testing machine by INSTRON.

2.9 Determination of ions release

In order to assess the ion release characteristics of DCP cement samples, the cement material was deposited into cylindrical Teflon moulds with a height of 12 mm and a diameter of 6.0 mm. Following preparation, samples were left to set at 25 °C for 24 hours. Submerging the set samples in SBF solution. The concentration and chemical composition of the SBF solution resembled those of the inorganic component of human plasma. It was prepared by dissolving reagents including NaCl, KCl, $K_2HP_4.3H_2O$, $NaHCO_3$, $(CH_2OH)_3CNH_2$, $MgCl_2.6H_2O$, $CaCl_2$, and Na_2SO_4 in deionized water per Kokubo's specification. Hydrochloric acid, HCl, was used to adjust the pH of the solution to 7.25. The samples were stored in SBF at 37 degrees Celsius for increments of 1, 3, and 7 days. Following that, the complete volume of the SBF was extracted in order to quantify its Ca^{2+} concentration, and subsequently re-fed with fresh solution. The concentrations of Ca^{2+}, Co^{2+} and Zn^{2+} were ascertained make use of Atomic Absorption Spectrometer.

2.10 Determination of *in vitro* drug release profiles

In order to prepare samples for the assessment of in vitro antibiotic release from the DCPD, the DCPD-containing antibiotic is positioned. Following preparation, samples are allowed to rest at ambient temperature for 24 hours. The specimens are submerged in 15 ml of SBF from each batch and incubated at 37 °C ± 0.5 °C. Aliquots of 2 ml of the solution are extracted directly from the receptacles at the following time intervals: 30 minutes, 1 hour, 2 hours, 3 hours, 4 hours, 7 hours, 12 hours, 24 hours, 48 hours, 72 hours, and 186 hours. A comparison is made between the quantity of antibiotic released and a calibration curve that is specific to the antibiotic produced in SBF. The quantification of antibiotic concentration in dissolution medium is accomplished through the utilization of ultraviolet–visible spectroscopy.

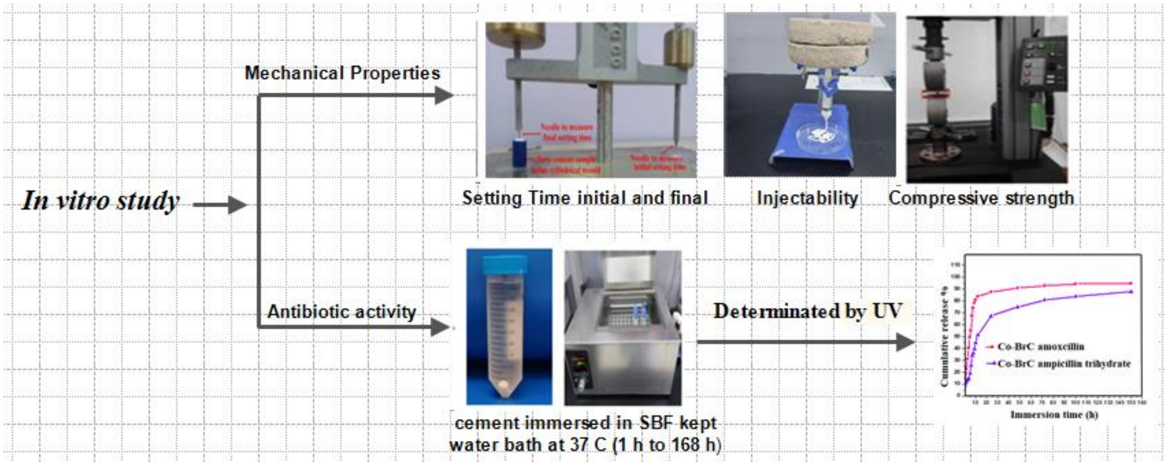

Figure 2.6: In vitro study, mechanical properties and antibiotic activity

2.11 Characterization

2.11.1 X-Ray Diffraction (XRD)

The crystallinity and phase integrity of each sample were assessed using an X-Ray Diffractometer (XRD, Bruker D8) set at 30 mA and 40 kV, employing CuKα radiation. The diffractograms were recorded at 2θ angles ranging from 20 to 80ϴ with a step size of 0.02° and a time interval of 1 second.

The degree of crystallinity was determined by utilising X-ray diffraction data to determine the proportion of crystalline phase present in the volume under analysis.

$X_C = 1 - (V_{1\,1\,2/3\,0\,0} / I_{3\,0\,0}) \times 100\%$ **(**Equation 3.1**)**

where X_C is the degree of crystallinity, $I_{3\,0\,0}$ is the intensity of (3 0 0) reflection and $V_{1\,1\,2/3\,0\,0}$ is the intensity of the hollow between (112) and (300) reflections.The average crystallite size was calculated using Scherrer's equation (Equation 3.2)

$$D = 0.9\lambda/\beta\cos\theta,$$

where D = crystallite size (nm), λ = wavelength of the X-ray used (nm), β = full width of the line at half of its maximum intensity in radians (FWHM),

θ = diffraction angle

For crystallite size calculations we used the FWHM at (002), (300), (222) and (310) reflections.

Calculation of lattice parameters a, c and mobile extent (v) of ion substituted cap shape were made using the unit-cellular application of holland and redfern. The percentage presence of secondary segment within the samples was decided from relative intensity ratio of the corresponding main levels by the use of (equation 3.3a ,b)

presence of section to be determined = relative intensity ratio of the section x one hundred (equation 3.3a)

Relative intensity ratio = depth of the predominant top of the section / ∑ intensity of primary peaks of all levels (equation three.3b)

2.11.2 Fourier Transform Infrared Spectroscopy (FTIR)

The KBr disc method was employed to corroborate the presence of functional groups using an FTIR spectrophotometer (Nicolet iS50 spectrometer). All spectra were acquired in transmission mode, covering the scanning range of 4000-400 cm^{-1}, with a total of 32 scans and a resolution of 4 $cm.^{-1}$.

2.11.3 Field Emission Scanning Electron Microscope (FESEM)

The morphology and microstructure of the DCPD and HA were analyzed using a FESEM (Zeiss-LEOModel1530) coupled to an Energy Dispersive X-Ray Analysis (EDX operating at a potential of 20 Kv. Prior to analysis, samples were gold or platinum-coated to prevent charge accumulation. make use of an EDX capable of operating at 15 kV of voltage, the elemental composition of the apatite layer that formed when samples were submerged in SBF was analyzed. To compute the average elemental composition, measurements were taken at five distinct locations.

2.11.4 UV-Vis Spectroscopy

On a Shimadzu 3101 UV-Vis-NIR spectrophotometer, the absorption spectra of antibiotic release from DCPD-loaded antibiotic samples are recorded within the 200-800 nm spectral range.

make use of a twofold monochromatic diffraction grinding framework and a photomultiplier R-928 indicator with a resolution of approximately 0.1 nm, the absorbance is determined.

CHAPTER THREE

RESULTS
AND
DISCUSSION

3.1 Synthesis of Hydroxyapatite (HA)

Synthesis of HA through a microwave assisted wet precipitation method, by exposing the reaction mixture with Ca/P molar ratio of 1.67 to 1050 W microwave radiations for 30 min. Calcination of this calcium deficient structure at 1000 °C for 2 h furnished HA. The reactions involved in the formation of HA during the chemical precipitation method can be expressed as follows (Equation 3.1 and 3.2).

$$10Ca(NO_3)_2.4H_2O + 6(NH_4)_2(HPO_4) + 9NH_4OH \rightarrow Ca_{10}(HPO_4)(PO_4)(OH) + 18NH_4NO_3 + 5H_2O \qquad \textbf{3.1}$$

$$Ca_{10}(HPO_4)(PO_4)(OH) \xrightarrow{1000\ °C} Ca_{10}(PO_4)_6(OH)_2 + H_2O \qquad \textbf{3.2}$$

3.1.1 X-Ray Diffraction (XRD) Analysis

XRD was employed to analyses the microstructure of HA powder at 1000 °C (figure 3.1). The phase analysis of size-controlled HA is evaluated in comparison to the ICDD (International Centre for Diffraction Data standard HA) (ICDD 00-009-0432) [117]. The comparison reveals that the principal diffraction peaks at 2θ values of 33.424°, 34.165°, 40.722°, 46.954°, and 52.271°, which correspond to the Miller planes (211), (300), (222) and (231), respectively, are in satisfactory agreement with the standard HA. The lattice parameters of the hexagonal structure of HA are as follows: a = b = 9.416; c = 6.863; and cell volume = 527.3 (Table 3.2). The outcome of the XRD analysis performed in the current study is highly consistent with the results that have been previously reported [118].

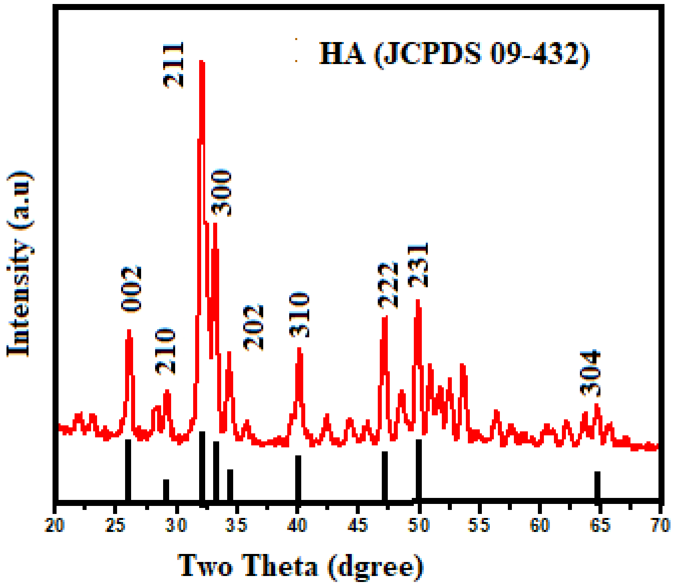

Figure 3.1: XRD pattern of HA calcined at 1000°C for 2 h.

Table 3.1: Lattice parameters of HA calcined at 1000 °C plus degree of crystallinity.

Samples	**Chemical formula**	**Lattice Parameter**			**X_c**	***D***
	$Ca_{10}(PO_4)_6\,(OH)_2$	***a* (Å)**	***c* (Å)**	***V* (Å)^3**	**(%)**	**(nm)**
Standard HA	$Ca_5(PO_4)_3(OH)$	9.418	6.884	528.8	----	----
HA (1000 °C)	$Ca_{10}(PO_4)_6(OH)_2$	9.418	6.866	527.4	86	98.23

3.1.2 FTIR spectra analysis

The FTIR spectra of HA calcinated at 1000°C) are illustrated in Figure 3.2. FTIR spectra of HA consists of four vibrational modes due to the presence of phosphate group and two bands due to the stretching of group. The sharp narrow band at wide band at 3572 cm^{-1} are associated with free hydroxyl group where this peak proves the presence of HA. The sharp peak at 474 cm $^{-1}$ was attributed to the vibrational mode of O-P, and the peaks at 572 cm $^{-1}$and 602 cm^{-1} were assigned to the O–P–O bending modes, the sharpness of the bands at 632, 602 and 572 cm^{-1} indicated the formation of a crystalline HA. While the absence of peak at 867 cm^{-1} in all samples confirmed that all our samples were free of HPO$_4^{2-}$ as a contaminant, moreover, no bands attributed to the carbonate group were observed at 867,1455 or 1423cm^{-1} the minor band at around 1633cm^{-1} was assigned to the bending vibration mode of O-H of adsorbed water [118].

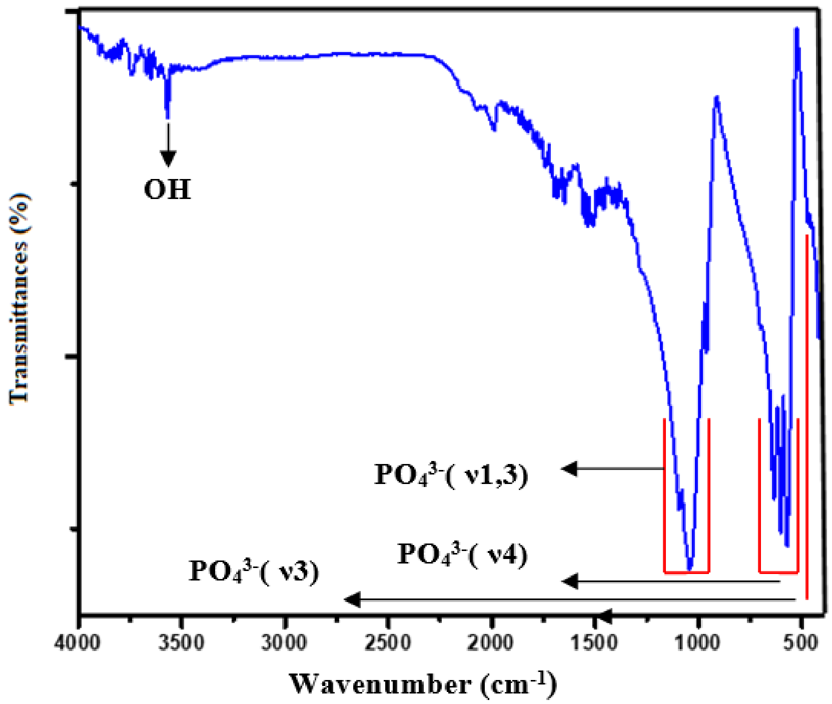

Figure 3.2: FTIR spectra of HA powder Calcined at 1000°C for 2 h.

3.1.3 FESEM Analysis

The FESEM micrographs of calcined extracted granules at 1000°C revealed the particles to be densely packed, irregularly shaped agglomerates (Figure 3.3). The formation of HA particles may involve one or more of the subsequent processes: a) the synthesis of HA through the nucleation and growth processes as a result of (b) the aggregation of constituent crystals via the molecular attractions of unique scale forces, the surface free energy is diminished. As a result, the surface-free energy decreases. Aggregation occurs when additional crystals are generated within the aggregates as a result of continuous residual supersaturation. Subsequently, this agglomerated particle undergoes a process of coalescence with other particles, resulting in the formation of secondary particles that grow in size. The HA demonstrated a greater particle size and a spherical morphology. Grain growth and crystallization of HA particles were affected by an increase in calcination temperature as a result of thermal energy absorption during the chemical synthesis process. There are fewer visible fissures in the sample.

As time progresses, the volume of HA decreases significantly, while their surface-to-volume ratios increase substantially. Nevertheless, the presence of Van der Waals interactions coupled with these enormous surface areas produced a strong inclination towards agglomeration. Particle characteristics, including size, shape, and surface texture, are influenced by these factors. The particle size significantly influences the profile of drug release exhibited by the particles. Additionally, the morphology of HA particles is influenced by the bone source, calcination temperature, and holding duration.

An increase in calcination temperature results in the particulates achieving a finer consistency. Additionally, the dietary habits, gender, and age of the animals from which the bone was extracted could potentially exert an impact. Therefore, further research is necessary in order to comprehend the impact that these biological factors have on the morphology.

3.1.4 Calcium-to-phosphorus ratio (Ca/P)

The elemental analysis performed using EDX permits the calculation of the Ca/P ratio, as shown in Table 3.2. The Ca/P ratio measured at 1000 °C was 1.68, which can be attributed to the existence of these trace elements. The value that approaches the theoretical HA ratio of 1.67. During the calcination phase at 1000 °C, the monophase of HA began to persist, which led to a close Ca/P ratio.

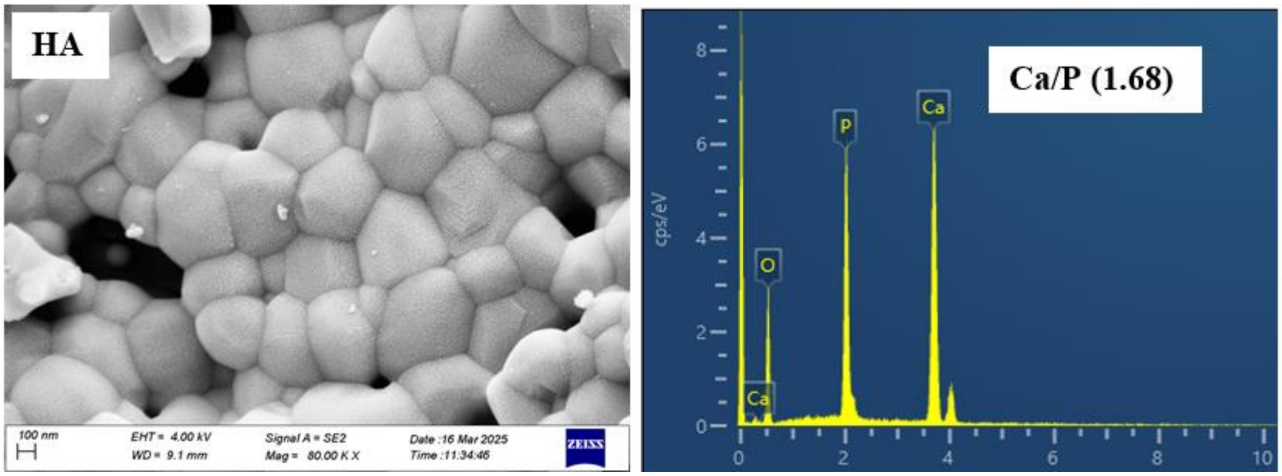

Figure 3.3: FESEM and EDX images showing the morphology and Ca/p of HA in 1000 °C.

Table 3.2: Ca/p ratio of calcined at 1000 °C

Samples HA	Elemental Composition (HA) (wt %)		Ca/P ratio
	Ca	P	
1000 °C	61.12	36.25	1.68

3.2 Cobalt Doped Hydroxyapatite (Co-HA)

Co doped HA(Co-HA) was synthesised in a same manner as HA mentioned in section 3.1 except that appropriate amount of $Co(NO_3)_2.6H_2O$ (Table 3.3) was added in the solution of calcium nitrate (Equation 3.3 and 3.4).

$$10\text{-}xCa(NO_3)_2 + XCo(NO_3)_2 + 6(NH_4)_2 HPO_4 + 9NH_4OH \rightarrow (Ca_{10-x} Co_x)(HPO_4)(PO_4)_5(OH) + 18NH_4NO_3 + 5H_2O \qquad \textbf{(3.3)}$$

$$Ca_{10-x} Co_x (HPO_4)(PO_4)_5(OH) \xrightarrow{1000\ °C} Ca_{10-X} Co_X (PO_4)_6 (OH)_2 + H_2O \qquad \textbf{(3.4)}$$

Where's (x) represent amount of Co^{2+} between 0 - 1.0 (Table 3.3)

Table 3.3: Nominal composition of Co-HA samples

Samples	**Reactants (mole)**		
	Ca^{2+}	**PO_4^{3-}**	**Co^{2+}**
HA	10.0	6.0	0.00
1Co-HA	9.75	6.0	0. 25
2Co-HA	9.50	6.0	0. 50
3Co-HA	9.25	6.0	0. 75
4Co-HA	9.00	6.0	1.00

3.2.1 Crystal Structure

The XRD sample of HA and Co-HA powders warmness handled at 1000 ºC are proven in (figure 3.4). XRD of pure HA is in properly settlement with the same old HA sample (ICDD 09-432) therefore indicating the formation of crystalline HA. Absence of mirrored image at 31.08º showed that the synthesized HA changed into freed from β-TCP as a secondary phase. XRD sample of Co-HA had been also in good settlement with the XRD pattern of crystalline HA, indicating the formation of pure phase Co-HA at a 1000 ºC, but a clear shift of peaks to higher 2θ values and reduction within the intensity of the XRD peaks turned into determined (fig 3.4).

The transferring of peaks to higher 2θ values became attributed to the substitution of large sized Ca^{2+} ions (0.99A^{o}) with smaller sized Co^{2+} ions (0.79A^{o}), at the same time as the discount in height depth became due to the discount in the degree of crystallinity of the samples. In preferred, the substitution of ions with smaller ionic radius and better price than the Ca^{2+} ions tend to supply doped analogues of HA with reduced of crystallinity. Lattice parameters alongside the a and c axis showed a slow decrease in duration with a growth in amount of Co^{2+} doping (table 3.4). This lower was attributed to the alternative of Ca^{2+} ion by using the smaller sized Co^{2+} ion.

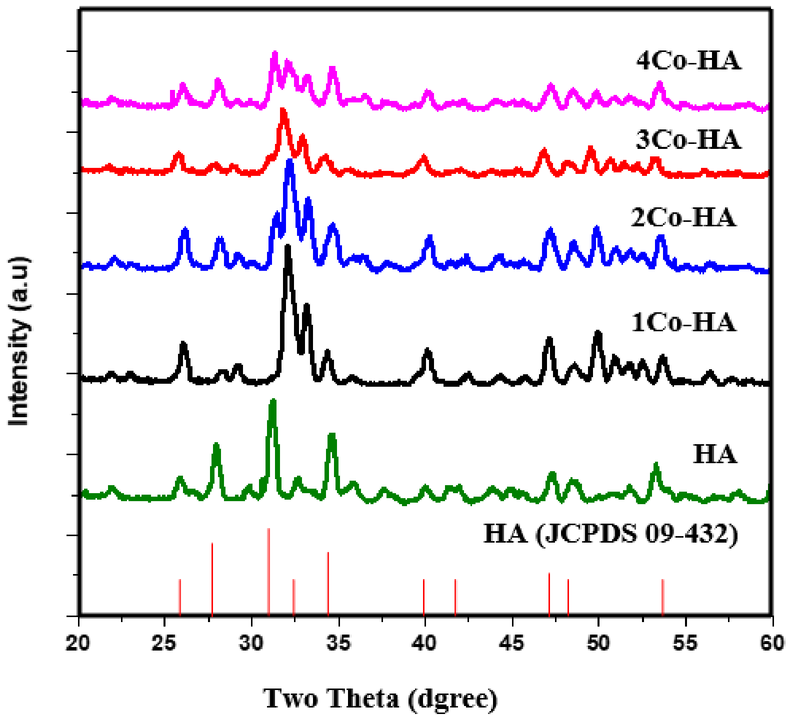

Figure 3.4: XRD patterns of HA and Co-HA series calcined at 1000 °C for 2h

Table 3.4: Lattice parameters and degree of crystallinity of HA and Co-HA samples

Samples	**Chemical formula**	**Lattice parameter**			**Degree of crystallinity % X_C**
		a-Axis (Å)	**c-Axis (Å)**	**Cell Vol. (Å)^3**	
HA	$Ca_{10}(PO_4)_6$	9.420	6.888	530.8	77
1Co-HA	$Ca_{9.75}Co_{0.25}(PO_4)_6(OH)_2$	9.417	6.880	526.5	68
2Co-HA	$Ca_{9.50}Co_{0.5}(PO_4)_6(OH)_2$	9.395	6.878	522.7	63
3Co-HA	$Ca_{9.25}Co_{0.75}(PO_4)_6(OH)_2$	9.387	6.869	520.3	57
4Co-HA	$Ca_{9.0}Co_{1.0}(PO_4)_6(OH)_2$	9.377	6.863	517.9	51

3.2.2 FTIR Spectra Analysis

FTIR spectra of HA and Co-HA samples contained all feature bands of the apatite structure (figure 3.5). The bands at 1084, 1033, 601 and 572 cm^{-1} were attributed to the symmetrical stretching and bending mode (ʋ3 and ʋ4) of PO_4^{3-} organisation. The two bands positioned at 952 and 474 cm^{-1} have been assigned to the symmetric stretching modes ʋ1and ʋ2 of the PO_4^{3-} enterprise respectively. A band positioned at 1622 cm^{-1} became assigned to absorbed water. A band centred at 3569 cm^{-1} was ascribed to the OH stretching mode. At the same time as the very small peaks placed at 870 and 1410 cm^{-1} were due to the b-kind substitution of the carbonate organization CO_3^{2-} . However, a top located at 1460 cm^{-1} end up assigned to a-kind CO_3^{2-} substitution of the carbonate institution. The doping of HA with Co^{2+} resulted inside the reduction extensive and sharpness of the bands, therefore confirming that the crystallinity of HA changed into reduced upon Co^{2+} doping. The depth of OH band steadily reduced due to the fact the doping of Co^{2+} ions extended in the ha lattice because of the partial alternative of OH– by using CO_3^{2-} (a-kind) of HA lattice. Moreover, the cut price inside the PO_4^{3-} bands is probably because of the ensuing changes in the bonding forces, which arise some of the ions due to weakening of the vibrational mode of P-O, and O-P-O [119].

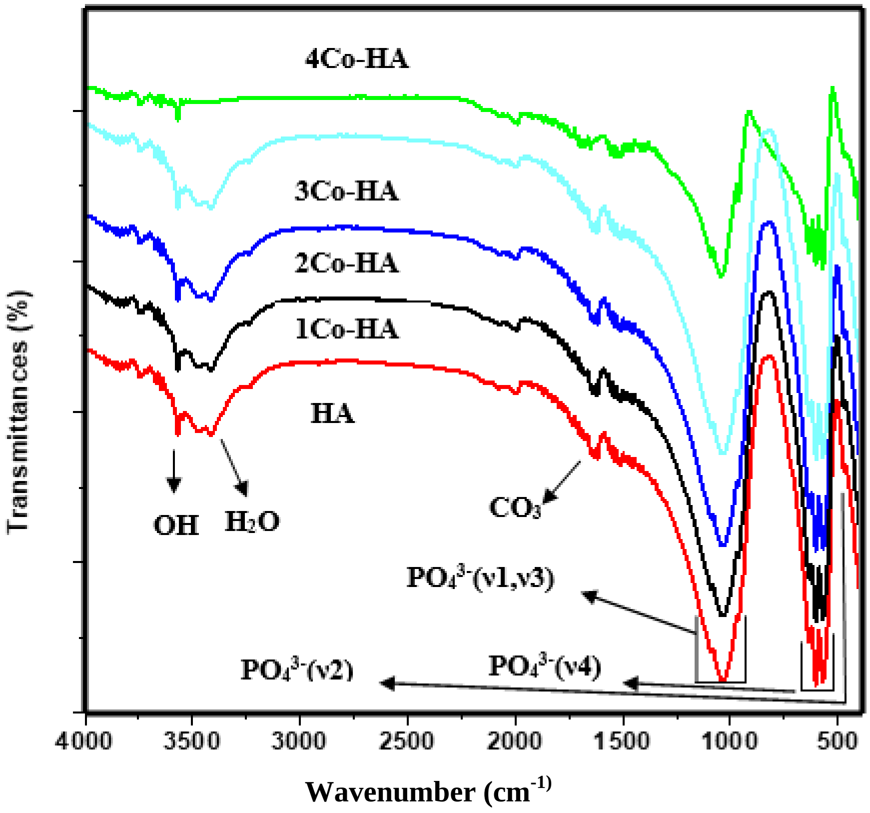

Figure 3.5 FTIR spectrum of HA and Co^{2+} doped HA calcined at 1000 °C.

3.2.3 FESEM Analysis

Figure. 3.6 show the FESEM micrographs of pure HA and Co-doped Powders calcined at 1000 °C. The microstructure of the powders consisted of microscale aggregates fused collectively. EDX evaluation of all samples showed that the Co^{2+} doping had successfully taken area and the amount of Co^{2+} doped inside the samples (figure.3.7). The modifications discovered in XRD height top, width and shifting (figure.3.4) along with the EDX statistics confirmed that the Co^{2+} doped had taken place inside the crystal structure in place of the mere adsorption of Co^{2+} ion at the floor of HA.

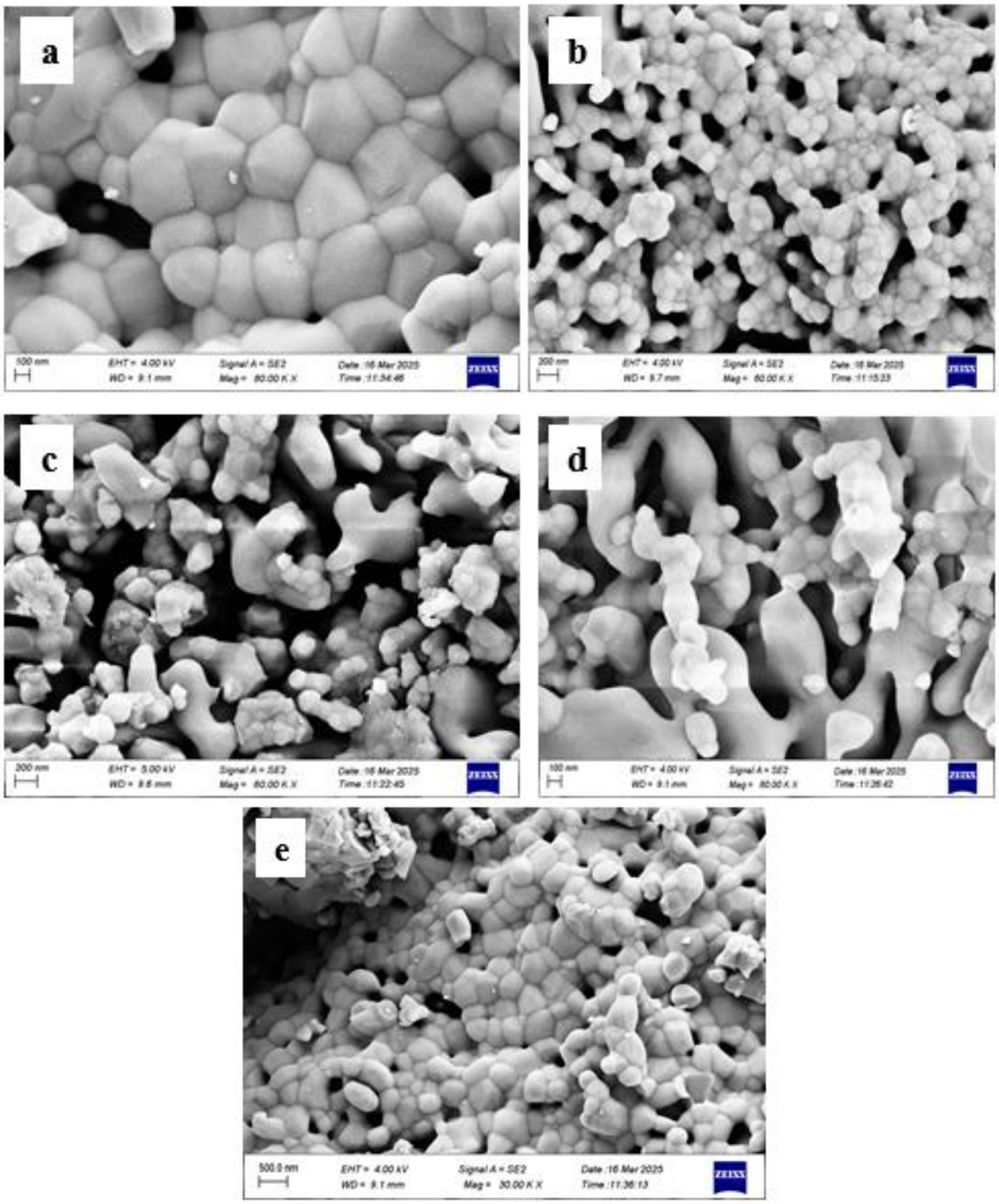

Figure 3.6: FESEM images of (a)pure HA, (b)1Co-HA, (c)2Co-HA, (d)3Co-HA and (e) 4Co-HA calcined at 1000 °C.

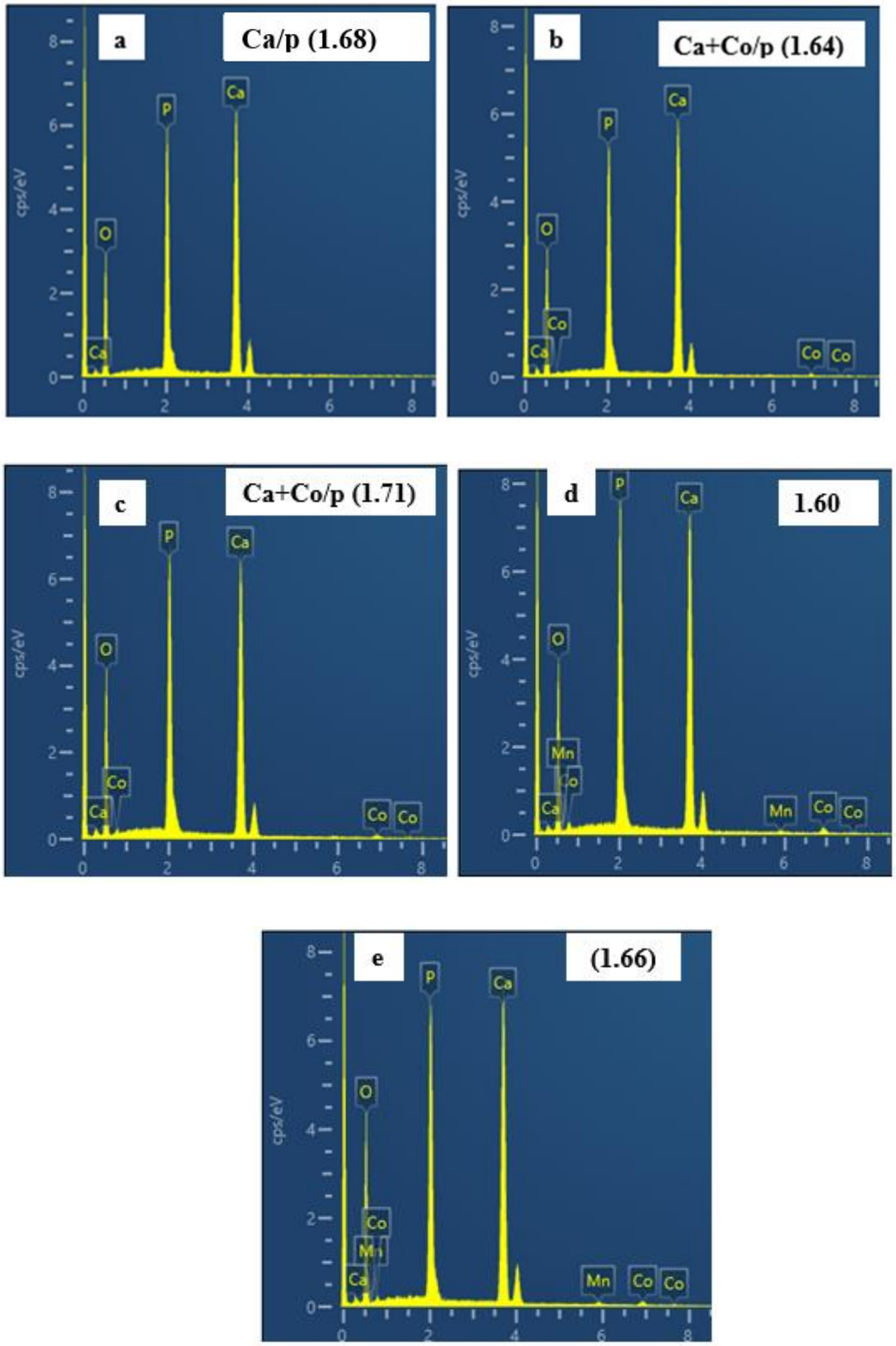
a
Ca/p (1.68)
cps/eV
O
P
Ca
Ca
b
Ca+Co/p (1.64)
O
Co
Ca
P
Ca
Co
Co
c
Ca+Co/p (1.71)
O
Co
Ca
P
Ca
Co
Co
d
1.60
P
Ca
O
Mn
Co
Ca
Mn
Co
Co
e
(1.66)
P
Ca
O
Co
Mn
Ca
Mn
Co
Co
0
2
4
6
8

Figure 3.7: EDX analysis for (a) Pure HA, (b)1Co-HA, (c)2Co-HA, (d)3Co-HA and (e) 4Co-HA

3.3 Znic Doped Hydroxyapatite (Zn-HA)

Zn doped HA(Co-HA) was synthesised in a same manner as HA mentioned in section 3.1 except that appropriate amount of $Zn(NO_3)_2.6H_2O$ (Table 3.5) was added in the solution of calcium nitrate (Equation 3.5 and 3.6).

$$10\text{-}xCa(NO_3)_2 + XZn(NO_3)_2 + 6(NH_4)_2\,HPO_4 + 9NH_4OH \rightarrow$$
$$(Ca_{10\text{-}x}\,Zn_x)\,(HPO_4)(PO_4)_5(OH) + 18NH_4NO_3 + 5H_2O \qquad \textbf{(3.5)}$$

$$Ca_{10\text{-}x}\,Zn_x\,(HPO_4)(PO_4)_5(OH) \xrightarrow{1000\ °C} Ca_{10\text{-}X}\,Zn_X\,(PO_4)_6\,(OH)_2 + H_2O \qquad \textbf{(4.6)}$$

Where's (x) represent amount of Zn^{2+} between 0 - 1.0 (Table 3.5)

Table 3.5: Nominal composition of Zn-HA samples

Samples	**Reactants (mole)**		
	Ca^{2+}	**PO_4^{3-}**	**Zn^{2+}**
HA	10	6.0	0.00
1Zn-HA	9.75	6.0	0. 25
2Zn-HA	9.50	6.0	0. 5
3Zn-HA	9.25	6.0	0. 75
4Zn-HA	9.00	6.0	1.00

3.3.1 Crystal Structure

The XRD pattern of HA and Zn-HA powders warmth handled at 1000 ºC are shown in (figure 3.8). XRD of pure HA is in correct settlement with the usual HA pattern (ICDD 09-432) for this reason indicating the formation of crystalline HA. Absence of reflection at 31.08º showed that the synthesized ha became freed from β-TCP as a secondary section. XRD pattern of Zn-HA had been additionally in desirable settlement with the XRD pattern of crystalline ha, indicating the formation of pure phase Zn-HA at one thousand ºC, however a clean shift of peaks to better 2θ values and reduction within the intensity of the XRD peaks became located (figure 3.8).

The incorporation of Zn^{2+} into the HA lattice led to a moving of diffraction peaks to better 2θ values and bargain inside the depth of the XRD peaks turned into moreover placed, which were attributed to the substitution of smaller sized Zn^{2+} ions (0.74 A°) in place of Ca^{2+} ions (0.99 A˚). No additional tiers have been detected inside the XRD styles, indicating that a strong solution and Zn^{2+} ions has been fashioned. Lattice parameters along the a and c axis showed a slow lower in length with a growth in amount of Zn^{2+}. This lower became attributed to the alternative of Ca^{2+} ion by using the smaller sized Zn^{2+} ion. The lattice parameter *a*- decreased from 9.412A˚ to 9.379A˚ and c-axis parameters decreased to 6.881A˚ from 6.863A˚ upon incorporating Zn ions into the structure (4Zn- HA). The substitution of smaller-sized Zn^{2+} Into the structure also resulted in the lower of unit cell quantity from 522.6 $Å^3$ to 510.9$Å^3$ (Table 3.6).

Table 3.6: Lattice parameters and degree of crystallinity of pure HA and Zn-HA series heat treated at 1000 °C.

		Lattice parameters				
Sample	**Chemical formula**	**a (Å)**	**c (Å)**	**c/a**	**V ($Å^3$)**	**Xc (%)**
HA	$Ca_{10}(PO_4)_6(OH)_2$	9.417	6.885	0.731	525.8	78
1Zn-HA	$Ca_{9.75}$-$Zn_{0.25}$ $(PO_4)_6(OH)_2$	9.412	6.881	0.731	522.6	73
2ZnHA	$Ca_{9.50}Zn_{0.50}$ $(PO_4)_6(OH)_2$	9.391	6.877	0.732	519.9	66
3ZnHA	$Ca_{9.25}Zn_{0.75}$ $(PO_4)_6(OH)_2$	9.385	6.868	0.731	515.5	56
4ZnHA	$Ca_{9.0}Zn_{1.00}$ $(PO_4)_6(OH)_2$	9.379	6.863	0.731	510.9	48

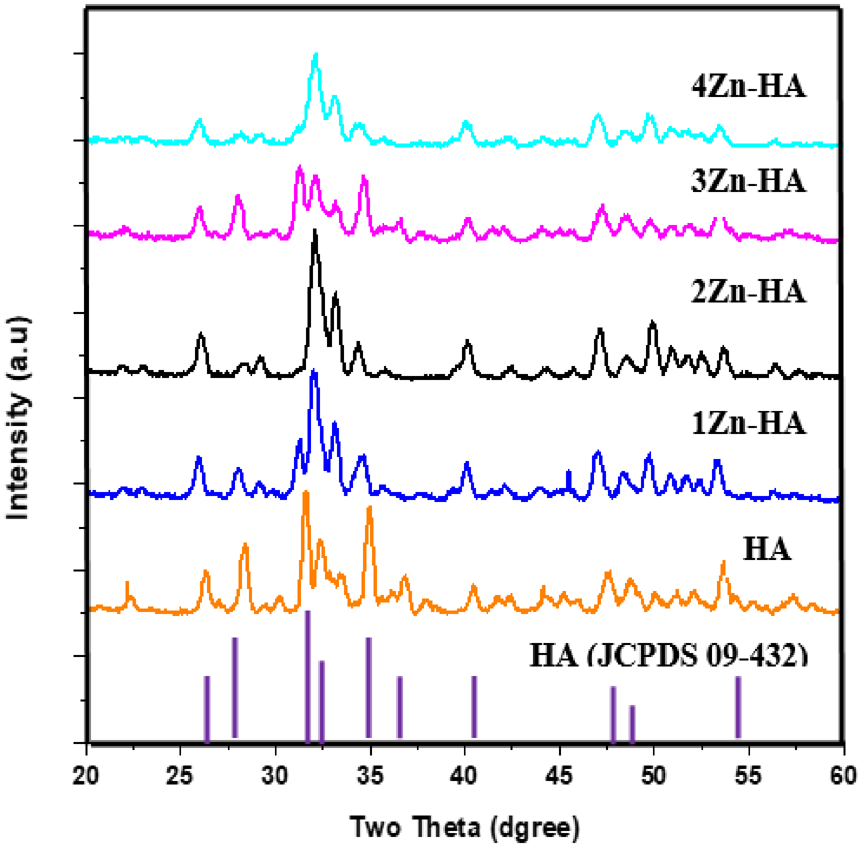

Figure 3.8: XRD diffraction patterns of HA and Zn-HA series calcined at 1000 °C for 2h

3.3.2 FTIR Spectra Analysis

FTIR spectra of HA and Zn-HA samples contained all function bands of the apatite shape (Figure 3.9). The bands at 1084, 1033, 601 and 572 cm^{-1} had been attributed to the symmetrical stretching and bending mode (ʋ3 and ʋ4) of PO_4^{3-} group. The two bands placed at 952 and 474 cm^{-1} had been assigned to the symmetric stretching modes ʋ1and ʋ2 of the PO_4^{3-} organization respectively. A band placed at 1622 cm^{-1} become assigned to absorbed water. A band targeted at 3569 cm^{-1} grow to be ascribed to the OH^- stretching mode. Furthermore, the liberation modes of OH^- ions have been detected at 630 cm^{-1}, even as the very small peaks positioned at 1410 cm^{-1} have been because of the b-type substitution of the carbonate organization CO_3^{2-} However, a peak located at 1560 cm^{-1} was assigned to A-type CO_3^{2-} substitution of the carbonate group**.** doping of HA with Zn^{2+} resulted within the bargain in depth and sharpness of the bands, consequently confirming that the crystallinity of ha became reduced upon Zn^{2+} doping. The intensity of OH^- band progressively reduced as the doping of Zn^{2+} ions accelerated inside the ha lattice due to the partial opportunity of OH^- through CO_3^{2-} (a-type) of HA lattice. Moreover, the discount inside the PO_4^{3-} bands is probably due to the consequent modifications within the bonding forces, which occur most of the ions due to weakening of the vibrational mode of P-O, and O-P-O.

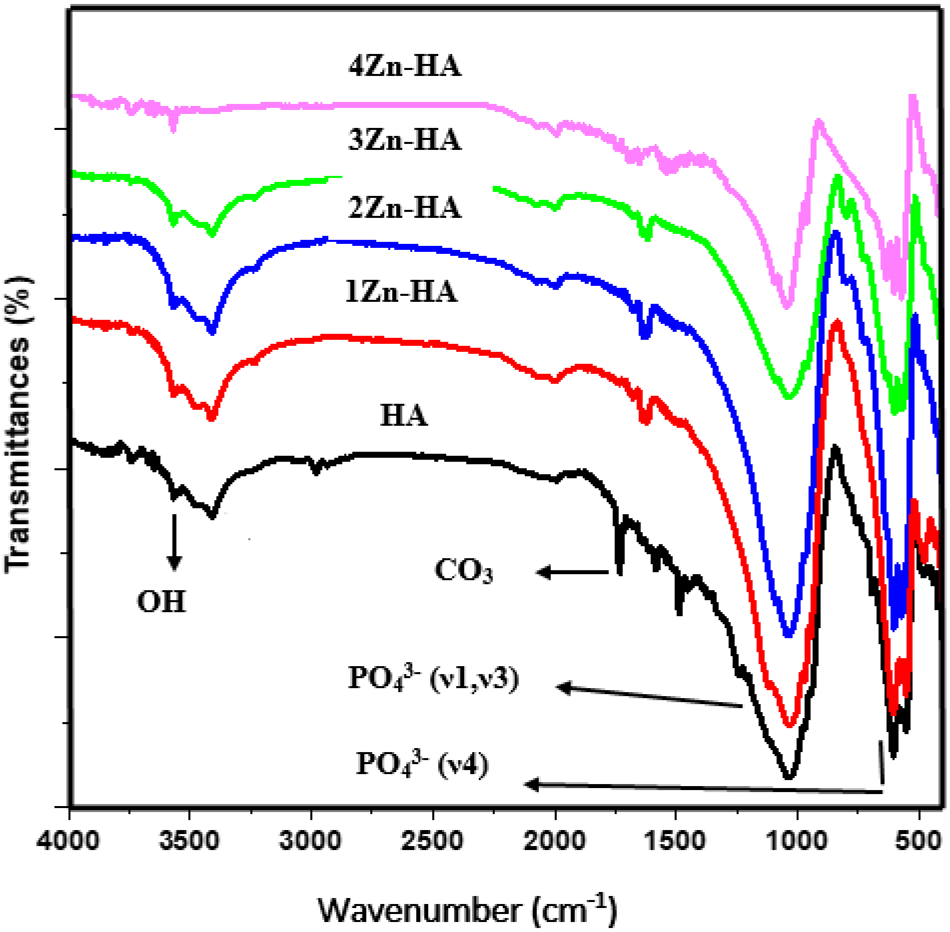

Figure 3.9: FTIR spectrum of HA and Zn^{2+} doped HA calcined at 1000 °C.

3.3.3 FESEM Analysis

Figure. 3.10 show the FESEM micrographs of pure HA and Zn-doped Powders calcined at 1000 °C. The microstructure of the powders consisted of microscale aggregates fused together. EDX evaluation of all samples showed that the Zn^{2+} doping had successfully taken area and the amount of Zn^{2+} substitution in the samples (Figure.3.11). The modifications observed in XRD height, width and moving (figure.3.8) alongside the EDX records confirmed that the Zn^{2+} substitution had taken place in the crystal structure instead of the mere adsorption of Zn^{2+} ion on the surface of HA.

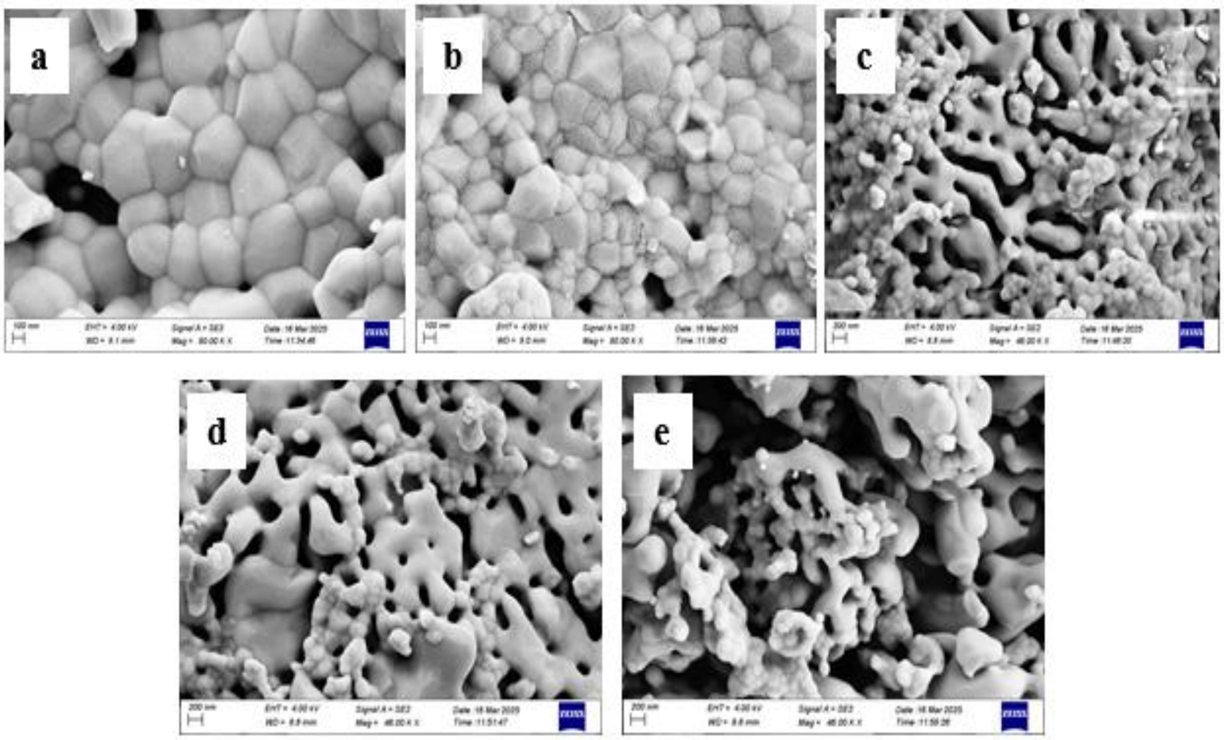

Figure 3.10 FESEM images of (a)pure HA, (b)1Zn-HA, (c)2Zn-HA, (d)3Zn-HA and (e) 4Zn-HA calcined at 1000 °C.

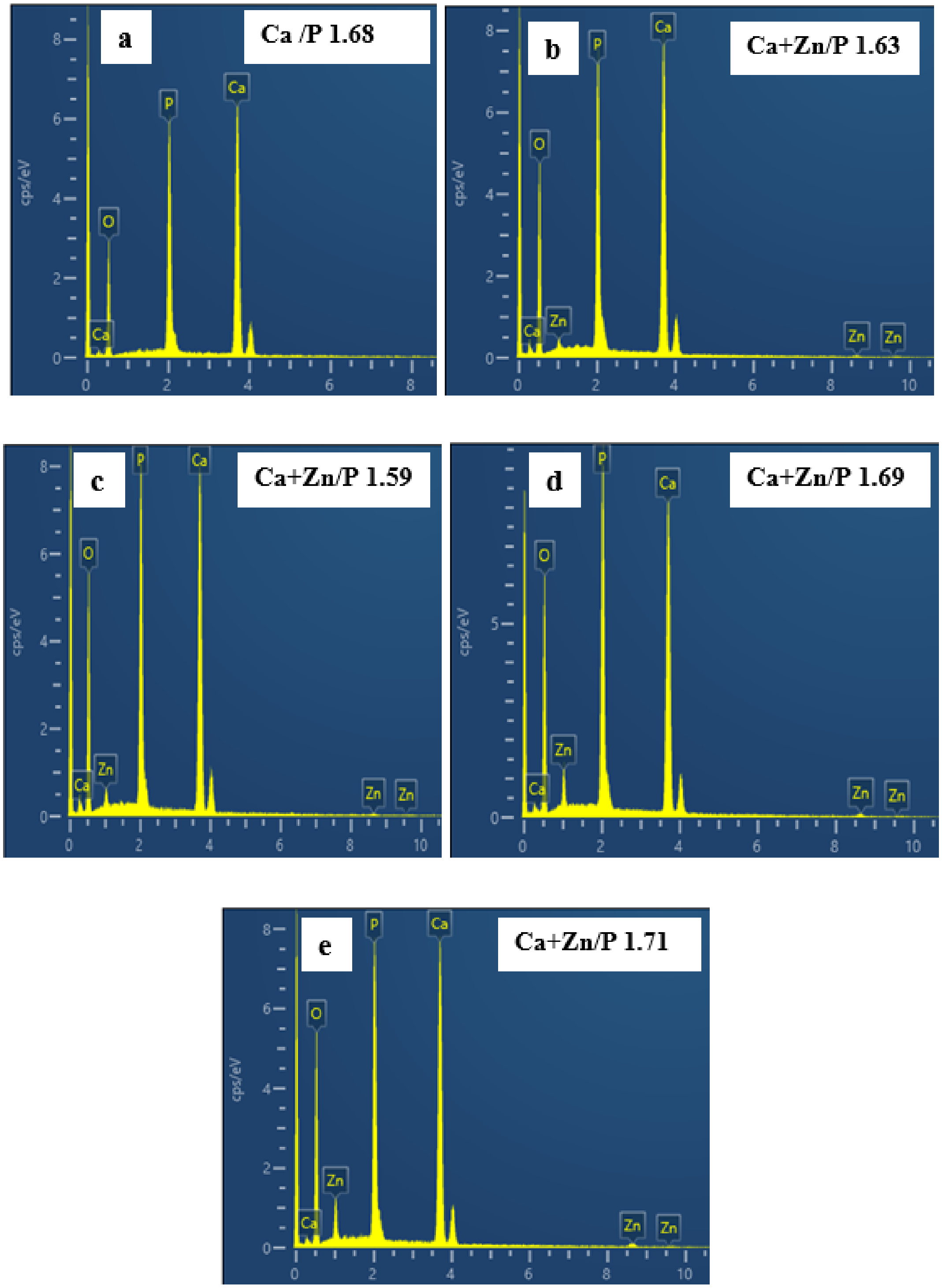

Figure 3.11: EDX analysis for (a) Pure HA, (b)1Zn-HA, (c)2Zn-HA, (d)3Zn-HA and (e) 4Zn-HA

3.4 Sliver Doped Hydroxyapatite (Ag-HA)

Synthesis of HA through a microwave assisted wet precipitation method is reported in section 3.1, Ag-HA samples were prepared in exactly the same manner except the initial Ca+Ag/P ratio was adjusted to 1.67 to ensure successful incorporation of the Ag^+ ions into the structure (Equation 4.7 and 4. 8).

$$10\text{-}XCa(NO_3)_2 + XAgNO_3 + 6(NH_4)_2HPO_4 + 9NH_4OH \rightarrow (Ca_{10-x}Ag_x)(HPO_4)(PO_4)_5(OH) + 18NH_4NO_3 + 9H_2O \quad \textbf{(4.7)}$$

$$Ca_{10-x}Ag_x(HPO_4)(PO_4)_5(OH) \xrightarrow{1000\ ^\circ C} C10_{-x}Ag_x(PO_4)_6 + H_2O \quad \textbf{(4. 8)}$$

Where's (x) represent amount of Ag^+ between 0 – 1.00 (Table 4.6)

Table 3.7: Nominal composition of Ag-HA samples

	Reactants (mole)		
Samples	**Ca^{2+}**	**$(PO_4)^{3-}$**	**Ag^+**
HA	10	6.0	0.00
1Ag- HA	9.75	6.0	0.25
2Ag- HA	9.50	6.0	0.50
3Ag- HA	9.25	6.0	0.75
4Ag- HA	9.00	6.0	1.00

3.4.1 Crystal Structure

Phase composition of Ag-HA was analyzed through powder XRD (Fig.3.12), XRD data showed pattern similar to that of the crystalline HA (ICDD 09-432) discussed in section 3.1.1, confirming the formation of HA. Normally, multiplied quantity of ag ion substitution caused a lower in the intensity of diffraction peaks as well as the peak broadening, suggesting that the particle length of the ensuing Ag-HA had decreased and the crystallinity of the particles had deteriorated. Doping of HA with silver ions prompted the moving of peaks in the direction of lower diffraction angle, which changed into attributed to a hit doping of ha lattice with larger sized Ag ions ensuing in improved cell dimensions. The unit cell parameters of all samples are presented in Table 3.8. The lattice parameters *a*=*b* and *c* increased with increasing amount of silver ions. Increase in the cell parameters was ascribed to the substitution of larger sized Ag^+ ions (1.28 Å) in place of Ca^{2+} (0.99 Å) in the β-TCP lattice. Crystallite size of the particles also decreased with the increase in Ag^+ doping (Table 3.8).

Table 3.8: Lattice parameters and degree of crystallinity of pure HA and Ag-HA series heat treated at 1000 °C.

		Lattice parameters				
Sample	**Chemical formula**	**a (Å)**	**c (Å)**	**c/a**	**V ($Å^3$)**	**Xc (%)**
HA	$Ca_{10}(PO_4)_6(OH)_2$	9.415	6.883	0.731	525.6	82
1Ag-HA	$Ca_{9.75}$-$Ag_{0.25}$ $(PO_4)_6(OH)_2$	9.419	6.886	0.731	528.7	72
2AgHA	$Ca_{9.50}Ag_{0.50}$ $(PO_4)_6(OH)_2$	9.424	6.891	0.732	534.5	67
3AgHA	$Ca_{9.25}Ag_{0.75}$ $(PO_4)_6(OH)_2$	9.429	6.903	0.732	539.8	60
4AgHA	$Ca_{9.0}Ag_{1.00}$ $(PO_4)_6(OH)_2$	9.436	6.910	0.732	543.2	54

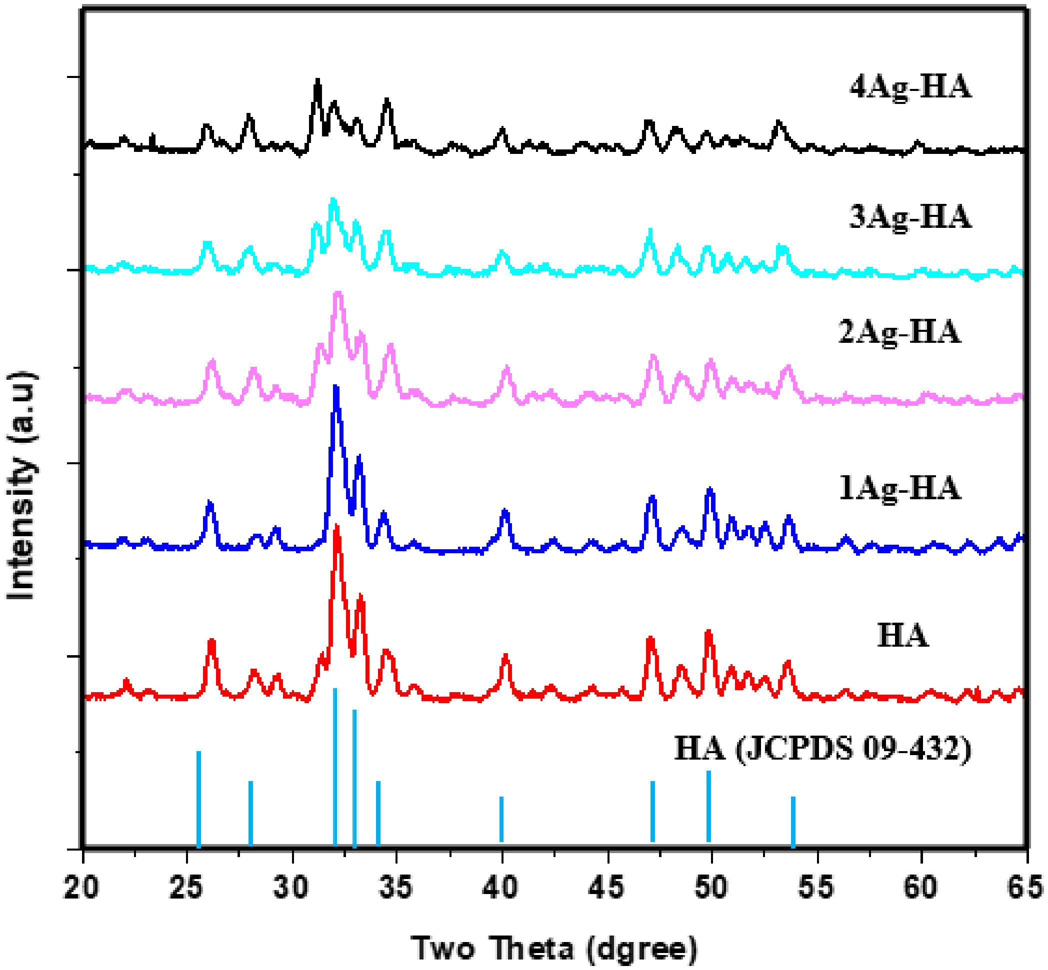

Figure 3.12: XRD diffraction patterns of HA and Zn-HA series calcined at 1000 °C for 2h

3.4.2 FTIR Analysis

FTIR spectra of HA confirmed the presence of band at 3443 cm^{-1}, (Figure 3.13). The peaks at 1036 cm^{-1} and 540 cm^{-1} have been assigned to the PO_4^{3-} groups. The peaks at 1112 and 1077 cm^{-1} were ascribed to the stretching (υ3) of P–O bond of phosphate organization. The height at 974 cm^{-1} modified into assigned to the symmetric stretching (υ1) of the P–O bond in phosphate group. Sharp peaks at 603 and 554 cm^{-1} corresponded to bending mode (υ4) of the O–P–O linkage in phosphate agencies of HA. Incorporation of Ag^+ ions in ha pattern resulted inside the shifting of phosphate band from 969–1122 cm^{-1} to 946–1125 cm^{-1}. The PO_4^{-3} bands have become broader for Ag-HA samples as compared with natural HA, consequently confirming the formation of Ag-HA samples with reduced diploma of crystallinity, a style this is according with the XRD records (Figure.3.12).

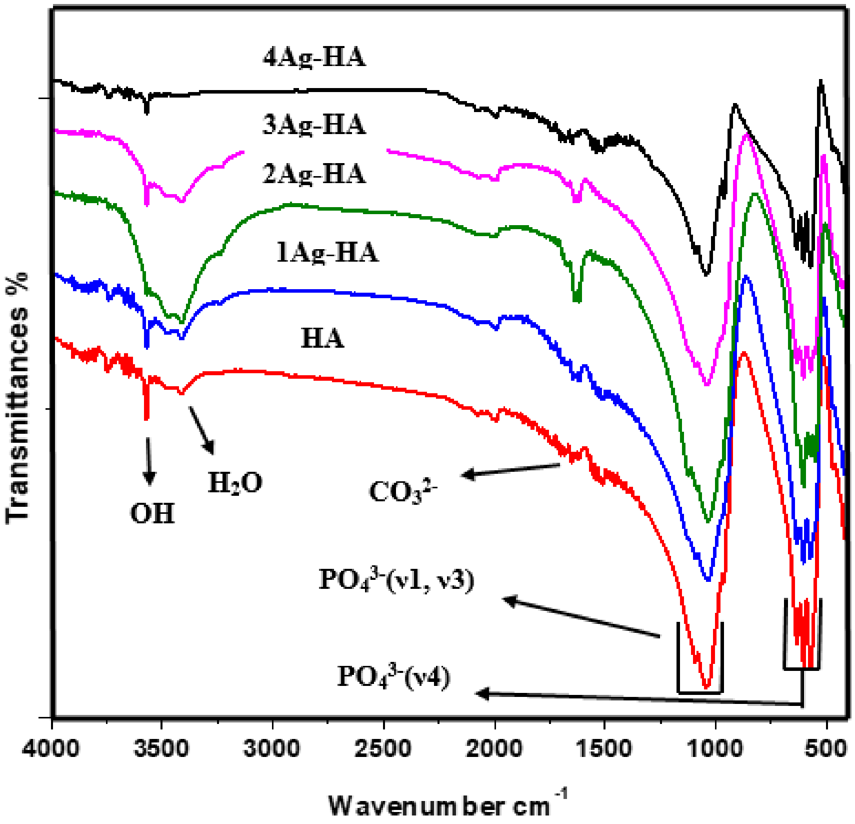

Figure 3.13: FTIR spectrum of HA and Ag^+ doped HA calcined at 1000 °C.

3.4.3 FESEM Analysis

FESEM images showed the formation of HA powder with prolate spheroidal phase structure (Figure.3.14). Micrographs of 1Ag-HA and 4Ag-HA, confirmed that the particles became irregular in shape and highly agglomerated upon silver doping. EDX analysis of all samples showed that the Ag^{+} doping had efficaciously taken location and the quantity of Ag^{+} substitution in the samples (discern.3.15). The changes located in XRD peak top, width and transferring (Figure.3.12) together with the EDX facts showed that the Ag+ substitution had taken region within the crystal structure.

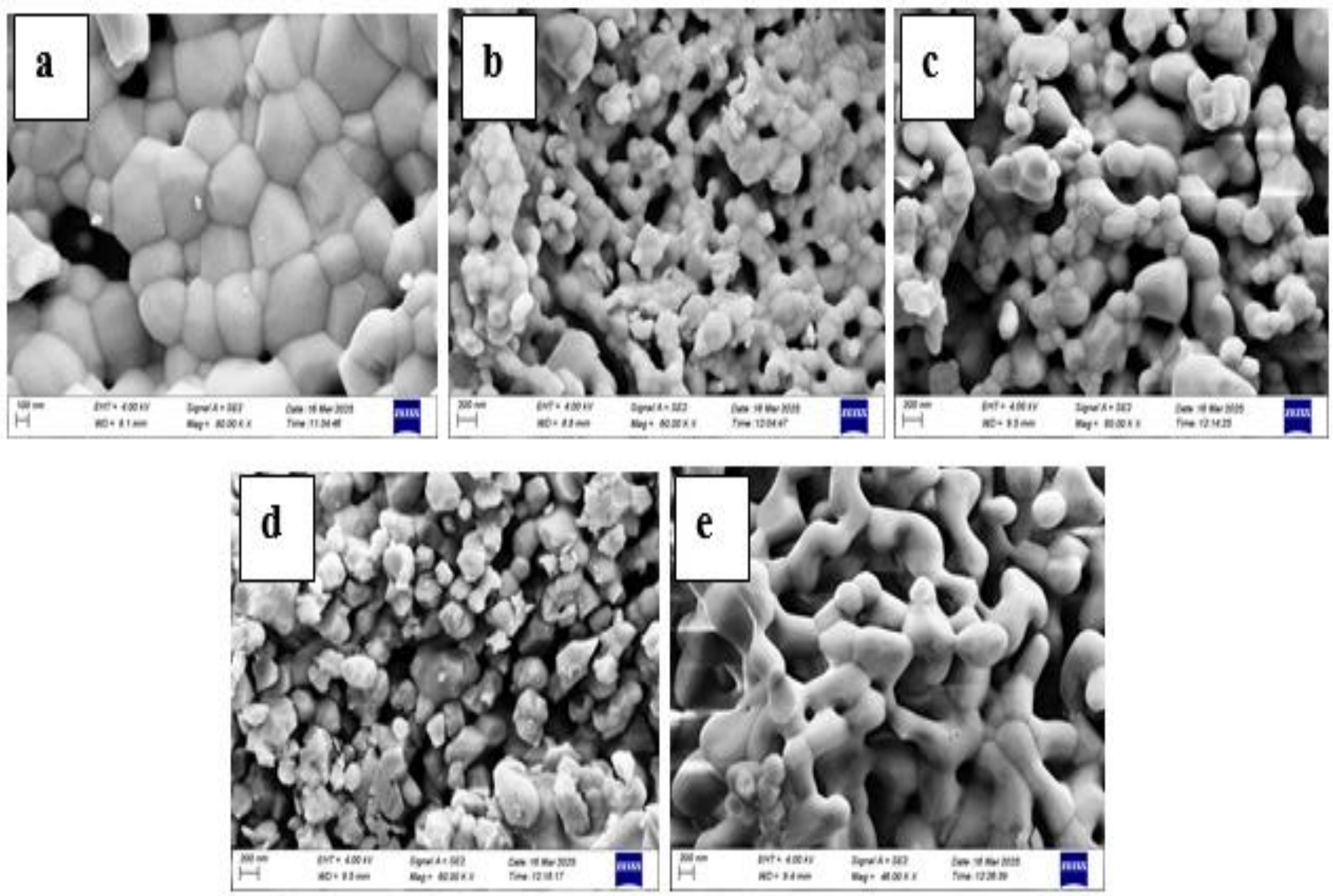

Figure 3.14: FESEM images of (a)pure HA, (b)1Ag-HA, (c)2Ag-HA, (d)3Ag-HA and (e) 4Ag-HA calcined at 1000 $^{\circ}$C.

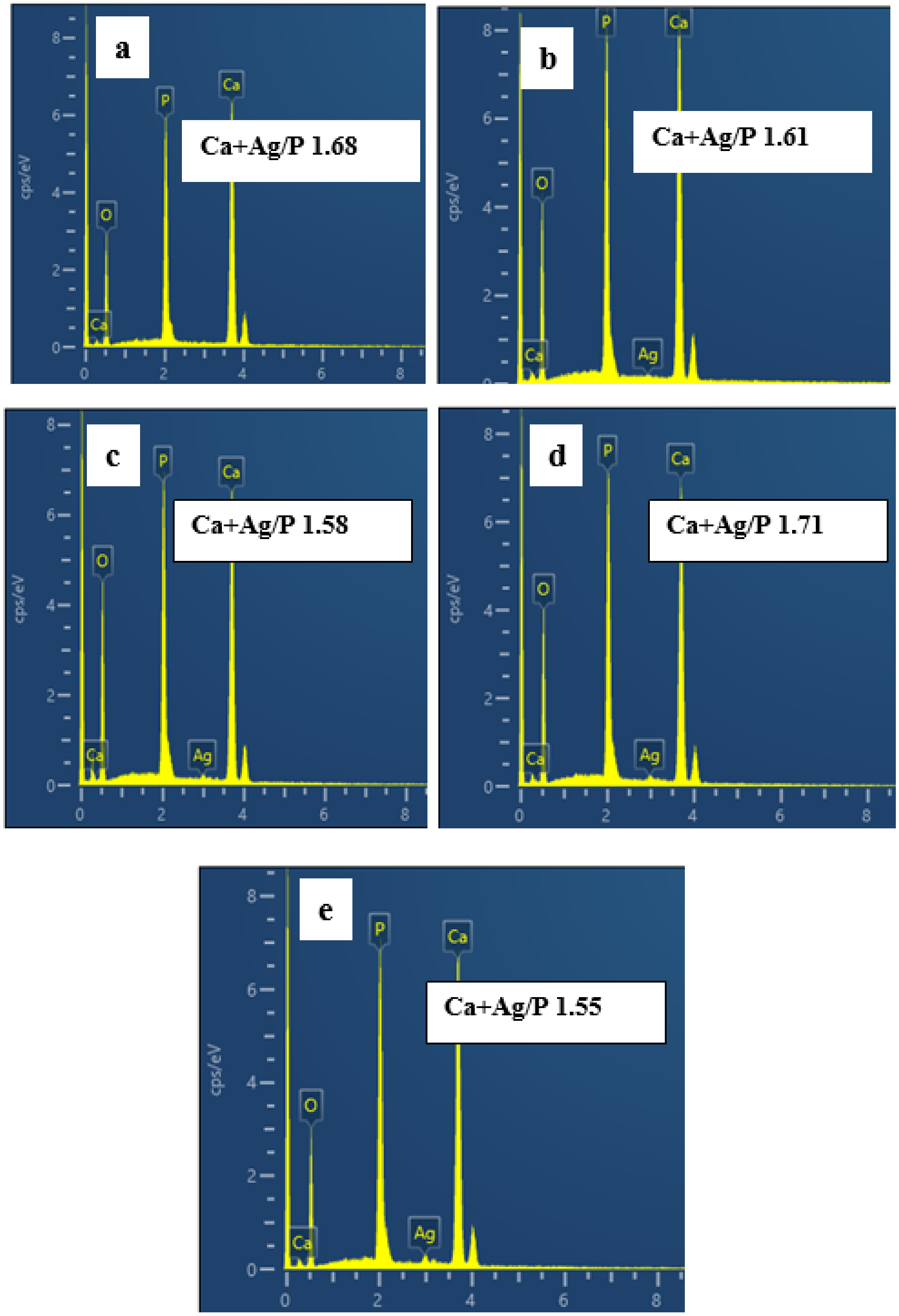

Figure 3.15: EDX analysis for (a) Pure HA, (b)1Ag-HA, (c)2Ag-HA, (d)3Ag-HA and (e) 4Ag-HA

CHAPTER FOUR

PREPARATION AND CHARACTERIZATION, MECHANICAL PROPERTIES AND BIOACTIVITY OF Co, Zn AND Ag DOPED DICALCIUM PHOSPHATE (DCP) CEMENTS

4. Preparation of Brushite Cement (Brc)

Brushite was prepared by hand mixing HA (1gm) and monocalcium phosphate monohydrate (0.5gm) in the presence of (0.8 ml, 0.5M trisodium citrate). The mixture was mixed until a smooth paste was formed.

4.1 Crystal Structure

Segment analysis of the brushite turned into determined via the use of XRD. The XRD pattern of brushite contained peaks at 21.15°, 29.55°, 30.77°, 34.31°, 37.22°, 41.77° and 42.29°, which were ascribed to the (12 -1), (14 -1), (121), (15 0), (141), (15 -2) and (260) planes of crystalline brushite (ICDD 72-0713) (figure 4.1). The lattice data obtained for pure brushite confirmed the formation of monoclinic crystalline brushite with lattice parameters a= 5.099Å, b= 15.362 and c= 5.491 Å, $\alpha = \beta = 90^{\circ}$, and $\gamma = 120^{\circ}$.

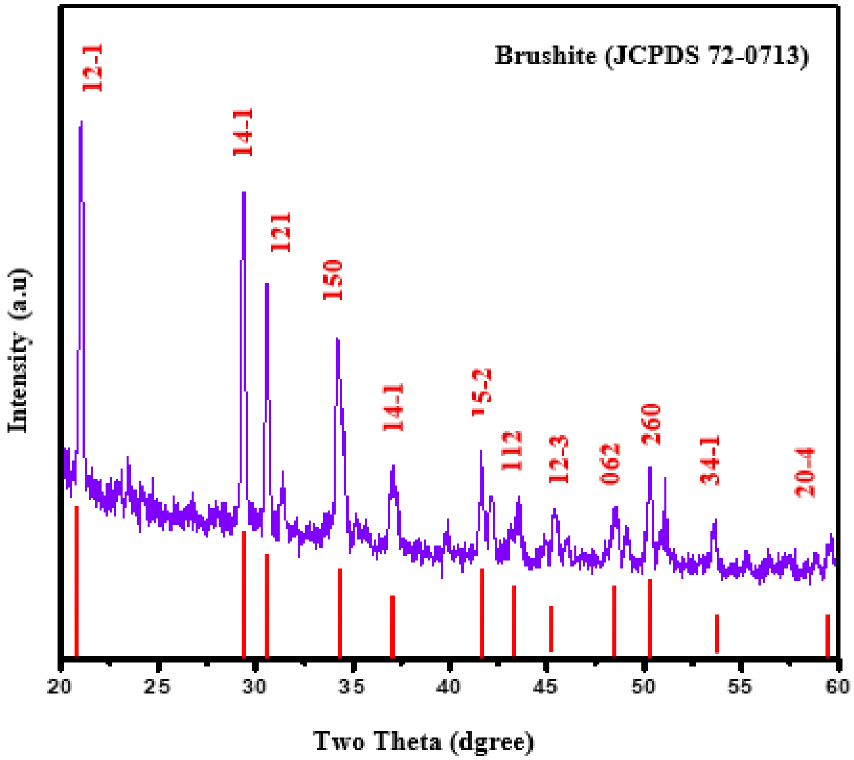

Figure 4.1: XRD patterns of brushite cements with reference pattern (JCPDS 72-0713)

4.2 FTIR spectra analysis

FTIR spectrum of brushite shown in Figure 4.2, Table 4.1 contained bands centred at 3547 and 3467cm^{-1}, which were assigned to the stretching of OH. Furthermore, the bending band of OH was located at 1648 cm^{-1}. All characteristic phosphate bands of brushite were found at 1208, 1132, 1064, 981, 870, 658, 582 and 526 cm^{-1}.The bands at 1208–988 and 788–526 cm^{-1} corresponded, respectively, to ν3 and ν4 vibration modes of phosphate groups. Weak band at 981 and 870 cm^{-1} were assigned to the P-OH stretching mode of HPO_4^- group.

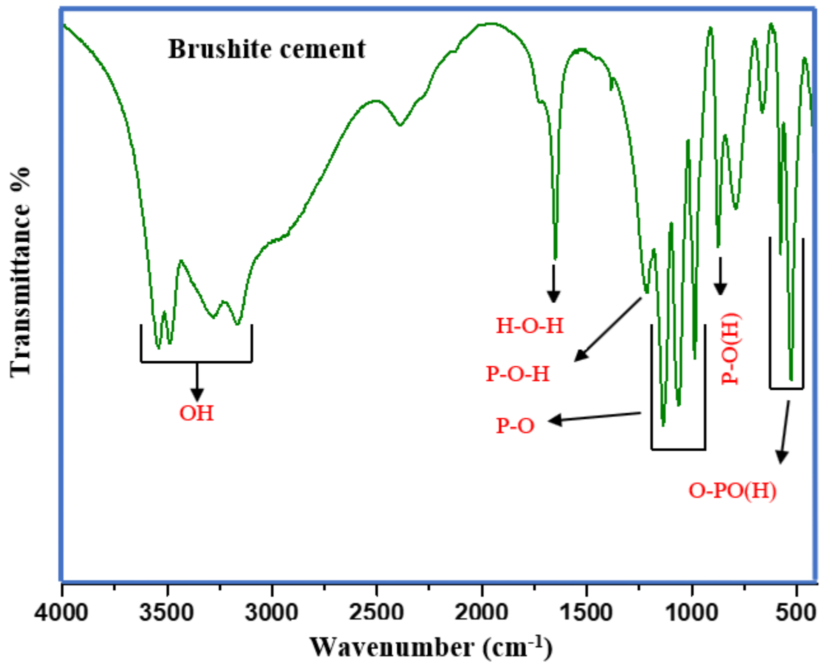

Figure 4.2: FT-IR spectra of brushite cement

Table 4.1: FTIR bands for brushite cement

Absorptions	**Vibration of brushite (FTIR modes)**
3557-3468	O-H stretching of lattice
3269-3148	water molecules
2936	(P)O-H stretching
2392	Combination H-O-H
	bending and residual free
1620-1720(broad)	H-O-H bending of lattice
1653	water molecules
1207	P-O-H in-plane bending
1135	P-O stretching
1065	
984	P-O stretching
871	P-O(OH) stretching
784	P-O(OH) out-of-plane
663	bending
569	Water liberations
	O-P-O(H) bending mode

4.3 Morphology

Due to the fact that brushite's chemical reactivity is highly dependent on its surface properties, regulating its crystal morphology is crucial for its use as a precursor to other bioceramics or as a functional material. The formation mechanism of nested structures is predicated not only on a reduction in concentration during crystallization, but also on the early aggregation of crystal nuclei. Controlling the early crystallization process, specifically the rate of nucleation, is thus the most significant determinant in determining the morphology of the brushite crystals. Pure brushite FESEM images revealed the formation of small, irregularly shaped, structured particles. (Figure 4.3).

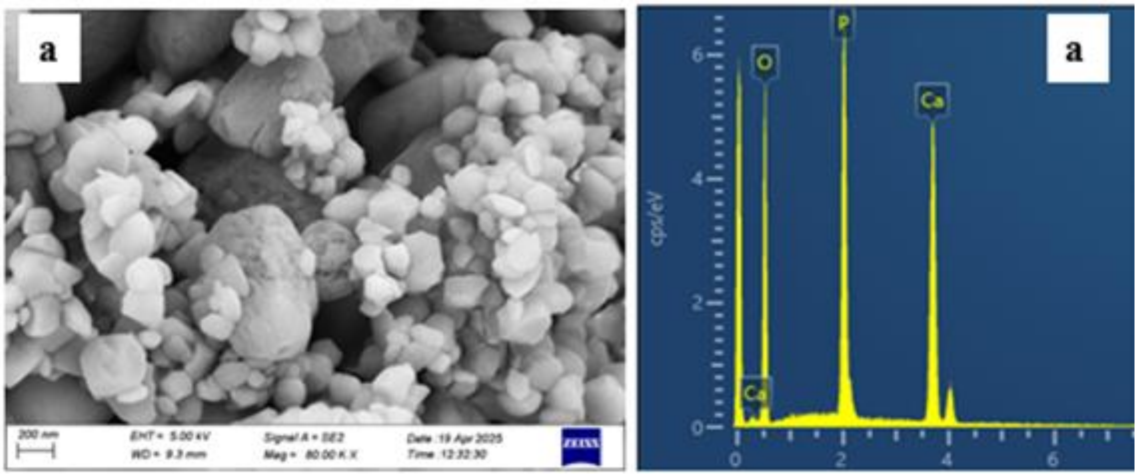

Figure 4.3. FESEM images and EDX of brushite cement

4.4 Cobalt Substituted Dicalcium Phosphate Cement

4.4.1 X-ray diffraction analysis (XRD)

The x-ray diffraction patterns of the bruhite (Brc), Co-Brc (Figure. 4.4) confirmed that the cement matrix became predominantly composed of crystalline brushite (ICDD 72-0713). XRD pattern confirmed the formation of monoclinic crystalline section with decrease in lattice parameters upon Co^{2+} doping (Table 4.2). The plane (12-1) of Co-Brc shifted to the lower angle by 0.05°, when compared to the pure brushite. The degree of shifting in peaks increased with increase in the Co^{2+}

concentration in the brushite samples, the shifting in the peak indicated the incorporation of Co^{2+} into the brushite lattice in place of Ca^{2+} ion or presence of the Co^{2+} in the lattice as an interstitial ion. No characteristic peaks of other calcium phosphate phases and impurities were detected in all Co doped brushite cements.

Table 4.2: Lattice parameters of brushite and Co-substituted brushite cements.

Samples ID	**Lattice parameters**			
	a(Å)	*b*(Å)	*c*(Å)	Cell Volume (Å)^3
Brc	5.808	15.126	6.234	490.4653
1Co-Brc	5.802	15.158	6.442	491.3927
2Co-Brc	5.806	15.138	6.236	490.3782
3Co-Brc	5.854	15.850	6.058	319.3183
4Co-Brc	5.521	15.868	6.481	312.3109

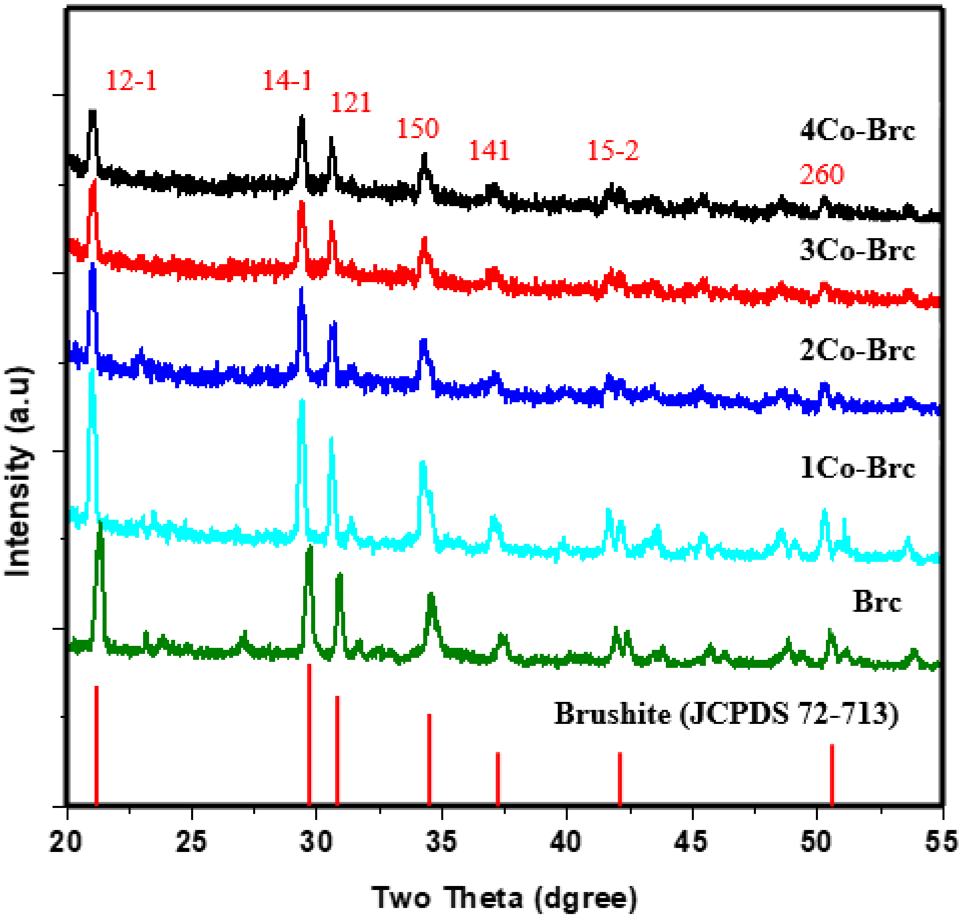

Figure 4.4 XRD patterns of the Brc and set Co-Brc cements.

4.4.2 FTIR spectra analysis

FTIR of Co and Co-Brc shown in (Figure 4.5). FTIR spectra of the Co doped Co-Brc contained bands at 3540 cm^{-1}, 3485 cm^{-1}, 3290 cm^{-1} and 3155 cm^{-1}, which were assigned to the O–H stretching of water. PO stretching was located at 1139 cm^{-1}, 1057 cm^{-1}, and 988 cm^{-1}. The P–O(H) stretching is observed at 864 cm^{-1}, PO bending is recorded at 664 cm^{-1}, 575 cm^{-1} and 520 cm^{-1}. The intensity of vibrational bands reduced upon incorporation of Co^{2+} ions substantially suggesting a distortion of the shape, hence confirming the formation of Co-DCP samples with reduced diploma of crystallinity, a fashion that's according with the XRD data altering the specific geometric linkage of the Ca–P related bonds due to the presence of Co^{2+}.

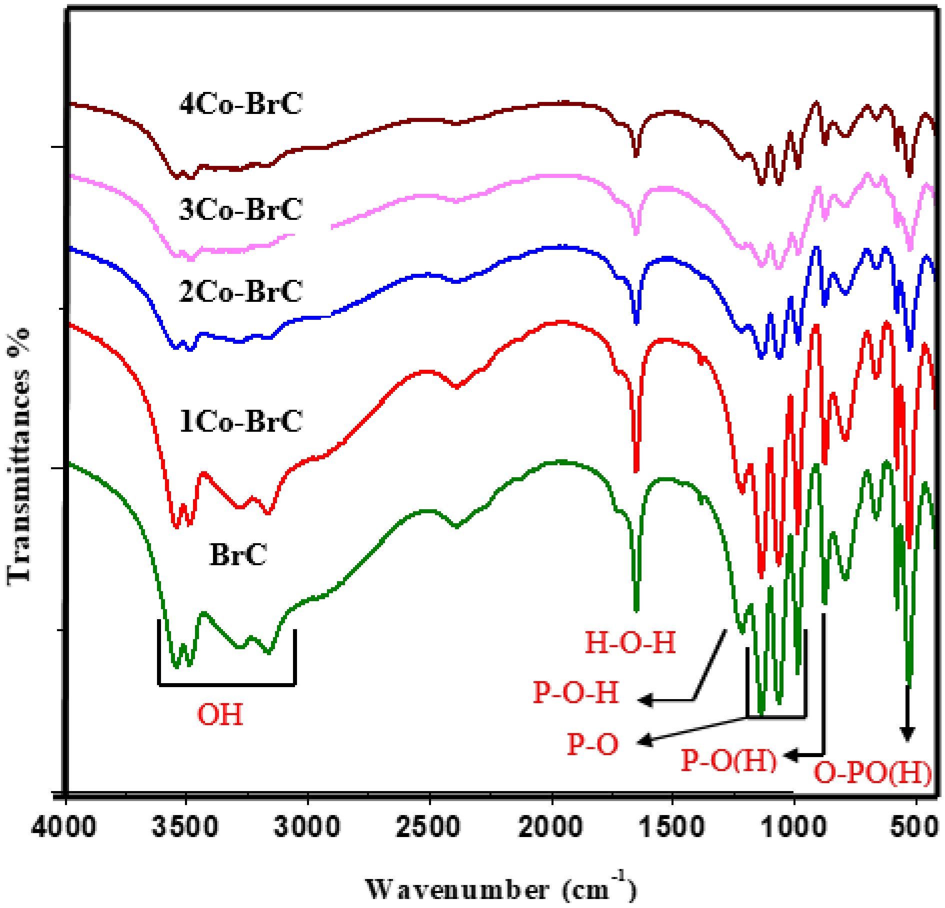

Figure 4.5 FTIR spectra of Brc and Co doped brushite

4.4.3 Morphology

The FESEM pictures of Co doped DCP cements are provided in determine four.6. FESEM of natural brushite confirmed the formation of small based particles of abnormal morphology (Figure 4.6a), which modified to loosely packed plate like morphology with heterogeneous size distribution upon Co^{2+} doping (parent 4.6b-e). The plates show a specific orientation, suggesting a greater or less isotropic conduct.

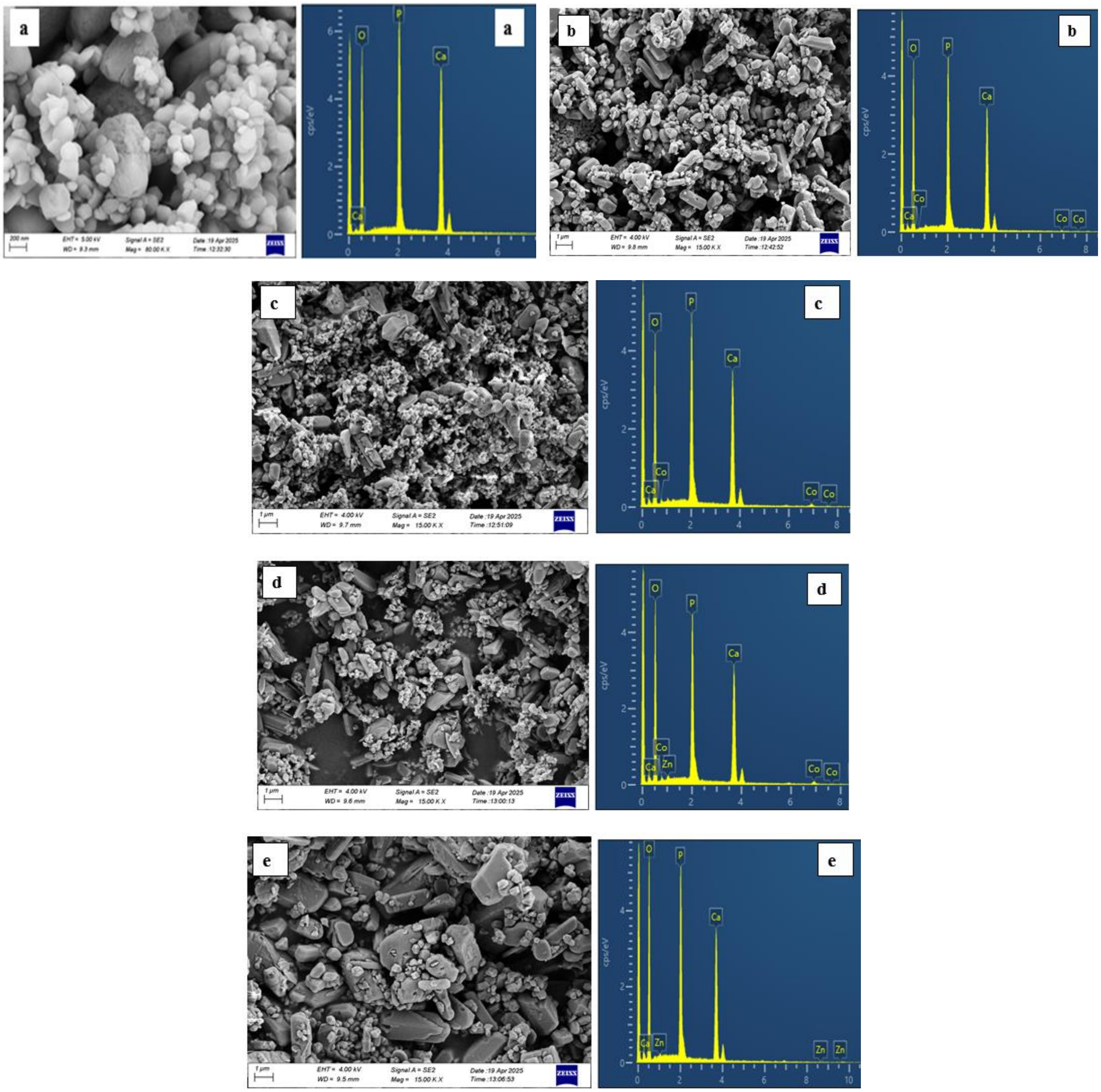

Figure 4.6: FESEM images and EDX of (a)Brc, (b)1Co-Brc, (c)2Co-Brc, (d)3Co-Brc and (e) 4Co-Brc.

4.5 In vitro study

4. 5.1 Setting time and injectability

Brushite cements are of clinical hobby because of their most effective dissolution underneath physiological conditions. Presently, proscribing factors for Their tremendous clinical software are quick placing times, low mechanical properties and a loss of sufficient fluidity to enable injection through hypodermic needles. Figure 4.7 indicates the outcomes of setting times of the cements measured by way of the usage of the gilmore needle. The initial and very last placing times of the herbal brushite cement organized at 0.8 ml/g liquid-to-powder ratios had been 5 min and 9 min respectively. Short placing times measured for natural brushite cement makes it wrong for clinical programs. But, the doping of Co ions into the brushite cement ended in large boom in the setting, wherein very last putting times of 15 minutes became placed for 1Co-Brc. In elegant, the final placing instances of brushite cements stepped forward with the growth inside the Co content material inside the cement, final setting times of 20, 25 and 32 min have been placed for 2Co-brc, 3Co-Brc and 4Co-Brc respectively.

Cement injectability could be very critical for minimally invasive surgical procedures that require injection of the cement into bone defects. Injectable, brushite cements have excellent potential as bone replacement substances because of more appropriate degradability and lengthy-time period inclusion in bone remodeling. But, the usage of brushite cement in minimally invasive surgical strategies is constrained by using their low injectability and mechanical power. One of the main demanding situations for injectable cements is to better control their injectability and keep away from the famous phenomenon of ‘‘clear out-urgent”, or the separation of powder debris and liquid within the syringe, which drastically limits their implantation using an injection method. The injection of paste is supposed to take location right now after blending of the liquid and the powder stages of the cement (Figure 4.7a). The effect of cobalt doping on the injectability brushite cement is illustrated in (Figure 4.7 b). Natural Brc confirmed an injectability of 11.50 %, making it incorrect for minimal invasive surgeries. The horrible injectability of the natural brushite cement end up attributed to its brief putting time of five minutes. The injectability of the paste multiplied to 80.5 % even as cobalt turned into included into the brushite cement (Figure.5.7b). In well known, the injectability of the cements extended with boom inside the co-content material, which was attributed to the concomitant lower of the viscosity of the pastes.

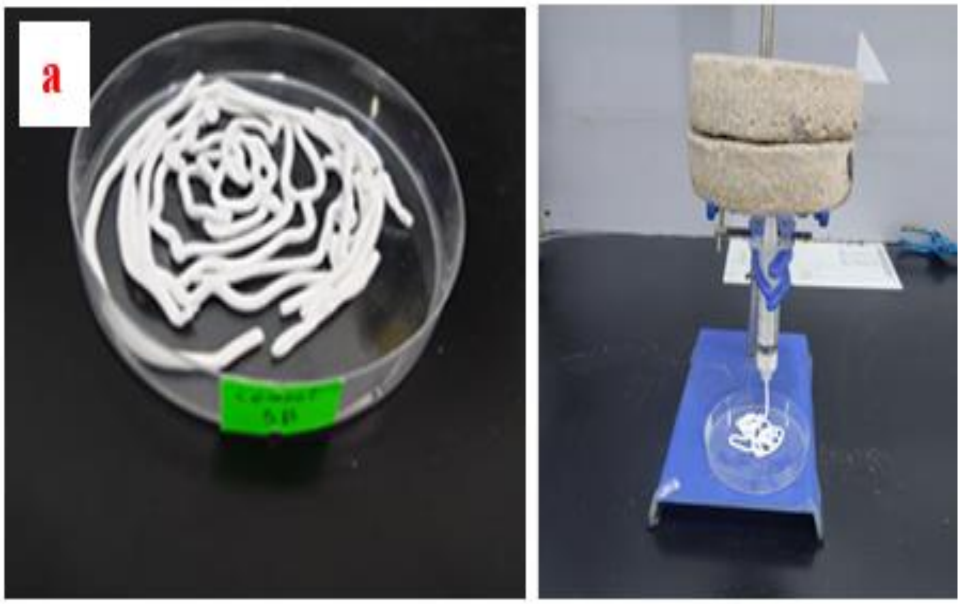

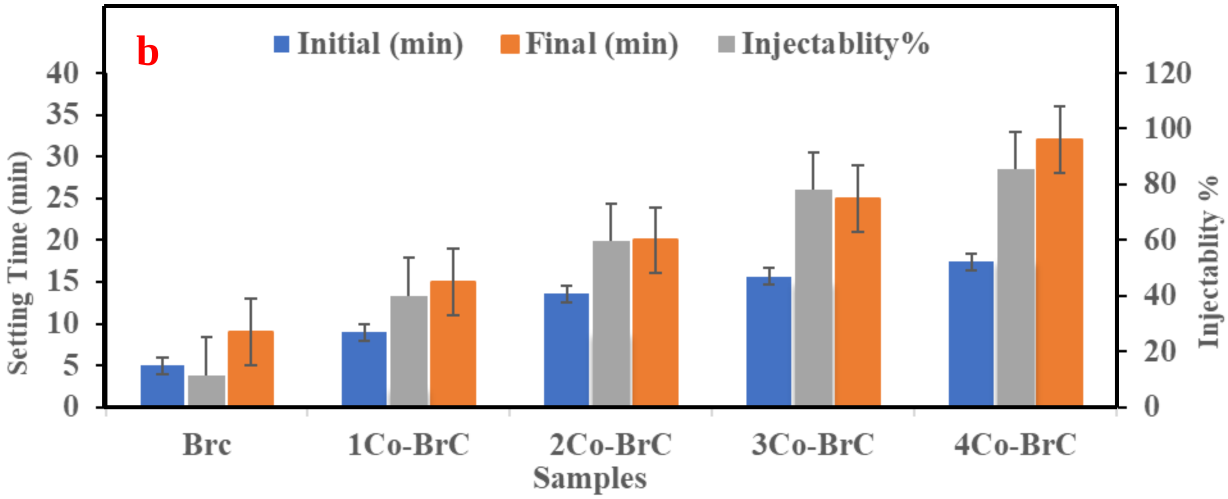

Figure 4.7: photograph of the paste after extrusion from the syringe (a), Setting time and injectability of brushite cement and cobalt substituted (b).

4.5.2 Compressive strength

In medical applications, bone replacement substances are required to provide good enough brief- and lengthy-time period mechanical help for the defect website, which is crucial for the bone healing manner. Brushite cements are generally weaker than the general public of apatite cements [120], the principal reason for relatively low compressive energy is the extraordinarily rapid putting reaction which ends up in high porosity. Compressive power of natural Brc before soaking in SBF answer was 0.98 MPa, the boom in compressive electricity of the Brc samples became located with addition of Co^{2+} ions into the cement, compressive electricity of 9.87, 13.63, 18.34 and 20.78 MPa had been discovered for 1Co-Brc, 2Co-Brc, 3Co-Brc and 4Co-Brc after 1 day respectively. This growth in compressive electricity became assigned to the decrease in relative porosity of the samples. To similarly examine the in vitro mechanical homes of the fabric, the compressive power of the samples becomes measured after soaking in SBF for 7 days (Figure 4.8, table 4.3). The compressive electricity of the natural brushite cement improved from 1.323 MPa to 8.59 MPa after being soaked in the SBF for 1 day, this increase within the compressive strength becomes due to the slow reduction in relative porosity. The compressive strength of the Brc sample elevated similarly to 23.87after 7 days of soaking in SBF. In standard, the compressive electricity of the Co-Brc elevated with the growth in Co content in sample and boom in soaking time in SBF. Highest compressive power of 25.34 MPa become discovered for 4Co-Brc after 3 days of soaking in SBF.

Table 4.3: Compressive strength (MPa) of Brc and Co-Brc before and after immersion in SBF.

Samples ID	**0d**	**1d**	**3d**	**7d**
Brc	0.89	5.8	10.76	15.45
1Co-Brc	7.88	9.87	16.92	13.47
2Co-Brc	10.78	13.63	18.83	18.28
3Co-Brc	13.45	18.34	22.45	16.76
4Co-Brc	16.93	20.78	25.34	23.87

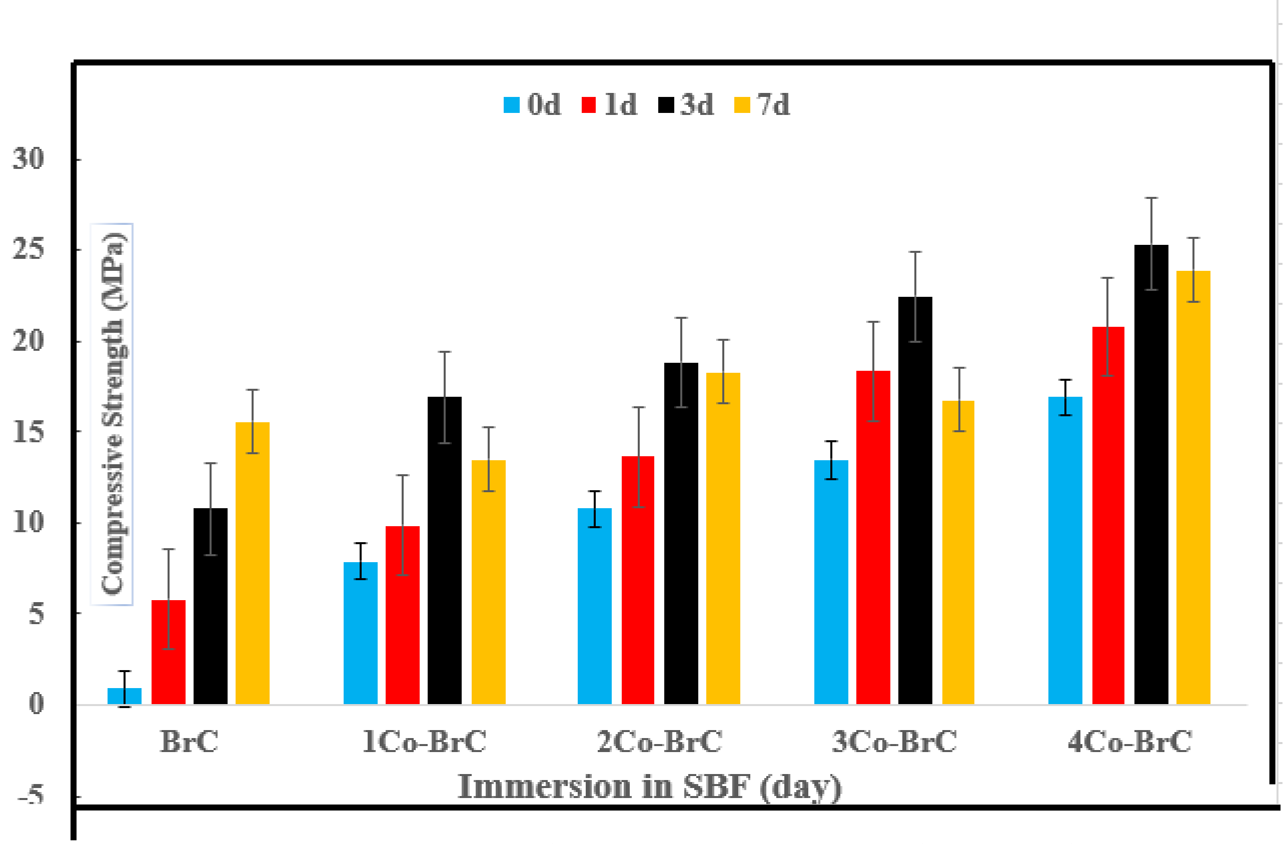

Figure 4.8: Compressive strength of brushite and Co-Brc before and after immersion in SBF

4.5.3 Ion release from Co-substituted brushite cements

Table 4.4 suggests the release of Ca^{2+} ions and Co^{2+} ions in SBF over 7 days, it was mentioned that the Ca^{2+} ion and Co^{2+} concentration in SBF started to increase right away, indicating the initiation of the ground degree dissolution of the samples. After 3days of immersion the eye of Ca^{2+} ion started to decline due to the consumption of Ca^{2+} ions within the formation of the apatite layer, indicating that the deposition manner will become the dominant process after the first three days of the immersion in SBF. The awareness of Ca^{2+} was fairly strong among 3 to7 days ultimately indicating that the equilibrium between the deposition and dissolution has been attained, whilst the attention of Co^{2+} ions started out to mention no after three days, which modified into in all likelihood due to their consumptions in the formation of the apatite layer [121]. Launch of Co^{2+} ion from Co-Brc samples over 7 days is proven in desk 4.4, the maximum release of 72.54 mg/L was observed for 4Co-Brc in 7 days. In general, the dissolution of Brc in SBF is connected with ionic substitution. Ionic substitution in Brc results in the reduction in the degree of crystallinity, resulting in the faster dissolution of Brc or vice versa. In this study, Co-Brc exhibited higher dissolution compared to standard Brc Which was attributed to the alternate within the lattice parameters and decrease degree of crystallinity of Co-Brc samples.

Table 4.4: Release of Ca^{2+} and Co^{2+} ions in SBF over 7 days at 37°C

Immersion time (days)	**Release of Ca^{2+} ion (mg/L) and Co^{2+} ion (mg/L) in SBF**								
	BrC	**1Co-BrC**		**2Co-BrC**		**3Co-BrC**		**4Co-BrC**	
	Ca^{2+}	**Ca^{2+}**	**Co^{2+}**	**Ca^{2+}**	**Co^{2+}**	**Ca^{2+}**	**Co^{2+}**	**Ca^{2+}**	**Co^{2+}**
1	3.658	4.750	46.9	4.254	50.5	4.786	55.29	4.854	49.98
3	3.624	3.485	50.3	4.155	58.32	4.634	42.12	3.799	60.57
7	3.662	3.517	47.8	4.873	49.35	4.967	53.66	5.876	72.54

4.5.4 *In vitro* controlled drug release

4.5.4.1 *In vitro* drug release profiles of antibiotics from Co-Brushite cement

The cumulative release of amoxicillin and ampicillin trihydrate from 2Co-Brc is shown in (Figure 4.9).

On this observe the discharge profile is seen to be bimodal, wherein burst release become observed in first 12 h observed with the resource of a managed continuous launch. After a fast release of 80% all through the primary 12 h, the release charge reduced ampicillin trihydrate have become determined after 7 days. Whereas 67% burst launch of amoxicillin have become found in first 12 h observed via using sustained launch over 7 days to gain 77 % launch of the loaded drug. The 2Co-Brc containing ampicillin trihydrate launched 55% of the loaded drug after 12 h of immersion, while general of 80% loaded drug turned into released after 7 days. The initial burst launch became attributed to the release of drug adsorbed at the outer surface of the samples, while the sluggish sustained launch of the drug come to be ascribed to the discharge of drug from inside the cement network. The burst launch inside the preliminary segment accompanied by using a slow release over 7 days is taken into consideration favorable to prevent bacterial contamination after the surgical procedure. Three possible reasons are suggested for its slow release from cement (i) interaction of organic acid molecules with calcium ions which leads to the formation of antibiotic–calcium phosphate complex (ii) poor water solubility of antibiotic (iii) The change in the nature of loaded matrix, i.e. conversion of the cement reactants into apatite phase. It may result in trapping antibiotic molecules within the apatite crystals [122].

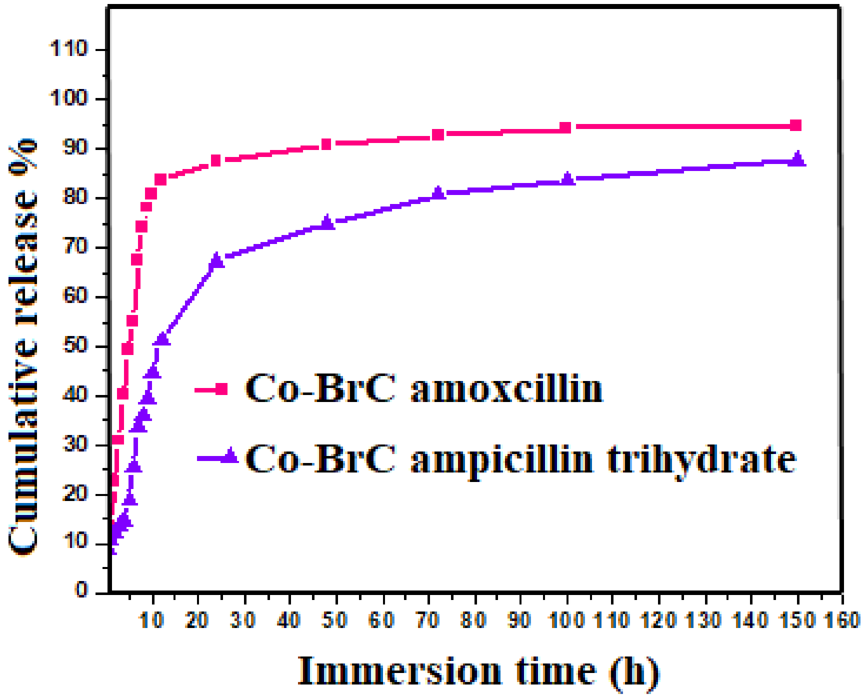

Figugre 4.9 In vitro release profile of antibiotics from 2Co-Brc in SBF versus immersion time.

4.6 Zinc Substituted Dicalcium Phosphate Cement

Zinc-substituted HA as-prepared powder was mixed at a 1:0.5 gm weight ratio with MCPM; 0.8 ml (0.5M of trisodium citrate) was added to the mixture to form a homogeneous paste.

4.6.1 X-ray diffraction analysis (XRD)

Phase evaluation of the brushite and Zn-brushite changed into determined with the aid of using XRD. The XRD sample of pure brushite became in correct settlement with the crystalline brushite (ICDD 72-0713)[122]. The incorporation of Zn in the lattice additionally prompted the shifting of XRD peaks (Figure 4.10). The aircraft (12-1) of 1Zn-Brc shifted to the lower attitude by 0.05°, whereas the same aircraft in 2Zn-brc shifted to the lower attitude by way of 0.21° while compared to the pure brushite. The degree of moving in peaks elevated with growth within the Zn awareness inside the brushite samples, the transferring within the top indicated the incorporation of mg into the brushite lattice in place of Ca^{2+} ion or presence of the Zn inside the lattice as an interstitial ion. No characteristic peaks of other calcium phosphate phases and impurities were detected in all Zn doped brushite cements.

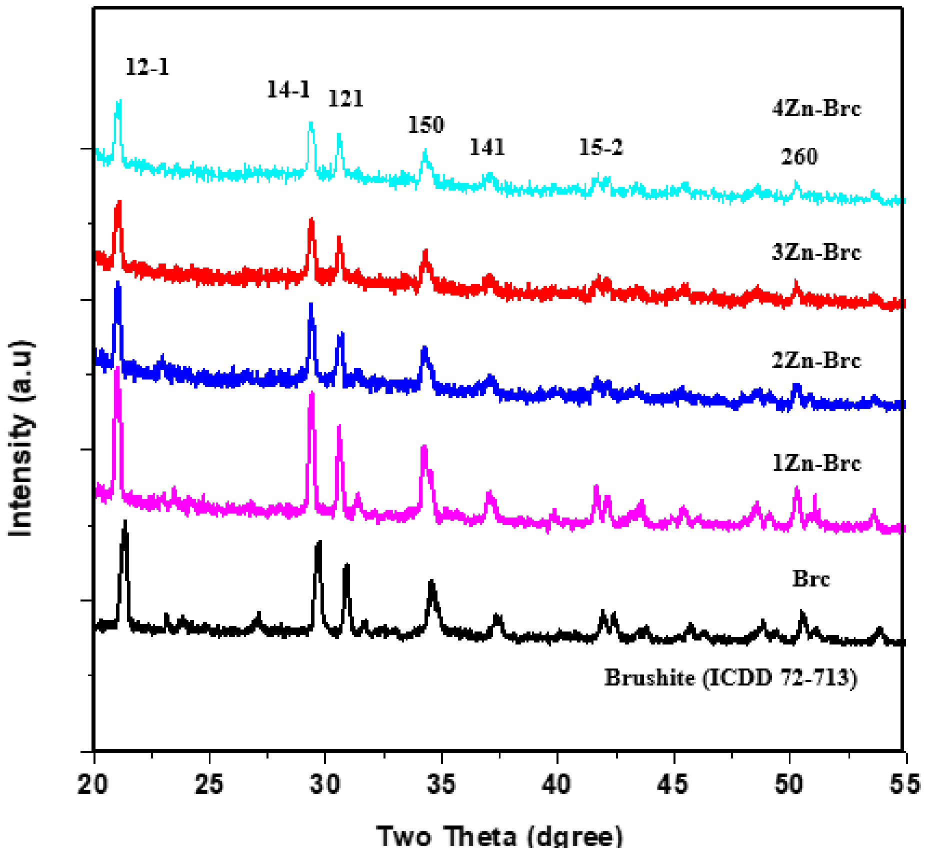

Figure 4.10 XRD patterns of the Brc and set Zn-Brc cements.

4.6.2 FTIR spectra analysis

FTIR of Zn and Zn -Brc shown in (figure 4.11). FTIR spectra of the Zn doped Zn -Brc contained bands at 3540 cm^{-1}, 3485 cm^{-1}, 3290 cm^{-1} and 3155 cm^{-1}, which have been assigned to the O–H stretching of water. PO stretching become located at 1139 cm^{-1}, 1057 cm^{-1}, and 988 cm^{-1}. The P–O(H) stretching is located at 864 cm^{-1}, PO bending is recorded at 664 cm^{-1}, 575 cm^{-1} and 520 cm^{-1}. The intensity of vibrational bands decreased upon incorporation of Zn^{2+} ions considerably suggesting a distortion of the structure, hence confirming the formation of Zn -DCP Samples with decreased degree of crystallinity, a fashion that's in accordance with the XRD information changing the specific geometric linkage of the Ca–P related bonds because of the presence of Zn^{2+}.

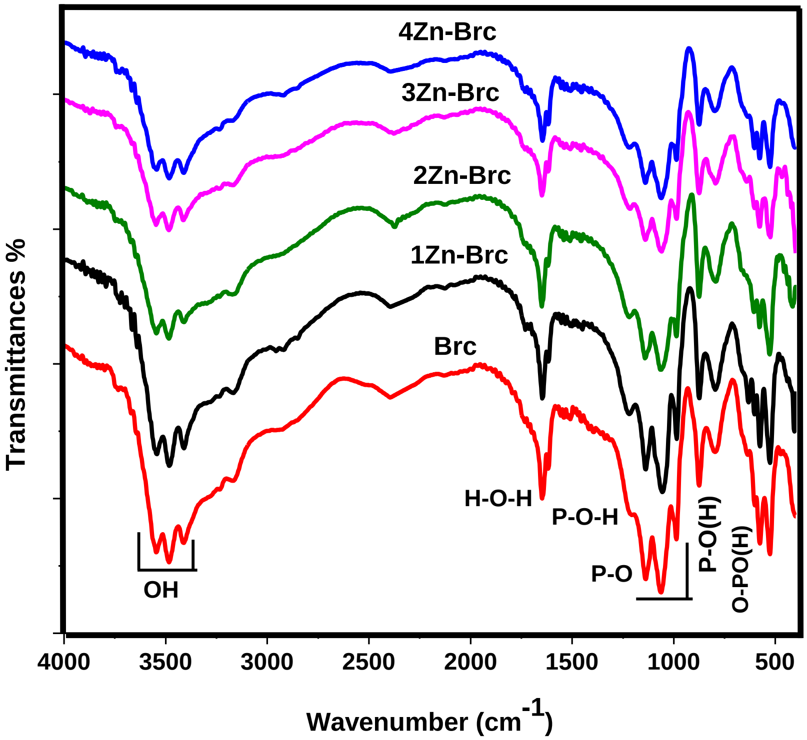

Figure 4.11: FTIR spectra of Brc and Zn doped brushite

4.6.3 Morphological Analysis

FESEM analysis of pure and zinc substituted brushite cements are proven in (figure 4.12). FESEM pics of brushite showed the formation of structured debris of irregular morphology (figure 4.12a). The incorporation of Zn ions into the brushite network resulted within the formation of larger sized particles (figure.4.12b-e). Closer inspection of the pix showed that the larger sized Zn -Brc particles have been predominantly composed of flakes. Which a characteristic of brushite.

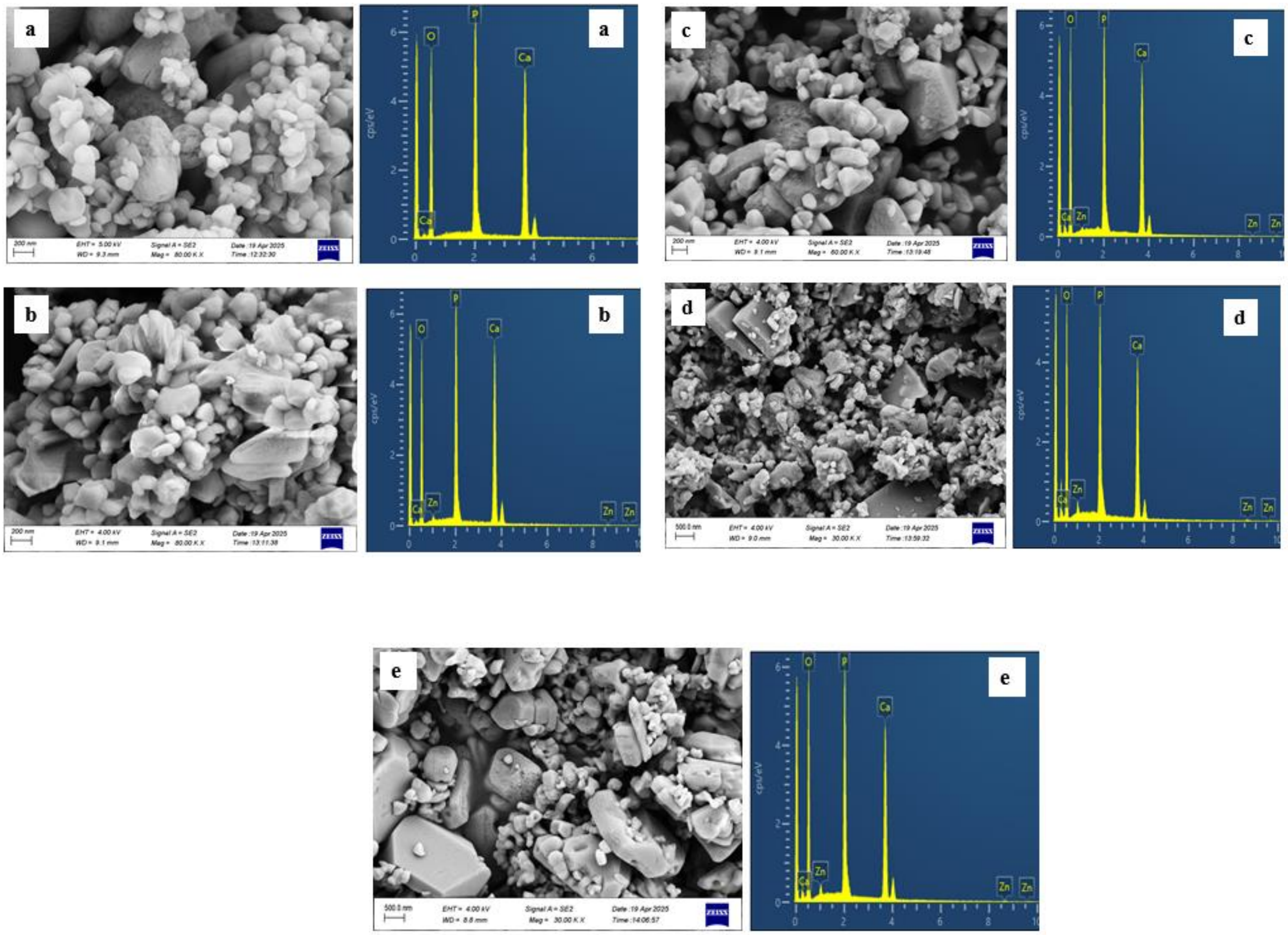

Figure 4.12: FESEM images and EDX of (a)Brc, (b)1Zn-Brc, (c)2Zn-Brc, (d)3Zn-Brc and (e) 4Zn-Brc.

4.6 In vitro study

4. 6.1 Setting time and injectability

Brushite cements are of scientific interest due to their superior dissolution underneath physiological conditions. Presently, proscribing elements for his or her large clinical application are brief putting instances, low mechanical power and a loss of sufficient fluidity to allow injection through hypodermic needles. Determine 4.13 indicates the consequences of placing instances of the cements measured with the resource of the use of the gilmore needle[123]. The initial and very last setting instances of the natural brushite cement prepared at 0.8 ml/g liquid-to-powder ratios had been five min and nine min respectively. Short putting instances measured for herbal brushite cement makes it improper for scientific applications. However, the doping of Zn ions into the brushite cement caused vast increase within the setting, where final putting instances of 12.54 mins became discovered for 1Zn-brc. In fashionable, the final setting times of brushite cements improved with the growth inside the Zn content within the cement, very last setting instances of 18.85, 22.53 and 26.21 min were determined for two Zn-Brc, 3 Zn-Brc and four Zn-Brc respectively.

The injection of paste is supposed to take region proper away after mixing of the liquid and the powder levels of the cement (figure 4.13., table 4.5). The effect of Zn doping on the injectability brushite cement is illustrated in (figure 4.13). Herbal Brc confirmed an injectability of 12.34%, making it wrong for minimum invasive surgical processes. The poor injectability of the natural brushite cement have become attributed to its short setting time of 9 mins. The injectability of the paste improved to 84.14 % at the same time as Zn changed into covered into the brushite cement. In standard, the injectability of the cements increased with growth inside the Zn-content material, which become attributed to the concomitant decrease of the viscosity of the pastes.

Table 4.5. Setting time and injectability of Brc and Zn-Brc

	Brc	1Zn-BrC	2Zn-BrC	3Zn-BrC	4Zn-BrC
Initial (min)	2	7.23	10.32	14.56	16.87
Final (min)	4.66	12.54	18.85	22.53	26.21
Injectability%	12.34	44.47	62.24	80.62	84.14

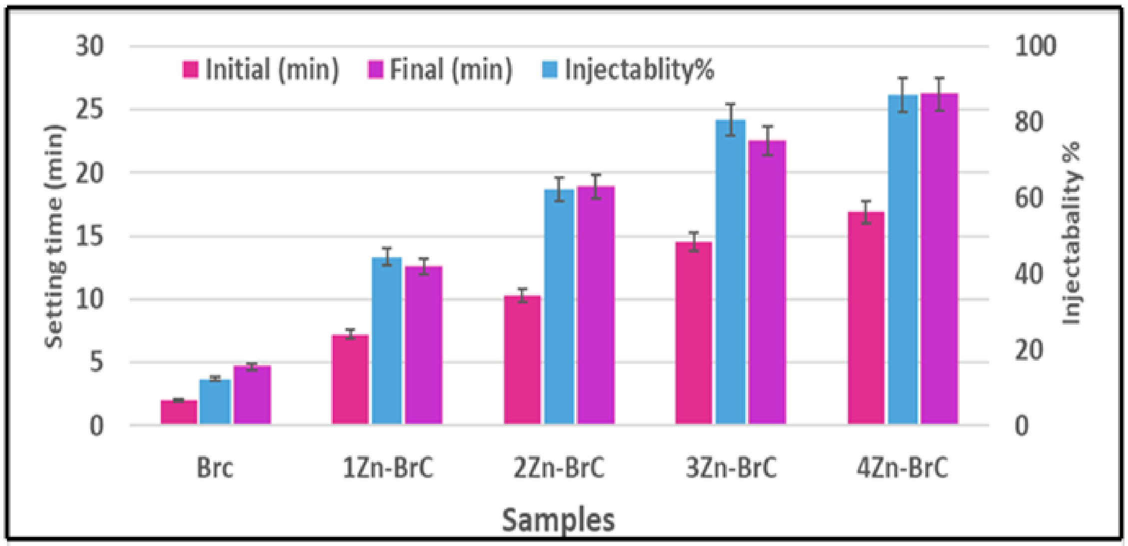

Figure 4.13: Setting time and injectability of brushite cement and zinc substituted.

4.6.2 Compressive strength

Brushite cements are usually weaker than the general public of apatite cements [124], the primary cause for fantastically low compressive strength is the relatively fast setting response which ends up in excessive porosity. The compressive electricity of Brc and Zn-Brc cements earlier than and after soaking in SBF. Compressive energy of pure Brc earlier than soaking in SBF answer become 0.82 MPa, the growth in compressive electricity of the Brc samples became located with addition of Zn^{2+} ions into the cement, compressive strength of 17.25, 19.21, 20.76 and 27.83 MPa have been observed for 1Zn-Brc, 2Zn-Brc, 3Zn-Brc and 4Zn-Brc after soaked in SBF for 3 days respectively. This growth in compressive energy becomes assigned to the decrease in relative porosity of the samples. To further take a look at the in vitro mechanical properties of the fabric, the compressive electricity of the samples changed into measured after soaking in SBF for 7 days (figure 4.14, table 4.6). This boom within the compressive electricity changed into due to the sluggish discount in relative porosity. In stylish, the compressive electricity of the Zn-Brc increased with the growth in Zn content cloth in sample and growth in soaking time in SBF.

Table 4.6: Compressive strength of brushite and Zn-Brc before and after immersion in SBF

	BrC	1Zn-BrC	2Zn-BrC	3Zn-BrC	4Zn-BrC	AVERAGE	STDEV
0d	0.82	6.88	10.78	14.66	16.11	8.285	6.195773
1d	6.2	10.23	12.88	17.98	20.45	11.8225	5.760397
3d	9.26	17.25	19.21	20.76	27.83	16.62	6.688525
7d	13.65	14.57	15.34	15.73	23.54	14.8225	3.978873

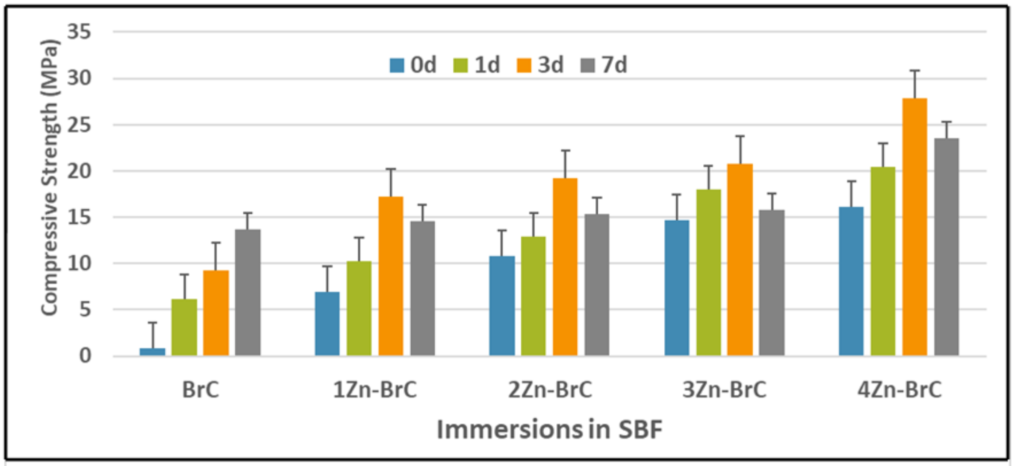

Figure 4.14: Compressive strength of brushite and Zn-Brc before and after immersion in SBF

4.6.3 Ion release from Zn-substituted brushite cements

Table 4.7 shows the discharge of Ca^{2+} ions in SBF over 7 days, it became stated that the Ca^{2+} ion concentration in SBF began to boom straight away, indicating the initiation of the surface diploma dissolution of the samples. After 3days of immersion the eye of Ca^{2+} ion started out to say no due to the consumption of Ca^{2+} ions inside the formation of the apatite layer, indicating that the deposition machine becomes the dominant procedure after the first three days of the immersion in SBF. The eye of Ca^{2+} grow to be quite solid among three to7 days therefore indicating that the equilibrium the various deposition and dissolution has been attained, while the attention of Zn^{2+} ions commenced to mention no after three days, which have become likely because of their consumptions in the formation of the apatite layer. Release of Zn^{2+} ion from Zn-Brc samples over 7 days is shown in table 4.7, the maximum release of 72.54 mg/L was observed for 4Zn-Brc in 7 days. In general, the dissolution of Brc in SBF is connected with ionic substitution. Ionic substitution in Brc results in the reduction in the degree of crystallinity, resulting in the faster dissolution of Brc or vice versa [125]. In this study, Zn-Brc exhibited higher dissolution compared to standard Brc which was attributed to the change in the lattice parameters and lower degree of crystallinity of Zn-Brc samples.

Table 4.7: Release of Ca^{2+} and Zn^{2+} ions in SBF over 7 days at 37°C

Immersion time (days)	**Release of Ca^{2+} ion (mg/L) and Co^{2+} ion (mg/L) in SBF**								
	BrC	**1Zn-BrC**		**2Zn-BrC**		**3Zn-BrC**		**4Zn-BrC**	
	Ca^{2+}	**Ca^{2+}**	**Zn^{2+}**	**Ca^{2+}**	**Zn^{2+}**	**Ca^{2+}**	**Zn^{2+}**	**Ca^{2+}**	**Zn^{2+}**
1	3.752	4.760	47.22	4.254	50.5	4.786	55.29	4.854	49.98
3	3.633	3.490	51.30	4.155	58.32	4.634	42.12	3.799	60.57
7	3.680	3.520	48.74	4.873	49.35	4.967	53.66	5.876	72.54

4.7 Silver Substituted Dicalcium Phosphate Cement

Silver-substituted HA as-prepared powder was mixed at a 1:0.5 gm weight ratio with MCPM; 0.8 ml (0.5M of trisodium citrate) was added to the mixture to form a homogeneous paste.

4.7.1 X-ray diffraction analysis (XRD)

The X-ray diffraction patterns of the Brc, Ag-Brc (Figure. 4.15) showed that the cement matrix was predominantly composed of crystalline brushite (ICDD 72-0713). The increased incorporation of Ag^{+} ion into the DCP induced the shifting of peaks toward lower diffraction angle, increase in the lattice parameters and decrease in cell volume, this change in parameters could be attributed to the larger ionic radius of Ag^{+} (1.28 Å) compared to the Ca^{2+} (0.99 Å) which it has replaced [126].

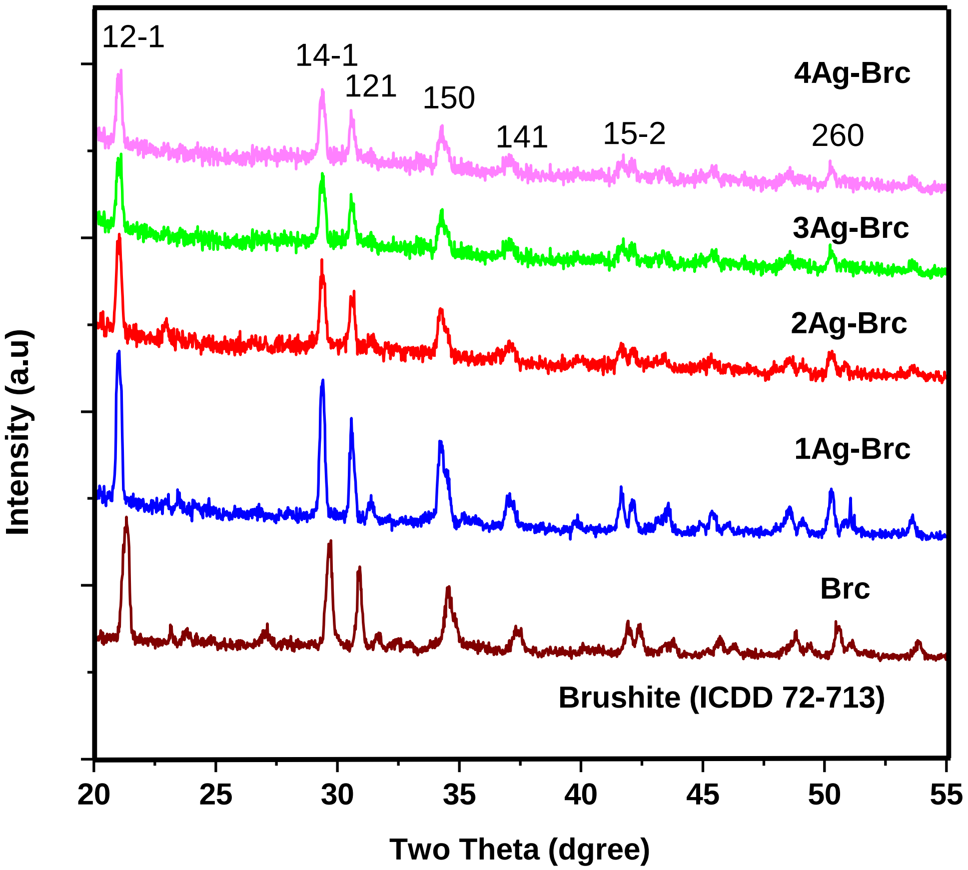

Figure 4.15: XRD patterns of the Brc and set Ag-Brc cements.

4.7.2 FTIR spectra analysis

FTIR of Ag and Ag-Brc shown in (figure 4.16). FTIR spectra of the ag doped Ag-Brc contained bands at 3540 cm^{-1}, 3485 cm^{-1}, 3290 cm^{-1} and 3155 cm^{-1}, which had been assigned to the O–H stretching of water. PO stretching turned into located at 1139 cm^{-1}, 1057 cm^{-1}, and 988 cm^{-1}. The P–O(H) stretching is observed at 864 cm^{-1}, po bending is recorded at 664 cm^{-1}, 575 cm^{-1} and 520 cm^{-1}. The depth of vibrational bands reduced upon incorporation of Ag^{+} ions considerably suggesting a distortion of the structure, hence confirming the formation of Ag -DCP Samples with reduced degree of crystallinity, a fashion that is in accordance with the XRD data changing the specific geometric linkage of the Ca–P related bonds because of the presence of Ag^+ [127].

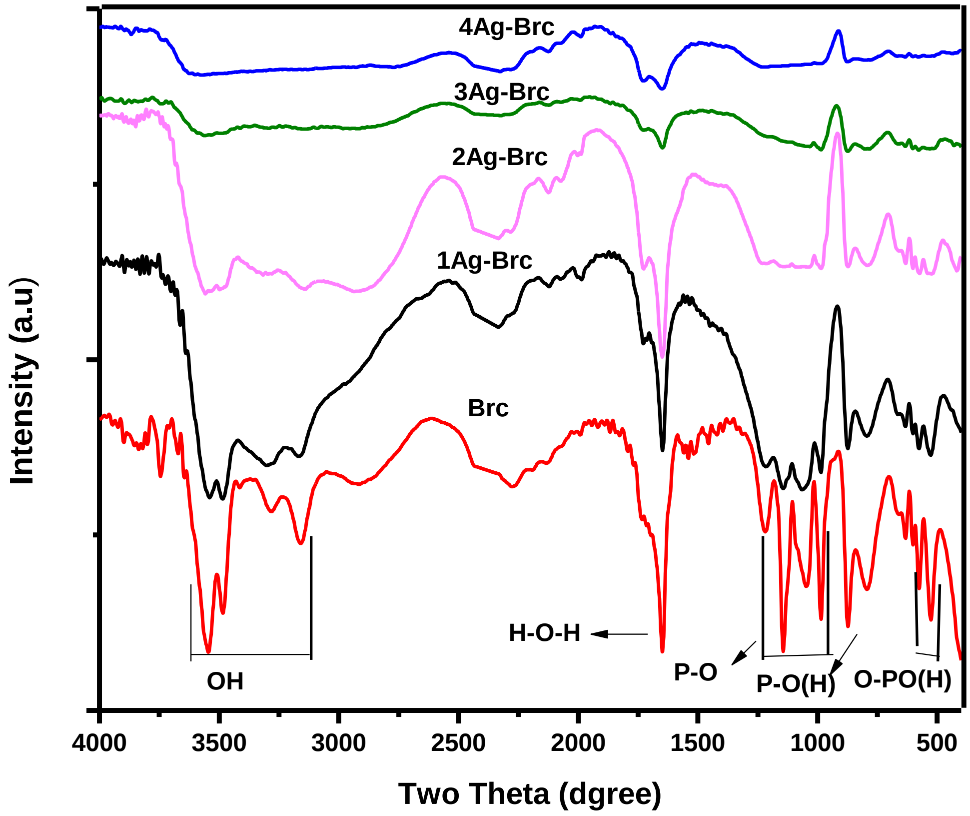

Figure 4.16: FTIR spectra of Brc and Ag doped brushite

4.7.3 Morphological Analysis

Due to the fact that brushite's chemical reactivity is highly dependent on its surface properties, regulating its crystal morphology is crucial for its use as a precursor to other bioceramics or as a functional material. The formation mechanism of nested structures is predicated not only on a reduction in concentration during crystallization, but also on the early aggregation of crystal nuclei. Controlling the early crystallizations process, specifically the rate of nucleation, is thus the most significant determinant in determining the morphology of the brushite crystals. Pure brushite FESEM images revealed the formation of small, irregularly shaped, structured particles. (Figure 4.17).

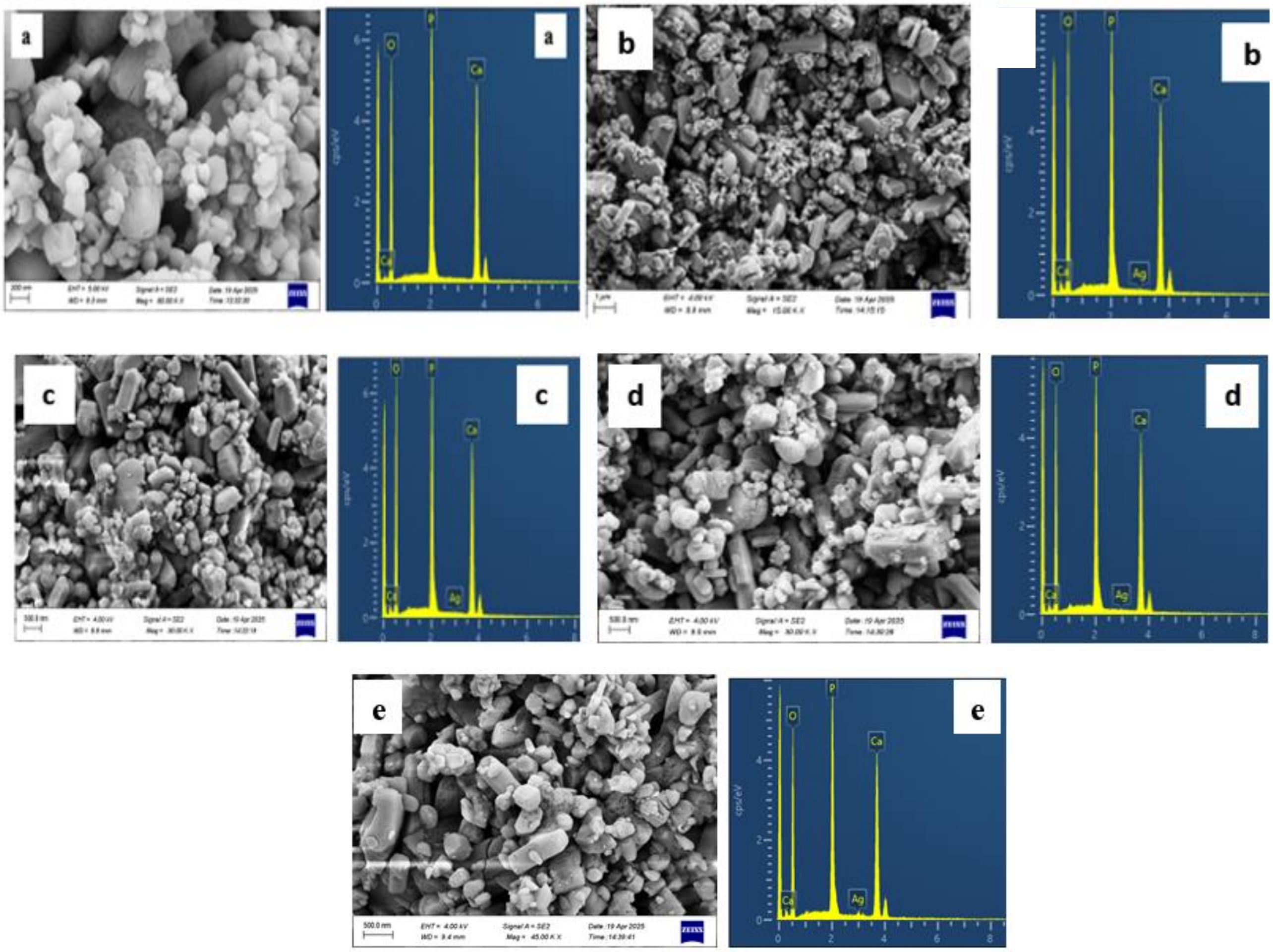

Figure 4.17: FESEM images and EDX of (a)Brc, (b)1Ag-Brc, (c)2g-Brc, (d)3Ag-Brc and (e) 4Ag-Brc.

4.8 In vitro study

4. 8.1 Setting time and injectability

The clinical utility of brushite cements stems from their favorable solubility under physiological conditions. An objective of this study was to ascertain whether the setting reaction has any effect on the injectability of DCPD. Figure 4.18, Table 4.8 illustrates the initial and ultimate configuration periods for DCPD at ambient temperature (25 ◦C). At present, their expansive clinical application is constrained by several factors: prolonged setting periods, inadequate mechanical strength, and insufficient fluidity to facilitate administration via hypodermic needles. The results of the cements' curing periods, as determined by the Gilmore needle, are illustrated in Figure 4.18. The pure brushite cement liquid-to-powder ratio exhibited initial and final curing durations of 4.18 minutes and 6.34 minutes, respectively. Brushite cement's rapid curing periods render it inappropriate for use in clinical settings. Conversely, incorporating varying concentrations of silver ions into the brushite cement led to a significant delay in the setting process, as evidenced by the sample 1Ag-Brc final setting time of 13.82 minutes. Overall, it was observed that the ultimate configuration durations for 2Ag-Brc, 3Ag-Brc, and 4Ag-Brc were 19, 24, and 27 minutes, respectively. The findings suggest that the setting reaction can be influenced by the concentration of silver ions in DCPD, leading to the formation of cement with distinct compositions [128].

The prolonged incorporation of injectable brushite cements into bone remodeling and their enhanced biodegradability make them highly promising as bone replacement materials. While brushite cement can be utilized in minimally invasive procedures, its mechanical strength and injectability are both inadequate. Controlling the injectability of cements and preventing the well-known "filter-pressing" or separation of particulate particles and liquid within the syringe [129], which severely restricts their implantation via injection, is one of the primary challenges of injectable cements. It is recommended that the injection of material occur promptly following the blending of the liquid and granular components of the cement. As shown in (Figure 4.18 table 4.8), the injectability of the material rose from 15.76% to 47.72% (Brc,1Ag-Brc), and then to 67%, 79%, and 86% (2Ag-Brc, 3Ag-Brc, 4Ag-Brc), respectively.

Table 4.8: Setting time and injectability of brushite and Ag-Brc cements

	Brc	1Ag-Brc	2Ag-Brc	3Ag-Brc	4Ag-Brc	AVERAGE	STDEV
Initial (min)	4.18	8.65	12.54	15.43	18.93	11.946	5.754166
Final (min)	6.34	13.82	19.12	24.43	27.35	18.212	8.414646
Injectability%	15.76	47.72	67.63	79.63	86.28	59.404	28.46222

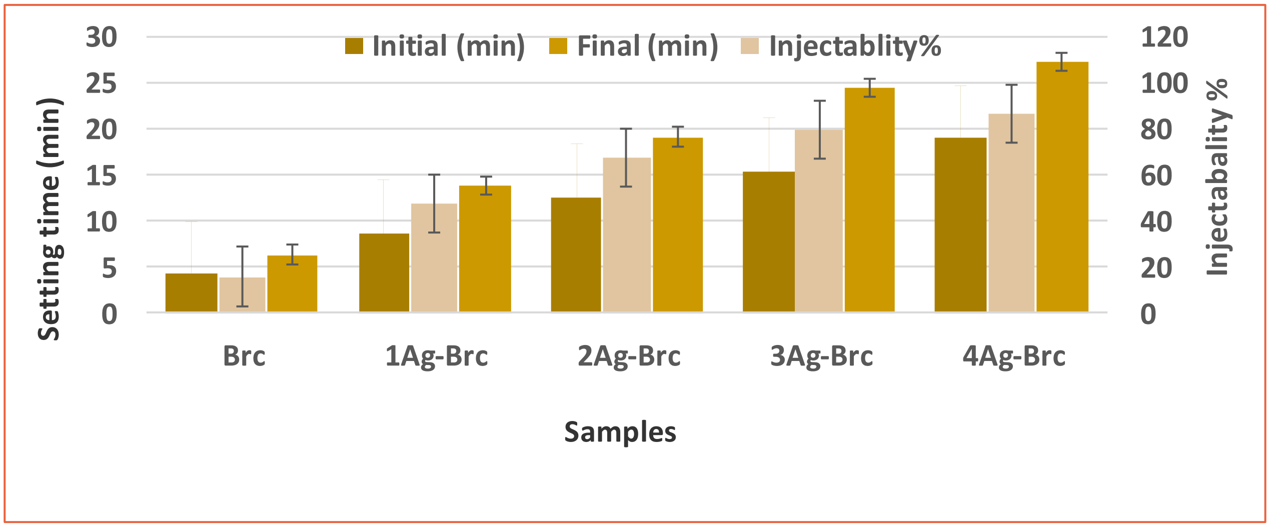

Figure 4.18. Setting time and injectability of brushite and Ag-Brc cements

4.8.2 Compressive strength

Table 4.9 and Figure 4.19 present the compressive strength of brushite cement prior to and subsequent to immersion in SBF for durations of 0, 1, 3, and 7 days. BrC exhibited a compressive strength of 4.87 MPa of Brc prior to immersion in SBF solution 1 day. 1Ag-Brc, 2Ag-Brc, 3Ag-Brc and 4Ag-Brc brushite exhibits an increase in compressive strength from 12.48 to 13.53,14.55 and 18.87 MPa after seven days of immersion in SBF. Overall, the Ag-Brc compressive strength increased to 23.69 MPa after three days of marinating in SBF.

Table 4.9: Compressive strength of brushite before and after immersion in SBF

	BrC	1Ag-Brc	2Ag-Brc	3Ag-Brc	4Ag-Brc	AVERAGE	STDEV
0d	0.74	5.51	8.53	12.63	15.27	8.536	5.138909
1d	4.87	9.94	11.47	16.21	17.76	12.05	4.609785
3d	12.54	15.26	18.82	19.93	23.69	18.048	3.849184
7d	10.52	12.48	13.53	14.55	18.87	13.99	2.780669

	BrC	1Zn-BrC	2Zn-BrC	3Zn-BrC	4Zn-BrC	Average	Stdev
0d	0.82	6.88	10.78	14.66	16.11	8.285	6.195773
1d	6.2	10.23	12.88	17.98	20.45	11.8225	5.760397
3d	9.26	17.25	19.21	20.76	27.83	16.62	6.688525
7d	13.65	14.57	15.34	15.73	23.54	14.8225	3.978873

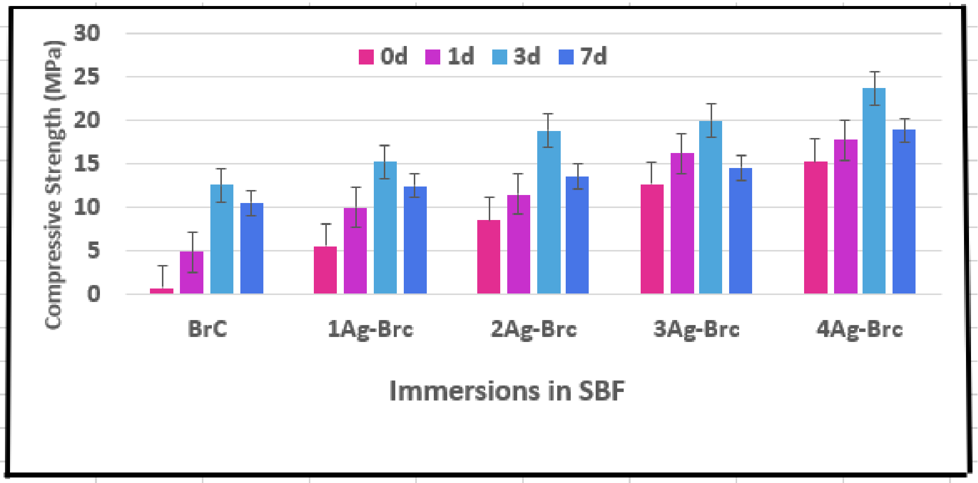

	BrC	1Ag-Brc	2Ag-Brc	3Ag-Brc	4Ag-Brc	Average	Stdev
0d	0.74	5.51	8.53	12.63	15.27	8.536	5.138909
1d	4.87	9.94	11.47	16.21	17.76	12.05	4.609785
3d	12.54	15.26	18.82	19.93	23.69	18.048	3.849184
7d	10.52	12.48	13.53	14.55	18.87	13.99	2.780669

Figure 4.19: Compressive strength of Brc and Ag-Brc before and after immersion in SBF

4.8.3 In vitro antibacterial activity

Biomaterials for clinical programs must residences earlier than scientific trials Balouiri et al, 2016; Gonelimali et al,2018; Sulaiman et al.,2024; Jasim et al.,2020. The antimicrobial activity of the Ag-DCP become assessed via the nicely diffusion assay against human pathogenic strains in clouding yeast, Gram-fine and Gram-bad microorganism. (figure 4.20). The antibacterial activity of the Ag-DCP loaded antibiotic launched changed into assessed against the Escherichia coli (*E.coli, ATCC* 25922 lines) and *Staphylococcus aureus*. The samples had been incubated with E. coli and Staphylococcus aureus suspension for 24 h. determine four.6 well-known shows the significant in antibacterial effect. in this observe we've validated that with a silver concentration it has to be possible to supply a bone replacement material with antibacterial residences that is likely to inhibit capability post-operative bacterial {Lin, 2015 #190}infections [130].

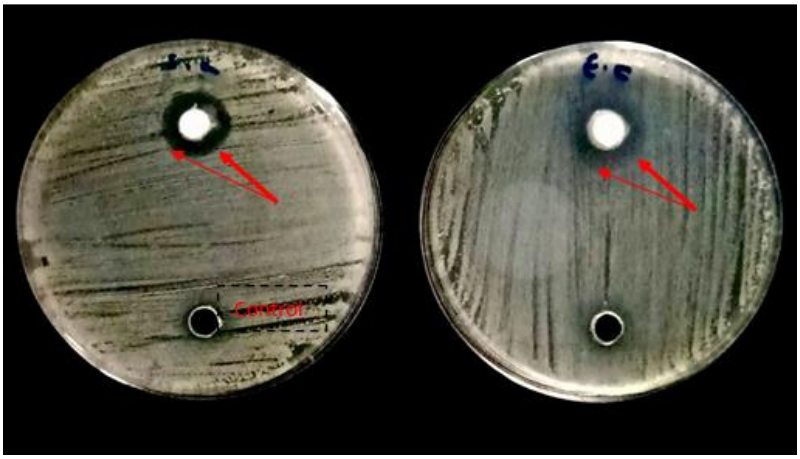

Figure 4.20: Representative photos of *E. coli* colonies and *S. aureus* on Ag-DCP

Samples	Inhibitory diameter of compounds measured in mm against selected microbes	
	S. aureus(+ve)	E. coli
1	16 mm	13

CHAPTER FIVE

CONCLUSIONS AND RECOMMENDATIONS

Conclusions

Findings of The Study

On this work a microwave assisted method is followed for the synthesis of segment pure HA and their doped analogues by using the usage of calcium nitrate tetrahydrate and di-ammonium hydrogen phosphate as Ca^{2+} and PO_4^{3-} precursors respectively. Calcium nitrate and di-ammonium hydrogen phosphate solution react without delay upon blending to furnish amorphous calcium phosphate; but the microwave irradiations extended the fee of reaction by manifold via lowering the activation power of the response. Because of this fast kinetics of the microwave irradiation, it turned into possible to swiftly grant the desired products. The synthesized CaP and their doped analogues were absolutely characterized to decide their phase composition, ionic substitution, impact of doping at the physicochemical houses.

The proportion of powder to liquid (p/l) ratio is a very critical parameter because it determines many homes of the cement along with setting time, bioresorbabity and rheological conduct. On this have a look at we selected 2:1 ratio to reap possible setting time and mechanical properties. The effect of Co^{2+}, Zn^{2+} and Ag^{+} ions doping into the DCP cement on the physicochemical, mechanical residences and antibacterial pastime was studied in element.

Following are the major findings of this study:

1) Co^{2+}, Zn^{2+} and Ag^{+} substituted HA are efficaciously synthesized by microwave assisted wet precipitation technique. Effects showed that Co^{2+}, Zn^{2+} and Ag^{+}

substitution had sizeable effect on the houses of HA., average crystallite sizes of the synthesized Co-HA samples multiplied with increase in co substitution, however the morphology of HA is change from a spherical shape via the doping of Co^{2+} ions, particles seemed tightly agglomerated arranged in clusters.

2) Co^{2+}, Zn^{2+} and Ag^{+} substituted DCPD (brushite) is successfully formed with monocalcium phosphate monohydrate (MCPM), the combination reacted in the presence of trisodium citrate as a liquid phase. Incorporation of co into the brushite lattice decreased the size of unit cellular. The morphology of the crystal is small plate-like with a heterogeneous length distribution. The morphology of the crystal is small plate-like with a heterogeneous size. The morphology of the crystal discovered that the DCPD debris composed of smaller plate-like particles. Consisted of crystals dispersed with exhibiting a more heterogeneous structure.
3) substitution of Co^{2+}, Zn^{2+} and Ag^{+} ions into the brushite cement resulted in huge growth in the setting time. In preferred, the injectability of the cements multiplied with growth inside the dopant attention. The boom in compressive strength of all samples became observed with addition of ions into the cement.
4) incorporation of antimicrobial sellers which includes antibiotics or other antimicrobial dealers in DCP cements can prevent publish-surgical infections. Ag integrated DCP cement established excellent antibacterial against *E-coli* and *Staphylococcus aureus*.
5) The cumulative release of amoxicillin and ampicillin trihydrate from Co- Brc cement systems turned into investigated. In this study the release profile is seen to be bimodal, where burst release is determined in first 12 h followed with the aid of a controlled. The burst launch inside the initial segment followed by using a slow

release over 168 h is taken into consideration beneficial to save you bacterial infection after the surgical operation.

Recommendations and Suggested Future Work

1. Synthesized thru microwave assisted wet precipitation technique. The three ions used in the present study are good potential candidates for various orthopaedic and dental applications. However, using them as biomaterial depends on good in-vivo biocompatibility and low cytotoxicity.
2. In the present study, HA/MCPM have been used to prepare DCP cements, which shows good *in vitro* setting reaction, mechanical properties and antibiotic activity and thus they are considered as potential candidates for various orthopaedic and dental applications. However, more investigation is needed to establish osteoblast cells proliferation and their ability to mineralize the bone matrix and thus establishing suitability of these materials as useable biomaterials for such applications.
3. As it is known that infections are not always produced by the same bacteria. Therefore, it would be very important to propose a material that could be integrated with different drugs, in such a way that the surgeon could choose the drug just before implantation. In addition, a serious drawback for the implementation of this technology is the DCP properties which could be affected by different drugs. Therefore, A lot of work is required to establish the general laws that control the release profile of these types of materials, in order to be able to adjust them to different therapeutically needs and to obtain reproducible and predictable drug delivery systems.

REFERENCES

References

1. Hertel, R., Fractures of the proximal humerus in osteoporotic bone. *Osteoporosis International*, 2005. 16: p. S65-S72.
2. Razfar, N., B. Grawe., Comparison of proximal humeral bone stresses between stemless, short stem, and standard stem length: a finite element analysis. *Journal of shoulder and elbow surgery*, 2016. 25(7): p. 1076-1083.
3. Piccirillo, C., H. Engqvist., Extraction and characterisation of apatite- and tricalcium phosphate-based materials from cod fish bones. *Materials Science and Engineering: C*, 2013. 33(1): p. 103-110.
4. Kumar, A., S. Yilmaz., FEA of humerus bone fracture and healing, *in Advanced Materials for Biomechanical Applications.* 2022, CRC Press. p. 255-272.
5. Nandi, S.K., M. Jagannatham., Orthopaedic applications of bone graft & graft substitutes: a review. *Indian Journal of Medical Reseach*, 2010. 132(1): p. 15-30.
6. Schumaier, A. and B. Grawe, Proximal humerus fractures: evaluation and management in the elderly patient. *Geriatric Orthopaedic Surgery & Rehabilitation*, 2018. 9: p. 2151458517750516.
7. Pu'ad, N.A.S.M., B. Grawe., Syntheses of hydroxyapatite from natural sources. *Heliyon*, 2019. 5(5): p. e01588.

8. Lertcumfu, N., H. Engqvist., Properties of calcium phosphates ceramic composites derived from natural materials. *Ceramics International*, 2016. 42(9): p. 10638-10644.

9. O'Hare, P., S. Yilmaz., biological responses to hydroxyapatite surfaces deposited via a co-incident microblasting technique. *Biomaterials*, 2010. 31(3): p. 515-522.

10. Boskey, A.L., *Third Edit. 2013, Elsevier.*

11. Mour, M., M. Jagannatham., Advances in porous biomaterials for dental and orthopaedic applications. *Materials,* 2010. 3(5): p. 2947-2974.

12. Feng, C., B. Grawe., Co-inspired hydroxyapatite-based scaffolds for vascularized bone regeneration. *Acta Biomaterialia*, 2021. 119: p. 419-431.

13. Zhang, D., H. Engqvist., The development of collagen based composite scaffolds for bone regeneration. *Bioactive materials*, 2018. 3(1): p. 129-138.

14. Falconer, J.L. and D.W. Grainger, 1.4 Silver antimicrobial biomaterials. *Compr*. *Biomater*. II, 2017. 1: p. 79-91.

15. Adzila, S., M. Murad, and I. Sopyan, Doping metal into calcium phosphate phase for better performance of bone implant materials. Recent Patents on *Materials Science*, 2012. 5(1): p. 18-47.

16. Dhandayuthapani, B. and D. Sakthi kumar, Biomaterials for biomedical applications. *Biomedical Applications of Polymeric Materials and Composites*, 2016: p. 1-20.

17. Engstrand, J., C. Persson, and H. Engqvist, The effect of composition on mechanical properties of brushite cements. *Journal of the mechanical behavior of biomedical materials,* 2014. 29: p. 81-90.

18. Dorozhkin, S.V., Calcium orthophosphate cements for biomedical application. *Journal of Materials Science*, 2008. 43(9): p. 3028-3057.

19. Rollo, J.M.D.d.A., B. Grawe., Assessment of trabecular bones microarchitectures and crystal structure of hydroxyapatite in bone osteoporosis with application of the Rietveld method. *Procedia Engineering*, 2015. 110: p. 8-14.

20. Bhat, S.V., Biomaterials. 2005: *Alpha Science Int'l Ltd.*

21. Sofronia, A.M., D.W. Grainger., Thermal and structural characterization of synthetic and natural nanocrystalline hydroxyapatite. *Materials Science and Engineering: C,* 2014. 43: p. 153-163.

22. Hoffman, R.M., Patient-derived orthotopic xenografts: better mimic of metastasis than subcutaneous xenografts. *Nature Reviews Cancer*, 2019. 15(8): p. 451-452.

23. Habraken, W., M. Jagannatham., Calcium phosphates in biomedical applications: materials for the future. *Materials Today*, 2018. 19(2): p. 69-87.

24. Mohd Pu'ad, N.A.S., L.C. Chow., Syntheses of hydroxyapatite from natural sources. *Heliyon*, 2020. 5(5): p. e01588.

25. De Groot, K., Bioceramics Calcium Phosphate. Vol. 226. 2018: *CRC press*.

26. Al-Haddad, A. and Z.A. Che Ab Aziz, Bioceramic-based root canal sealers: a review. *International journal of biomaterials*, 2019. 2016.

27. Moradi, A., M. Pakizeh, and T. Ghassemi, A review on bovine hydroxyapatite; extraction and characterization. *Biomedical Physics & Engineering Express*, 2022. 8(1): p. 012001.

28. Yelten-Yilmaz, A. and S. Yilmaz, Wet chemical precipitation synthesis of hydroxyapatite (HA) powders. *Ceramics International*, 2018. 44(8): p. 9703-9710.

29. Terzioğlu, P., H. Öğüt, and A. Kalemtaş, Natural calcium phosphates from fish bones and their potential biomedical applications. *Materials Science and Engineering: C*, 2018. 91: p. 899-911.

30. Zakaria, S.M., B. Grawe., Nanophase hydroxyapatite as a biomaterial in advanced hard tissue engineering: a review. *Tissue Engineering Part B: Reviews*, 2015. 19(5): p. 431-441.

31. Piccirillo, C., D.W. Grainger., Hydroxyapatite-based materials of marine origin: A bioactivity and sintering study. *Materials Science and Engineering: C*, 2015. 51: p. 309-315.

32. Ni, Z., M. Jagannatham., Synthesis of silver nanoparticle-decorated hydroxyapatite (HA@ Ag) poriferous nanocomposites and the study of their antibacterial activities. *RSC advances*, 2018. 8(73): p. 41722-41730.

33. Bahrololoom, M.E., S. Yilmaz., Characterisation of natural hydroxyapatite extracted from bovine cortical bone ash. *J. Ceram. Process. Res*, 2009. 10(2): p. 129-138.

34. Sallemi, I., F.B. Ayed, and J. Bouaziz. Effect of fluorapatite additive on the mechanical properties of tricalcium phosphate-zirconia composites. *IOP Publishing.*

35. Yokoi, T., H. Engqvist., Hydroxyapatite formation from octacalcium phosphate and its related compounds: a discussion of the transformation mechanism. *Bulletin of the Chemical Society of Japan*, 2020. 93(5): p. 701-707.

36. Lawton, D.M., M.D.J. Lamaletie, and D.L. Gardner, Biocompatibility of hydroxyapatite ceramic: response of chondrocytes in a test system using low temperature scanning electron microscopy. *Journal of Dentistry*, 1989. 17(1): p. 21-27.

37. Pramanik, N., D.W. Grainger., Chemical synthesis, characterization, and biocompatibility study of hydroxyapatite/chitosan phosphate nanocomposite for bone tissue engineering applications. *International journal of biomaterials*, 2009.

38. Do Prado Ribeiro, D.C., M. Jagannatham., Study of the osteoconductive capacity of hydroxyapatite implanted into the femur of ovariectomized rats. *Microscopy research and technique*, 2012. 75(2): p. 133-137.

39. Jaramillo, C.D., H. Engqvist., Osteoconductive and osseointegration properties of a commercial hydroxyapatite compared to a synthetic product. *Revista Colombiana de Ciancia's Peccaries*, 2010. 23(4): p. 471-483.

40. Jang, H.L., L.C. Chow., Phase transformation from hydroxyapatite to the secondary bone mineral, whitlockite. *Journal of materials chemistry* B, 2015. 3(7): p. 1342-1349.

41. Brown, W.E. and L.C. Chow, Chemical properties of bone mineral. Annual *Review of Materials Science*, 1976. 6(1): p. 213-236.

42. Ayatollah, M.R., M. Jagannatham., Mechanical and tribological properties of hydroxyapatite nanoparticles extracted from natural bovine bone and the bone cement developed by nano-sized bovine hydroxyapatite filler. *Ceramics International*, 2015. 41(9, Part A): p. 10818-10827.

43. Venkatesan, J., D.W. Grainger., Isolation and characterization of nano-hydroxyapatite from salmon fish bone. *Materials*, 2015. 8(8): p. 5426-5439.

44. Sun, R.-X., S. Yilmaz., Physicochemical and biological properties of bovine-derived porous hydroxyapatite/collagen composite and its hydroxyapatite powders. *Ceramics International*, 2017. 43(18): p. 16792-16798.

45. Londoño-Restrepo, S.M., L.C. Chow., Study of bovine hydroxyapatite obtained by calcination at low heating rates and cooled in furnace air. *Journal of Materials Science*, 2019. 51(9): p. 4431-4441.

46. Oladele, I.O., K. Pramanik., Non-synthetic sources for the development of hydroxyapatite. *J. Appl. Biotechnol. Bioeng*, 2018. 5(2): p. 88-95.

47. Kabilan, N., H. Engqvist., Optical nonlinear properties of hydroxyapatite-based *materials. Optik*, 2022. 265: p. 169562.

48. Jaber, H.L., A.S. Hammood, and N. Parvin, Synthesis and characterization of hydroxyapatite powder from natural Camelus bone. *Journal of the Australian Ceramic Society*, 2018. 54(1): p. 1-10.

49. Doostmohammadi, A., Dorozhkin, S.V., A comparative physico-chemical study of bioactive glass and bone-derived hydroxyapatite. *Ceramics International*, 2011. 37(5): p. 1601-1607.

50. Fudge, E.A., H. Engqvist., Synthesis of organic derived hydroxyapatite scaffold from pig bone waste for tissue engineering applications. *Advanced Powder Technology,* 2018. 29(1): p. 1-8.

51. López, E.O., D.W. Grainger., Hydroxyapatite and lead-substituted hydroxyapatite near-surface structures: Novel modelling of photoemission lines from X-ray photoelectron spectra. *Applied Surface Science,* 2022. 571: p. 151310.

52. Panda, N.N., K. Pramanik, and L.B. Sukla, Extraction and characterization of biocompatible hydroxyapatite from fresh water fish scales for tissue engineering scaffold. *Bioprocess and Biosystems Engineering,* 2014. 37(3): p. 433-440.

53. DileepKumar, V.G., K. Pramanik., A review on the synthesis and properties of hydroxyapatite for biomedical applications. *Journal of Biomaterials Science, Polymer Edition,* 2022. 33(2): p. 229-261.

54. Sunil, B.R. and M. Jagannatham, Producing hydroxyapatite from fish bones by heat treatment. *Materials Letters,* 2016. 185: p. 411-414.

55. Hidouri, M., S.V. Dorozhkin, and N. Albeladi, Thermal behavior, sintering and mechanical characterization of multiple ion-substituted hydroxyapatite bioceramics. *Journal of Inorganic and Organometallic Polymers and Materials*, 2019. 29: p. 87-100.

56. Neelakandeswari, N., G. Sangami, and N. Dharmaraj, Preparation and characterization of nanostructured hydroxyapatite using a biomaterial. Synthesis and Reactivity in Inorganic, *Metal-Organic, and Nano-Metal Chemistry*, 2011. 41(5): p. 513-516.

57. Bano, N., L.C. Chow., Natural hydroxyapatite extracted from bovine bone. *Journal of Science and Technology,* 2017. 9(2).

58. Hussin, M.S.F., M. Jagannatham., Extraction of natural hydroxyapatite for biomedical applications—A review. Heliyon, 2022: p. e10356.

59. Akram, M., Dorozhkin, S.V., Extracting hydroxyapatite and its precursors from natural resources. *Journal of Materials Science*, 2014. 49(4): p. 1461-1475.

60. Sihn, Y., D.W. Grainger., Cation-exchanged hydroxyapatite for strontium separation from groundwater. 2021.

61. Herliansyah, M.K., K. Pramanik., Preparation and characterization of natural hydroxyapatite: a comparative study of bovine bone hydroxyapatite and hydroxyapatite from calcite. *Trans Tech Publ.*

62. Ayatollahi, M.R., Dorozhkin, S.V., Mechanical and tribological properties of hydroxyapatite nanoparticles extracted from natural bovine bone and the

bone cement developed by nano-sized bovine hydroxyapatite filler. *Ceramics International*, 2015. 41(9): p. 10818-10827.

63. Ruksudjarit, A., L.C. Chow., Synthesis and characterization of nanocrystalline hydroxyapatite from natural bovine bone. *Current applied physics*, 2008. 8(3-4): p. 270-272.

64. Khurshid, Z., M. Jagannatham., Extraction of Hydroxyapatite from Camel Bone for Bone Tissue Engineering Application. *Molecules*, 2022. 27(22): p. 7946.

65. Le Ho, K.H., Lawton., Physicochemical properties, acute and subchronic toxicity of nano-hydroxyapatite obtained from Lates calcarifer fish bone. *Regional Studies in Marine Science*, 2022. 55: p. 102560.

66. Indra, A., K. Pramanik., Behavior of sintered body properties of hydroxyapatite ceramics: effect of uniaxial pressure on green body fabrication. *Materials Today Sustainability*, 2023. 17: p. 100100.

67. Indra, A., A. Kalemtaş., A novel fabrication procedure for producing high strength hydroxyapatite ceramic scaffolds with high porosity. *Ceramics International*, 2021. 47(19): p. 26991-27001.

68. Odusote, J.K., Lawton., Synthesis and characterization of hydroxyapatite from bovine bone for production of dental implants. *Journal of applied biomaterials & functional materials*, 2019. 17(2): p. 2280800019836829.

69. Taufik S, A., Dorozhkin, S.V., Treatment of bone defects with bovine hydroxyapatite xenograft and platelet rich fibrin (PRF) to accelerate bone

healing. *International Journal of Surgery Case Reports*, 2022. 97: p. 107370.

70. Azzallou, R., D.W. Grainger., Bovine bone-derived natural hydroxyapatite-supported $ZnCl_2$ as a sustainable high efficiency heterogeneous biocatalyst for synthesizing amidoalkyl naphthols. *Journal of Physics and Chemistry of Solids,* 2022. 163: p. 110533.

71. Han, K.-S., De Groot, K., Wound healing efficacy of biocompatible hydroxyapatite from bovine bone waste for bone tissue engineering application. *Journal of Environmental Chemical Engineering,* 2022. 10(1): p. 106888.

72. Pazourková, L., G.S. Martynková, and M. Šupová, Ca-deficient hydroxyapatite synthesis on the bioapatite bovine bone substrate study. *Materials Today: Proceedings*, 2021. 52: p. 227-231.

73. Londoño-Restrepo, S.M., A. Kalemtaş., The effect of cyclic heat treatment on the physicochemical properties of bio hydroxyapatite from bovine bone. *Journal of Materials Science: Materials in Medicine*, 2018. 29: p. 1-15.

74. Pires, L.A., Lawton., Effects of ZnO/TiO2 nanoparticle and TiO2 nanotube additions to dense polycrystalline hydroxyapatite bioceramic from bovine bones. *Dental Materials,* 2020. 36(2): p. e38-e46.

75. Surya, P., De Groot, K., Synthesis and characterization of nano-hydroxyapatite from Sardinella longiceps fish bone and its effects on human osteoblast bone cells. *Journal of the Mechanical Behavior of Biomedical Materials,* 2021. 119: p. 104501.

76. Hasan, M.R., N.S.M. Yasin, and M.S. Mohd, Proximate and morphological characteristics of nano hydroxyapatite (Nano HAp) extracted from fishbone. *Journal of Sustainability Science and Management*, 2020. 15(8): p. 9-21.

77. Venkatesan, J., D.W. Grainger., Isolation and Characterization of Nano-Hydroxyapatite from Salmon Fish Bone. *Materials (Basel),* 2015. 8(8): p. 5426-5439.

78. Pal, A., I. Sopyan., Synthesis of hydroxyapatite from Lates calcarifer fish bone for biomedical applications. *Materials Letters,* 2017. 203: p. 89-92.

79. Shi, P., N. Albeladi., Characterization of natural hydroxyapatite originated from fish bone and its biocompatibility with osteoblasts. *Materials Science and Engineering: C,* 2018. 90: p. 706-712.

80. Ahmad Fara, A.N.K., M.A. bin Yahya, and H.Z. Abdullah. Preparation and characterization of biological hydroxyapatite (HAp) obtained from Tilapia fish bone. *Trans Tech Publ*.

81. Popescu-Pelin, G., Lawton., Fish bone derived bi-phasic calcium phosphate coatings fabricated by pulsed laser deposition for biomedical applications. *Marine drugs*, 2020. 18(12): p. 623.

82. Elango, J., A. Kalemtaş., Rheological, biocompatibility and osteogenesis assessment of fish collagen scaffold for bone tissue engineering. *International Journal of Biological Macromolecules*, 2016. 91: p. 51-59.

83. Pon-On, W., L.B. Sukla., Hydroxyapatite from fish scale for potential use as bone scaffold or regenerative material. *Materials Science and Engineering: C,* 2016. 62: p. 183-189.

84. Manalu, J., B. Soegijono, and D. Indrani, Characterization of Hydroxyapatite Derived from Bovine Bone. 2015.

85. Sathiyavimal, S., I. Sopyan., Natural organic and inorganic–hydroxyapatite biopolymer composite for biomedical applications. *Progress in Organic Coatings*, 2020. 147: p. 105858.

86. Ribeiro, N., L.B. Sukla., New prospects in skin regeneration and repair using nanophased hydroxyapatite embedded in collagen nanofibers. *Nanomedicine: Nanotechnology, Biology and Medicine*, 2021. 33: p. 102353.

87. Bano, N., L.C. Chow., Extraction of biological apatite from cow bone at different calcination temperatures: a comparative study. *Key Engineering Materials*, 2019. 796: p. 46-52.

88. Mondal, S., De Groot, K., Studies on Processing and Characterization of Hydroxyapatite Biomaterials from Different Bio Wastes. *Journal of Minerals and Materials Characterization and Engineering*, 2012. 11: p. 55-67.

89. Zhang, L., I. Sopyan., Extraction and characterization of HA/β-TCP biphasic calcium phosphate from marine fish. *Materials Letters*, 2019. 236: p. 680-682.

90. Balamurugan, A., L.B. Sukla., Suitability evaluation of sol–gel derived Si-substituted hydroxyapatite for dental and maxillofacial applications through in vitro osteoblasts response. *Dental Materials*, 2008. 24(10): p. 1374-1380.

91. Walsh, P.J., L.B. Sukla., Low-pressure synthesis and characterisation of hydroxyapatite derived from mineralise red algae. *Chemical Engineering Journal,* 2008. 137(1): p. 173-179.

92. Monballiu, A., De Groot, K., Phosphate recovery as hydroxyapatite from nitrified UASB effluent at neutral pH in a CSTR. *Journal of Environmental Chemical Engineering,* 2018. 6(4): p. 4413-4422.

93. Govindaraj, D. and M. Rajan, Synthesis and Spectral Characterization of Novel Nano-Hydroxyapatite from Moringaoleifera Leaves. *Materials Today: Proceedings*, 2016. 3(6): p. 2394-2398.

94. Salma-Ancane, K., L. Stipniece, and Z. Irbe, Effect of biogenic and synthetic starting materials on the structure of hydroxyapatite bioceramics. *Ceramics International,* 2016. 42(8): p. 9504-9510.

95. Tarafdar, A., Bouaziz., Advances in biomaterial production from animal derived waste. *Bioengineered*, 2021. 12(1): p. 8247-8258.

96. Deng, K., N. Albeladi., Preparation and characterization of porous HA/β-TCP biphasic calcium phosphate derived from butterfish bone. *Materials Technology,* 2022. 37(10): p. 1388-1395.

97. Huang, Y.-C., P.-C. Hsiao, and H.-J. Chai, Hydroxyapatite extracted from fish scale: Effects on MG63 osteoblast-like cells. *Ceramics International*, 2011. 37(6): p. 1825-1831.

98. Shaltout, A.A., M.A. Allam, and M.A. Moharram, FTIR spectroscopic, thermal and XRD characterization of hydroxyapatite from new natural

sources. Spectrochimica Acta Part A: *Molecular and Biomolecular Spectroscopy*, 2011. 83(1): p. 56-60.

99. Rabiei, M., I. Sopyan., Comparing methods for calculating nano crystal size of natural hydroxyapatite using X-ray diffraction. *Nanomaterials*, 2020. 10(9): p. 1627.

100. Plumbum, I., Synthesis and characterization of hydroxyapatite from bulk seashells and its potential usage as lead ions adsorbent. *Malaysian Journal of Analytical Sciences*, 2017. 21(3): p. 571-584.

101. Vallet-Regí, M. and J.M. González-Calbet, Calcium phosphates as substitution of bone tissues. *Progress in Solid State Chemistry*, 2004. 32(1): p. 1-31.

102. Klinkaewnarong, J. and S. Utara, Ultrasonic-assisted conversion of limestone into needle-like hydroxyapatite nanoparticles. *Ultrasonics Sonochemistry*, 2018. 46: p. 18-25.

103. Wu, S.-C., I. Sopyan ,.A hydrothermal synthesis of eggshell and fruit waste extract to produce nanosized hydroxyapatite. *Ceramics International*, 2013. 39(7): p. 8183-8188.

104. Ofudje, E.A., D. Sakthi kumar., Nano-rod hydroxyapatite for the uptake of nickel ions: Effect of sintering behavior on adsorption parameters. *Journal of Environmental Chemical Engineering*, 2021. 9(5): p. 105931.

105. Sharma, C., De Groot, K., Fabrication and characterization of novel nano-biocomposite scaffold of chitosan–gelatin–alginate–hydroxyapatite for bone

tissue engineering. *Materials Science and Engineering: C*, 2016. 64: p. 416-427.

106. Bayar, N., M. Kriaa, and R. Kammoun, Extraction and characterization of three polysaccharides extracted from Opuntia ficus indica cladodes. *International Journal of Biological Macromolecules*, 2016. 92: p. 441-450.

107. Aarthy, S., Kabilan, N. Exploring the effect of sintering temperature on naturally derived hydroxyapatite for bio-medical applications. *Journal of Materials Science: Materials in Medicine*, 2019. 30: p. 1-11.

108. Jindapon, N., D. Sakthi kumar., Preparation, Characterization, and Biological Properties of Hydroxyapatite from Bigeye Snapper (Priancanthus tayenus) Bone. *International Journal of Molecular Sciences*, 2023. 24(3): p. 2776.

109. Grassino, A.N., Bouaziz., Ultrasound assisted extraction and characterization of pectin from tomato waste. *Food chemistry*, 2016. 198: p. 93-100.

110. Alici, E.H., Lawton., Alkyl chain modified metal phthalocyanines with enhanced antioxidant-antimicrobial properties by doping Ag^+ and Pd^{2+} ions. *Journal of Molecular Structure*, 2022. 1257: p. 132634.

111. Akindoyo, J.O., Kabilan, N., Synthesis of hydroxyapatite through ultrasound and calcination techniques. *IOP Publishing.*

112. Suchanek, W. L., Byrappa, K., Shuk, P., Riman, R. E., Janas, V. F. and Tenhuisen, K. S. Preparation of Magnesium-Substituted Hydroxyapatite Powders

by The Mechanochemical–Hydrothermal Method. Biomaterials. 2004. 25(19): 4647-4657.

113. Yang, C., Yang, P., Wang, W., Wang, J., Zhang, M. and Lin, J. Solvothermal Synthesis and Characterization of Ln (Eu^{3+}, Tb^{3+}) Doped Hydroxyapatite. *Journal of Colloid and Interface Science*. 2008. 328(1): 203-210.

114. Zhang, C., Xiao, L., Liu, C., Duan, C., Yang, J. and Wang, F. Ultrasonic Chemistry Fabrication of Carbonated Silicon-Substituted Hydroxyapatite Nanopowder and Its Configuration Representation. *Journal of The Chinese Ceramic Society*. 2011. 39(12): 1915-1921.

115. Zhu, K., Qiu, J., Ji, H., Yanagisawa, K., Shimanouchi, R., Onda, A. and Kajiyoshi, K. Crystallographic Study of Lead-Substituted Hydroxyapatite Synthesized By High-Temperature Mixing Method Under Hydrothermal Conditions. *Inorganica Chimica Acta*. 2010. 363(8): 1785-1790.

116. Ma, X. and Ellis, D. E. Initial Stages of Hydration and Zn Substitution/Occupation On Hydroxyapatite (0001) Surfaces. *Biomaterials*. 2008. 29(3): 257-265.

117. Boanini, E., Gazzano, M. and Bigi, A. Ionic Substitutions In Calcium Phosphates Synthesized At Low Temperature. *Acta Biomaterialia*. 2010. 6(6): 1882-1894.

118. Mcconnell, D. *Apatite*. Applied Mineralogy Technische Mineralogie, Wien: Springer-Verlag. 1973.

119. Shibata, S., Doi, Y., Takezawa, Y., Wakamatsu, N., Horiguchi, T., Kamemizu, H., Moriwaki, Y., Kubo, F. and Haeuchi, Y. Self-Setting Apatite

Cement. VII. Barium-Apatite As Radio-Opaque Medium. *Journal of The Japanese Society For Dental Materials and Devices*. 1989. 8(1): 77-82.

120. Kizuki, T., Ohgaki, M., Hashimoto, K., Toda, Y., Udagawa, S. and Yamashita, K. Synthesis of Apatite-Type Barium Rare Earth Oxide Silicates and Estimation of Their Biocompatibility. *Journal of The Ceramic Society of Japan*. 2001. 109(1266): 162-167.

121. Baxter, F., Turner, I., Bowen, C., Gittings, J. and Chaudhuri, J. An In Vitro Study of Electrically Active Hydroxyapatite-Barium Titanate Ceramics Using Saos-2 Cells. *Journal of Materials Science: Materials In Medicine*. 2009. 20(8): 1697-1708.

122. Baxter, F. R., Turner, I. G., Bowen, C. R., Gittings, J. P., Chaudhuri, J. B. and Lewis, R. W. C. The Structure and Properties of Electroceramics For Bone Graft Substitution. 2008. 99-102.

123. Baxter, F. R., Bowen, C. R., Turner, I. G. and Dent, A. C. E. Electrically Active Bioceramics: A Review of Interfacial Responses. *Annals of Biomedical Engineering*. 2010. 38(6): 2079-2092.

124. Furuya, K., Morita, Y., Tanaka, K., Katayama, T. and Nakamachi, E. Acceleration of Osteogenesis by Using Barium Titanate Piezoelectric Ceramic As An Implant Material. 2011. 10.1117/12.881858: 79750U-79750U.

125. Jianqing, F., Huipin, Y. and Xingdong, Z. Promotion of Osteogenesis by A Piezoelectric Biological Ceramic. *Biomaterials*. 1997. 18(23): 1531-1534.

126. Shackleton, K. L., Stewart, E. T., Henderson Jr, J. D., Demeure, M. J. and Telford, G. L. Effect of Barium Sulfate on Wound Healing In The Gastrointestinal Tract of The Rat. *Radiology*. 2000. 214(2): 563-567.

127. Leng, H., Wang, X., Ross, R. D., Niebur, G. L. and Roeder, R. K. Micro-Computed Tomography of Fatigue Microdamage In Cortical Bone Using A Barium Sulfate Contrast Agent. *Journal of The Mechanical Behavior of Biomedical Materials*. 2008. 1(1): 68-75.

128. Basten, C. H. J. and Kois, J. C. The Use of Barium Sulfate For Implant Templates. *Journal of Prosthetic Dentistry*. 1996. 76(4): 451-454.

129. Fowler, B. O. Infrared Studies of Apatites. II. Preparation of Normal and Isotopically Substituted Calcium, Strontium, and Barium Hydroxyapatites and Spectra-Structure-Composition Correlations. *Inorganic Chemistry*. 1974. 13(1): 207-214.

130. Bigi, A., Foresti, E., Marchetti, F., Ripamonti, A. and Roveri, N. Barium Calcium Hydroxyapatite Solid Solutions. *Journal of The Chemical Society, Dalton Transactions*. 1984. 10.1039/DT9840001091(6): 1091-1093.

الخلاصة

تعتبر المواد الحيوية والتي تشمل أسمنت فوسفات الكالسيوم من المواد الواعدة مستقبلا في علاج كسور العظام وذلك لما لها من صفات توافق حيوي مع العظام الطبيعية من حيث الخواص الفسيولوجية مثل التوافق الحيوي والخواص الميكانيكية. وبما انها ذات تصلب ضعيف قد تكون قابلية حقن الأسمنت ضرورية للغاية للأساليب الجراحية التي تتطلب حقن الأسمنت في عيوب العظام، وقد يحصل فصل بين الطورين الصلب والسائل فان ذلك يؤدي الحد من استخدامها في الجراحة العظمية. قد تكون قابلية حقن الأسمنت ضرورية للغاية للأساليب الجراحية التي تتطلب حقن الأسمنت في عيوب العظام. ولكن العامل الأهم لنجاح التدخلات الجراحية لزراعة الأطراف الاصطناعية أو المواد الموصلة للعظام هو الوقاية من العدوى البكتيرية بعد الجراحة. يمكن أن يمنع ذلك هو استخدام مضادات الميكروبات، بما في ذلك المضادات الحيوية أو غيرها من مضادات الميكروبات في هذه الدراسة تم تحضير مجموعة من أسمنت DCP الجديد من خلال مشوبة أيونات Co^{2+}و Zn^{2+} Ag^{+}في هيدروكسي أباتيت(HA) ثم تفاعلها مع أحادي فوسفات الكالسيوم أحادي الهيدرات (MCPM)في وجود سترات الصوديوم الثلاثي. دُرست آثار التشوب الأيوني على زمن الصب، وقابلية الحقن، وقوة الضغط، والتأثير المضاد للميكروبات لأسمنت ثنائي فوسفات الكالسيوم. استُخدمت تقنيات حيود الأشعة السينية (XRD)، ومجهر مسح الإلكترون بالانبعاث (FESEM) مع تحليل الأشعة السينية المشتتة للقوة (EDX)، ومطياف الأشعة تحت الحمراء (FTIR تركيب استُخدم جهاز إبرة جيلمور لتحديد زمن التصلب الأولي والأخير للأسمنت (ASTM c266-89). استُخدمت سلسلة Instron ix (ASTM-model 8.33 لتحديد قوة الضغط. تم تقييم سلوك ذوبان جميع أنواع الأسمنت في المختبر عن طريق غمر العينات في محلول الخلية العظمية الافتراضية (SBF) لمدة سبعة أيام عند درجة حرارة ٣٧ درجة مئوية. أدى استبدال الكوبالت والزنك والفضة في أسمنت البروشيت إلى زيادة قوة الضغط. واشارت إطلاق المضادات الحيوية إلى أن الأسمنت المُشَبَّب كأنظمة إطلاق مُتحكَّم فيها للأدوية. استبدال الكوبالت والزنك والفضة في أسمنت البروشيت إلى زيادة قوة الضغط. تشير النتائج الى إطلاق المضادات الحيوية إلى أن الأسمنت المُشَبَّب يمكن استخدامه أيضًا كأنظمة إطلاق مُتحكَّم فيها للأدوية. تم اختبار اسمنت المشوب بالفضة كمضاد بكتيري بأستخدام نوعين من البكتيريا وكانت نتائج جيدة في قتل الكتيريا.

.

جمهورية العراق

وزارة التعليم العالي والبحث العلمي
جامعة ميسان
كلية العلوم
قسم الكيمياء

تحضير وتشخيص لحقن أيونات الكوبلت والزنك والفضة المشوبة مع أسمنت ثنائي فوسفات الكالسيوم للاستخدامات المحتملة في جراحة العظام

رسالة مقدمة الى

كلية العلوم / جامعة ميسان جزء من متطلبات نيل شهادة الماجستير في علوم الكيمياء

من قبل الطالبة

مروه محمد عبد الله

بكالوريوس علوم كيمياء / جامعة البصرة (٢٠١٢)

باشراف

الأستاذ المساعد الدكتور علي طه صالح

٢٠٢٥